Flux flow and proximity effects in aligned Pb-Cd eutectic lamellar structures

by

Cary Ray Spencer

A Dissertation Submitted to the
Graduate Faculty in Partial Fulfillment of
The Requirements for the Degree of
DOCTOR OF PHILOSOPHY

Department: Physics
Major: Solid State Physics

Approved:

Signature was redacted for privacy.

In Charge of Major Work

Signature was redacted for privacy.

For the Major Department

Signature was redacted for privacy.

For the Graduate College

Iowa State University
Ames, Iowa

1977

TABLE OF CONTENTS

LIST OF FIGURES

LIST OF TABLES

LIST OF SYMBOLS

L	-Voltage lead spacing of sample
W	-Width of sample
Z	-Thickness of sample
d	-Lamellar periodicity
d_S	-Thickness of superconducting lamellae
d_N	-Thickness of normal lamellae
b	-Extrapolation length
$\lambda_{N,S}$	-Penetration depth in lamellae
$\xi_{N,S}$	-Coherence length in lamellae
$l_{N,S}$	-Electron mean free path
m_α	-Slope of α liquidus near eutectic point
m_β	-Slope of β liquidus near eutectic point
R	-Rate of directional solidification
D_x	-Diffusion coefficient of x
T	-Temperature
T_c	-Transition temperature
H_c	-Thermodynamic critical field
H_{c1}	-Lower critical field
H_{c2}	-Upper critical field
$\Delta(T)$	-Superconducting pair potential
$E_g(T)$	-Energy gap

f_L -Lorentz force

f_p -Flux pinning force

ρ_f -Flux flow resistivity

v_L -Vortex line velocity

η -Flux flow viscosity coefficient

J_T -Transport current density

J_c -Critical current density

INTRODUCTION

Superconductivity

Superconductivity has been a field of active research since Onnes (1) first observed the resistanceless state in 1911. Indeed, over the past 20 years, such properties as the specific heat, thermal conductivity, and the microwave absorption have been investigated thoroughly by well-defined experiments and a consistent theory for a variety of different behaviors has been developed. To considerable extent, the research has concentrated on homogeneous or spatially uniform systems in which boundaries are not of crucial importance, and with few exceptions, theory and experiment are in rather good agreement. In the work reported here, however, we will be extending the area of interest to include inhomogeneous superconductors in which boundary effects play a central role. In this regime the behavior of superconductors is not so well understood, partly because it is experimentally difficult to prepare well-defined boundaries and partly because the theory has additional variables. There is an extensive literature about boundary effect problems, but our understanding of composite systems lags far behind our understanding of homogeneous systems.

Recently, new techniques for preparing composite materials have opened a whole new realm of experiments for

inhomogeneous systems. With these advances, there is now the possibility of doing experiments with a large number (>1000) of relatively clean boundaries. Over the past few years, in collaboration with J. D. Verhoeven, we have developed techniques for the growth of oriented lamellar composites by directionally solidifying the eutectic composition of a binary system such as Pb-Cd. It is now a rather routine matter to prepare a lamellar structure with approximately 1000 aligned superconducting-normal boundaries. In such a material the superconducting pair potential will be periodically modulated with the lamellar period of the structure. Our primary goal in this research is to study the superconducting properties of these lamellar composites with the idea of developing new classes of materials which will utilize the periodic modulation of the long range coherent effects of superconductors. Taking the long view, we particularly want to study flux pinning and coherent radiation from arrays of superconductor-normal-superconductor (SNS) junctions if suitable new materials can be developed.

A number of experimental tools have been used to study superconductivity. Single particle tunneling (2) has proved to be a powerful tool to study the excitation spectrum of superconductors. Toplicar (3) has recently used this tool to study evaporated thin film single

composites of Pb and Cd. By varying the Pb thickness from 950A to 330A, Toplicar measured a change of the superconducting transition temperature from 7.22K to 4.8K. The observed energy gaps in these sandwiches varied from 1.38meV to 0.43meV. Toplicar calculated a phonon spectral function, the shape of which remained essentially unchanged throughout the series of samples studied.

At present, Zaitlin (4) is using thermal conductivity to determine the superconducting behavior of our Pb-Cd lamellar composites. As a function of magnetic field, the thermal conductivity shows a sharp decrease at a field H_d, where H_d is smaller than the critical field of Pb. This decrease in thermal conductivity is very dependent on the lamellar spacing and on temperature and corresponds to the Cd lamellae being induced into a superconducting state by the adjacent Pb lamellae.

In this work we present complementary information in which we have primarily used electrical resistance as a probe to study flux pinning, the proximity effect, and the Josephson effect (5) for the lamellar composite materials with multiple SNS junctions. In order to understand the behavior of composite systems, it is helpful to now recall some of the basic ideas which have been developed for homogeneous superconducting systems.

Superconductivity is a phenomenon which occurs in many metals and alloys when cooled below a transition temperature, T_c, which is characteristic of that material. One of the most striking properties of the superconducting state is the complete loss of resistance of the metal when cooled below T_c when no magnetic field is present. Persistent currents have been observed to flow in superconducting rings with reported decay times of over 100,000 years (6), emphasizing that the dc electrical resistivity is exactly or immeasurably close to zero (resistivity less than 10^{-22} ohm-cm). This resistanceless state may be destroyed at temperatures less than T_c in the presence of some minimum magnetic field H_c, called the thermodynamic critical field. The critical field may be related to T_c by the empirical relation

$$H_c(T) = H_c(0)[1 - (T/T_c)^2] \quad . \tag{1}$$

Meissner and Ochsenfeld (7) reported that superconductors are perfect diamagnets in low fields. Although zero resistivity is a very important feature of superconductivity, this perfect conduction is not sufficient to predict the perfect diamagnetism exhibited by superconductors. The diamagnetism in a superconductor in an applied magnetic field is the result of circulating surface currents which flow to cancel the magnetic flux density inside the superconductor. Most superconducting

elements display type I superconductivity in which the shielding currents increase as the magnetic field increases. When the magnetic field reaches a critical value, the material reverts abruptly to its normal state. Type II superconductivity is the more common class of superconductors which consists of most superconducting alloys and compounds and some elements which go into a mixed state when the applied magnetic field exceeds the lower critical field H_{c1} characteristic of the material. The mixed state consists of a superconducting matrix with quantized magnetic flux vortices penetrating through the material. As the magnetic field is increased above H_{c1}, the normal regions of the specimen, called fluxoids, become more closely packed and finally combine; the material becomes normal when the upper critical magnetic field H_{c2} is reached. It should be noted that no fundamental changes in the crystal lattice take place when the superconducting transition takes place in zero field. However, very small magnetostrictions at temperatures less than T_c have been reported (8) when the sample was driven normal by a magnetic field. Definite changes take place in the thermal conductivity and specific heat in the superconducting state. There is no latent heat associated with the transition at T_c, however, if the superconducting transition occurs at $T<T_c$ in a magnetic field, there is a

latent heat absorbed by the sample as it goes normal.

Although various attempts to explain the superconducting phenomena were previously advanced, it was not adequately theoretically described until 1957 when Bardeen, Cooper, and Schrieffer (BCS) advanced their famous theory of superconductivity (9). The BCS model predicts that the superconducting ground state of a solid can be described by a single wave function which is a coherent mixture of normal state Bloch wave functions. These superconducting states are occupied in pairs instead of individual electrons as in the normal state. Bloch states are mixed because of the exchange of virtual phonons between electrons close to the Fermi surface and BCS were able to show that the lowest energy state occurs when these electrons are exactly paired with electrons having opposite wave vector and opposite spin.

Cooper pairing is limited to electrons close (10^{-4}eV) to the Fermi surface. The electrons in the metal are often described by the two fluid model (10) in which the total electron density is divided into superfluid electrons and normal electrons. The pairing of the superconducting electrons leads to a lower energy for the system. The net effect of the electron-electron interaction is a lowering of the energy of the entire system. The minimum energy required to break a Cooper pair and to create an excitation

is

$$E_g = 2\Delta(T) \quad . \tag{2}$$

E_g is experimentally observed as an energy gap in the superconducting excitation spectrum and $\Delta(T)$ is directly related to the strength of the electron-phonon interaction. Electrons participating in the superconducting phase cannot be randomly scattered, since this would create empty pair states and lead to a rise in the energy of the system. This explains why superconducting electrons experience no dc electrical resistivity and contribute nothing to the thermal conductivity of the superconductor.

A great deal of interest has been generated in high critical current density, J_c, materials which can be applied to commercial applications because of their lossless electrical transport properties. Using BCS theory, it can be shown (11) that the pair breaking critical current density is given by $J_c = en_s\Delta/p_F$, where n_s is the superconducting electron density. The critical current density is the current density above which electron scattering may take place with a change in total momentum of the system. A change in total momentum of the electron system is manifest experimentally as a sample resistivity. However, other mechanisms, such as flux pinning, determine the critical current density in most systems. The mechanisms which cause high J_c have been under study in an

attempt to better understand both qualitatively and quantitatively the physics of these so-called pinning effects and how to fabricate materials with better J_c characteristics than now available. Also, it has been known for some time that a composite structure of superimposed normal and superconducting thin films may exhibit properties far different from those of the original, separated thin films. This is the proximity effect. The proximity effect may cause the transition temperature of the superconductor to be depressed. The normal metal may be induced to the superconducting state and the density of states may be significantly changed in both metals. Theoretical interest (12,13,14) has been generated in these subjects, but adequate solutions for the superconducting-normal boundary problem do not yet exist. This problem of how the Cooper pairs behave at a superconducting-normal boundary has been of great theoretical and experimental interest, but remains one of the least understood problems in the theory of superconductivity.

Toplicar (3) studied the proximity effect in superimposed Pb and Cd films by a tunneling method. In the thin film regime, the measured transition temperature was shown to vary as a function of the thickness of the superconducting Pb film as predicted by the de

Gennes-Werthamer theory (12,13). Toplicar's tunneling density of states results qualitatively resembled the results predicted by McMillan (15) and the observed phonon structure in the density of states was seen to occur at the same energy as in bulk Pb. An attempt to further understand the proximity effect in Pb and Cd is undertaken in this work by studying with a standard resistive method highly aligned lamellar Pb-Cd structures grown by a directional solidification technique. Because of the highly anisotropic nature of the Pb-Cd lamellar structure, the pinning effects due to inhomogeneities in the samples are also studied. Since the thickness of the Pb lamellae is much larger than the electron mean free path in the Pb metal, these structures allow the opportunity to study the proximity effects and pinning in structures which are out of the thin film regime of Toplicar and other experimenters. The method by which the Pb-Cd lamellar structures are grown guarantees that the Pb and Cd layers are in very good electrical and mechanical contact. To better understand how resistivity studies can be used to study superconductivity in Pb-Cd lamellar structures, it is useful to review the theoretical models for pinning, flux flow, and the proximity effect and how these models may be applied to the very anisotropic Pb-Cd samples used in this work.

Flux Pinning and Flux Flow

As early as 1930, experimenters (16) had hopes of making superconducting magnets of the Pb-Bi alloy which was known to have a critical field of 20 KOe. Unfortunately, measurements by Keesom (17) later showed that the critical current density of this alloy was too low to be practical. It wasn't until 1961 that J_c in Nb_3Sn was found to be 10^5 A/cm^2 in magnetic fields approaching 100 KOe and great interest was stimulated in the properties of superconductors which allow them to carry large current densities. Berlincourt and Hake (18,19) emphasized that high field superconductivity involves two distinct aspects: the existence of a high critical field follows solely from the bulk electronic properties (type II superconductivity) and the current-carrying capacity is strongly dependent on the presence of inhomogeneities and lattice defects (hard superconductivity).

Kim et al. (20,21) deduced that the critical current density in hard superconductors is limited by the pinning force on a fluxoid. These results led Anderson (22) to develop his flux creep theory which assumes that flux vortices are moving quantities that move in such a direction to equalize the macroscopic magnetic pressure in the presence of the Lorentz force. Vortices may be trapped or "pinned" wherever there exists a lattice defect or

inhomogeneity. This pinning effect is not well-understood, but the interaction between the vortex and the defect is thought to modify the vortex structure, which creates an energy barrier the vortex must overcome before it can move. A thorough analysis of various pinning mechanisms is given elsewhere by Campbell and Evetts (23) and is beyond the scope of this work. The penetration depth decreases as the temperature decreases, so the energy per unit length of flux increases with decreasing temperature. The critical current is, therefore, expected to be a temperature-dependent quantity. Analysis of pinning is extremely difficult because of the various complexities, the variety, and the spatial distribution of the pinning sites and mechanisms available.

Kim et al. (24,25,26) first presented an approach to explain the flux flow and power dissipation in samples displaying type II superconductivity. The typical sample geometry for flux flow experiments is a flat sheet of type II superconductor with the magnetic field applied perpendicular to the flat surface and a transport current flowing parallel to the flat surface in the sample (figure 1). A macroscopic treatment assumes that J_T is uniformly distributed within the sample. If the macroscopic magnetic pressure gradients are distributed equally among the vortices, the Lorentz force per unit length of flux is

$$f_L = J_T \phi_o / c \quad . \tag{3}$$

This relation was also demonstrated by Josephson (27) using thermodynamic arguments calculating the change in free energy for a vortex when the vortex is subjected to a virtual displacement of the field. The fluxoid remains pinned until the Lorentz force, f_L, exceeds the pinning force. As f_L increases more, the flux line motion enters a viscous flow state described by the equation

$$\eta v_L = J_T \phi_o / c - f_p = f_L - f_p \quad , \tag{4}$$

where v_L is the vortex line velocity orthogonal to J_T and H and $\eta(T,H)$ is an effective viscosity coefficient of the material. Faraday's law predicts that an average macroscopic electric field will arise in the sample as a result of these moving vortices, given by

$$E_o = n(v_L/c)\phi_o = (v_L/c)B \quad , \tag{5}$$

where n is the flux line density. One can eliminate f_p by taking derivitives of equations 4 and 5:

$$\frac{dv_L}{df_L} = \frac{c}{\phi_o}\frac{dv_L}{dJ_T} = \frac{1}{\eta} \quad ; \quad \frac{dE_o}{dv_L} = \frac{B}{c} \quad ,$$

Combining these expressions yields the flux flow resistivity

$$\rho_f = \frac{dE_o}{dJ_T} = \frac{\phi_o}{\eta c^2} B \quad . \tag{6}$$

Figure 1 shows how ρ_f is determined experimentally. For a fixed magnetic field, the sample voltage is measured as a function of increasing current. There is some speculation about what voltage actually is detected by a voltmeter connected to the sample with leads making contact at the sample surface. Khanna, Clem, and Le Blanc (28) point out that questions remain as to what extent the voltage depends on measuring-circuit lead configurations and whether vortex-line segments moving deep within the sample contribute to the measured voltage. The critical current, I_c, is the current at which a detectable voltage first appears. The voltage then rises and becomes a linear function of I. The slope of this linear, or flux flow, region is also linearly dependent on H as would be expected from equation 6. Once ρ_f is determined, η can be determined from equation 6. Bardeen and Stephen (29) solved the equation of motion of an isolated flux line to derive the same value of ρ_f as above. This analysis yields η as a function of normal state variables:

$$\eta = \phi_o H_{c2}/(\rho_N c^2) \quad \text{for} \quad H < H_{c2} \quad . \tag{7}$$

A power dissipation density can be assigned to the flow of magnetic flux vortices by the relation

$$P = \frac{E^2}{\rho_f} + J_c E \ . \qquad (8)$$

If flux flow is the only source of power dissipation, this will be the measured power loss of the sample.

The Pb-Cd system is under study here since it affords several sources of possible pinning. When unannealed, the Pb lamellae have been demonstrated to be type II superconductors. It has also been discovered that the Cd lamellae are induced into type II superconducting behavior because of their proximity to the Pb lamellae. The periodic nature of these structures gives rise to a modulated energy gap throughout the samples and, hence, a change in the energy per unit length of flux. This energy barrier is expected to be a "pinner" of vortices. The inhomogeneous concentration of Cd dissolved in the Pb lamellae is expected to cause additional pinning within the Pb lamellae. Another possible source of pinning is the periodic nature of the flux lattice itself. Experiments by Raffy et al. (30,31,32) indicate that matching configurations between the vortex lattice and the periodicity of the solute concentrations of the sample can lead to enhanced critical currents. Martinoli et al. (33,34) studied the behavior of the vortex lattice in superconducting granular Al films with a periodically modulated thickness. Matching configurations in these

experiments also served to enhance critical currents.

The Proximity Effect

If a normal metal N and an adjacent superconducting metal S are in good electrical contact, it is possible for Cooper pairs to "leak" into the normal metal. An exact derivation of the probability amplitude $F = \langle \Psi_{\uparrow} \Psi_{\downarrow} \rangle$ for finding a Cooper pair in the normal metal a distance $|x|$ from the NS boundary was derived by de Gennes (35). The probability amplitude has the form

$$F = \phi(x) \exp(-K|x|) \quad , \tag{9}$$

where $\phi(x)$ is a slowly varying function of x and

$$K^{-1} = \hbar v_{FN}/2k_B T \tag{10}$$

for clean metals or

$$K^{-1} = (\hbar v_{FN} l_N/6\pi k_B T)^{\frac{1}{2}} \tag{11}$$

for dirty metals. It should be stressed that in this model the normal-superconducting interface must represent a good electrical connection and a sharp metallurgical boundary.

In many cases of interest, the effects of the normal metal on the superconducting metal in a NS system can be described using a single parameter called the extrapolation length, b. If the temperatures of interest are close to T_{cS} of the bulk S material, as T_{cNS} must be for thick S films, the linearized Ginzburg-Landau equation can be applied to S. This equation may be written

$$-\alpha(T_{cNS})\Delta = (\hbar^2/2m)\nabla^2\Delta \quad , \tag{12}$$

where $\alpha(T_{cNS}) = (T_{cNS} - T_{cS})\alpha'$. Here α is defined as in the original Ginzburg-Landau equation (36) and is given by

$$\alpha \sim \hbar^2(T - T_c)/(T_c\xi_o^2) \tag{13}$$

for a pure metal. The effect of the normal metal is included in the pair potential boundary conditions by (37)

$$(\nabla - 2ie\ A/c)_n\Delta = (1/b)\Delta \quad , \tag{14}$$

where $(\ )_n$ denotes the component normal to the surface and b has units of length. The extrapolation length b has been shown (35) not to have any singularities at $T = T_{cS}$ and to be independent of temperature and field in the Ginzburg-Landau region $T \sim T_{cS}$. For $d_S >> \xi_{oS}$, the solution yields

$$T_{cNS} = T_{cS} - \pi^2\hbar^2/[8m\alpha'(d_S + b)^2] \quad . \tag{15}$$

The pair potential is not described by a single exponential in the normal metal and may be considered to have a nonzero value for a distance b from the NS interface into the normal metal. Values of b and α' may be obtained from experimental values of $(T_{cS} - T_{cNS})^{-1/2}$ plotted as a function of the superconducting metal thickness.

Another solution of the transition temperature behavior of a NS proximity sandwich was derived by Werthamer (12). Starting with the linear homogeneous integral of de Gennes and Guyon (13) for the pair potential at the transition temperature of a NS sandwich, Werthamer recognized that Δ/NV was continuous across the NS interface which led him to a solution of the equations. For $d_N > K_N^{-1}$, Werthamer found that

$$D_S = (\pi/2)(1 - t)^{-\frac{1}{2}} \cot^{-1}[(2/\pi)(t^{-1} - 1)^{\frac{1}{2}}] \quad , \qquad (16)$$

where $D_S = d_S(\hbar v_{FS} l_S / 6\pi k_B T_{cS})^{-1/2}$, $t = T_{cNS}/T_{cS}$, and $v_{FS} = 5 \times 10^7$ cm/sec for Pb. A linear regression fit to Pb-Cd data indicates that $l_S = 6 \times 10^{-6}$ cm and $T_{cS} = 7.150$K for Pb. When the transition temperature of the NS sandwich is close to the bulk transition temperature of the superconducting metal, equation 16 yields

$$t = 1 - 2.25\ \pi^2/(4D_S^2) \quad . \qquad (17)$$

This result may be easily compared to experimental data for a NS system. However, in the approximations made, this result is insensitive to the normal metal.

Following in the spirit of Martinoli (38), we derive an effective penetration depth $\lambda(x,T)$ for a SNS system with a normal metal in the clean limit. According to de Gennes (39), if we generalize the Ginzburg-Landau (G-L) equations

to N,

$$\lambda_N^{-2}(x,T) = \frac{16\pi e^2}{mc^2}\,\psi_N^2(x,T) \quad . \tag{18}$$

The coordinate system is shown in figure 2. The solution of the G-L equations gives

$$\begin{aligned}\psi_N(x,T) &= \psi_N(0,T)\,\cosh(K_N x) \\ &= \psi_N(d_N/2,T)\,\frac{\cosh(K_N x)}{\cosh(Kd_N/2)} \quad .\end{aligned} \tag{19}$$

The expression for the penetration depth becomes

$$\lambda_N^{-2}(x,T) = \frac{16\pi e^2}{mc^2}\,\psi_N^2(d_N/2,T)\,\frac{\cosh^2(K_N x)}{\cosh^2(K_N d_N/2)} \quad . \tag{20}$$

An essential boundary condition demonstrated by de Gennes (35) is

$$\frac{\Delta_N \text{ Boundary}}{\Delta_S \text{ Boundary}} = \frac{\Delta_{NB}}{\Delta_{SB}} = \frac{(NV)_N}{(NV)_S} \quad , \tag{21}$$

where NV is the BCS electron-electron interaction parameter at the Fermi surface defined by $T_c = 1.14\theta_D \exp(-1/NV)$. This boundary condition is the result of a self-consistent field approximation treating the pair potential as a perturbation on the eigenvalue equations for the system when the temperature is close to the transition temperature of the superconductor. An independent solution of the Ginzburg-Landau-Gor'kov equations by Zaitsev (40) yielded

this same boundary condition for planar superconducting-normal interfaces. According to Fetter and Hohenberg (41), the complex order parameter may be related to the pair parameter close to the transition temperature of S by

$$\Psi(\vec{r}) = \left[\frac{7\zeta(3)n\chi(1.075\ \xi_o/\ell)}{8\pi^2 k_B T_c^2} \right]^{\frac{1}{2}} \Delta(\vec{r}) \quad , \qquad (22)$$

where a strong coupling factor for Pb has been included in the argument of χ, n is the total electron density, the Riemann zeta function (42) $\zeta(3) = 1.202$, and χ is a function described by Werthamer (43). Here $\xi_o = 0.18\hbar v_F/k_B T_c$ is the BCS coherence length. To specialize equation 22 to the Pb-Cd system, we can note that for the clean limit of Cd, $\xi_o/l \ll 1$, so that $\chi = 1$. Also, T_{cNS} is approximately equal to T_{cS}, so $\xi_{oS} \approx \xi_o$. In this limit,

$$\frac{(NV)_N}{(NV)_S} = \frac{\Delta_{NB}}{\Delta_{SB}} = \left\{ \frac{n_S\chi(1.075\ \xi_{oS}/\ell_S)}{n_N} \right\}^{\frac{1}{2}} \frac{\Psi_{NB}}{\Psi_{SB}} \quad , \qquad (23)$$

which can be rewritten as

$$\frac{\Psi_{NB}}{\Psi_{SB}} = \frac{(NV)_N}{(NV)_S} \left[\frac{n_N}{n_S\chi(1.075\ \xi_{oS}/\ell_S)} \right]^{\frac{1}{2}} .$$

The London penetration depth is given by

$$\lambda_L(0) = [mc^2/(4\pi ne^2)]^{\frac{1}{2}} .$$

Substituting the London penetration depths, we find that

$$\frac{\Psi_{NB}}{\Psi_{SB}} = \frac{(NV)_N}{(NV)_S} \frac{\lambda_{LS}(0)}{\lambda_{LN}(0)} [\chi(1.075\ \xi_{oS}/\ell_S)]^{-\frac{1}{2}} \quad . \tag{24}$$

Substituting equation 24 into equation 20,

$$\lambda_N^{-2}(x,T) = \frac{16\pi e^2}{mc^2} \frac{(NV)_N^2}{(NV)_S^2} \frac{\lambda_{LS}^2(0)}{\lambda_{LN}^2(0)} [\chi(1.075\ \xi_{oS}/\ell_S)]^{-1}$$

$$\times \frac{\cosh^2 K_N x}{\cosh^2 K_N d_N/2} \Psi_{SB}^2 \quad . \tag{25}$$

We need to solve for equation 25 in terms of Ψ_{SBCS} .

From the G-L equations solved in S,

$$\Psi_{SB}(T) = \Psi_{SBCS}(T) \frac{1}{\sqrt{2}} \left\{ \left[\frac{\xi_S^2(T)}{b^2} + 2 \right]^{\frac{1}{2}} - \frac{\xi_S(T)}{b} \right\} \tag{26}$$

$$= \Psi_{SBCS}(T)\ A \quad ,$$

where b is the extrapolation length described previously and $\xi_S(T)$ is the coherence length in S. Substituting equation 26 into equation 25 and using the definition for the superconducting penetration depth,

$$\lambda_N^{-2}(x,T) = \lambda_S^{-2}(T) A^2 \frac{(NV)_N^2}{(NV)_S^2} \frac{\lambda_{LS}^2(0)}{\lambda_{LN}^2(0)} [\chi(1.075\ \xi_{oS}/\ell_S]^{-1} \tag{27}$$

$$\times \frac{\cosh^2 K_N x}{\cosh^2 K_N d_N/2} \quad ,$$

where

$$A = \frac{1}{\sqrt{2}} \left\{ \left[\frac{\xi_S^2(T)}{b^2} + 2 \right]^{\frac{1}{2}} - \frac{\xi_S(T)}{b} \right\} \quad . \tag{28}$$

Near T_c, it has been shown (41) that

$$\lambda_S^{-2}(t) = \lambda_{LS}^{-2}(0)\ 2(1 - t)\ \chi(1.075\ \xi_{OS}/\ell_S) \quad , \tag{29}$$

where $t = T/T_c$. The two fluid model predicts that at T close to T_c,

$$\lambda_S(t) = \frac{\lambda_S(0)}{\sqrt{1 - t^4}} \approx \frac{\lambda_S(0)}{2\sqrt{1 - t}} \quad . \tag{30}$$

Comparing equations 29 and 30 at t = 0,

$$\lambda_S(0) = \sqrt{2}\ \lambda_{LS}(0)[\chi(1.075\ \xi_{OS}/\ell_S)]^{-\frac{1}{2}} \quad , \tag{31}$$

giving

$$\lambda_S(t) = \frac{\sqrt{2}\ \lambda_{LS}(0)}{\sqrt{1 - t^4}} [\chi(1.075\ \xi_{OS}/\ell_S)]^{-\frac{1}{2}} \quad . \tag{32}$$

Finally, combining equations 27 and 32, we find that

$$\lambda_N^{-2}(x,T) = \frac{1}{\sqrt{2}} A^2 \frac{(NV)_N^2}{(NV)_S^2} \lambda_{LN}^{-2}(0)[1 - t^4] \frac{\cosh^2 K_N x}{\cosh^2 K_N d_N/2} \quad . \tag{33}$$

The penetration depth in N is very dependent on distance from the center of the N lamella. This spatial dependence of the penetration depth in the normal metal is the result of the rapid spatial variation of the pair potential within

the normal metal and a corresponding change in n_s. Equation 33 predicts that λ has its smallest value at the NS boundary and becomes the largest at the center of the N region in an SNS junction.

The consequences of this predicted penetration depth were studied by Dobrosavljevic and de Gennes (44). They predict that the N material in an SNS system will behave like a type II superconductor in which the field penetrates in quantized vortices, as shown in figure 3a. Their predicted field profile is shown in figure 3b, where ρ is given by:

$$\rho = K_N^{-1}[\ \ln(K_N\lambda_N) - 0.116] \quad . \tag{34}$$

The field at which the flux first penetrates the normal metal is given by

$$H_{c1N} = \frac{\phi_o}{8\lambda_N} \left(\frac{K_N}{a - \rho} \right)^{\frac{1}{2}} (\cosh K_N d_N/2)^{-1} \quad , \tag{35}$$

and the free energy per unit length of flux in N is predicted to be

$$F_1 = H_{c1}\phi_o/4\pi \quad . \tag{36}$$

If the vortex is considered elliptical, it should have a semi-major axis length of $2q_o^{-1}$ and a semi-minor axis length of approximately $d_N - 2\rho$, where

$$q_o^2 = (d_N/2 - \rho)K_N\lambda_B^{-2} \quad . \tag{37}$$

With typical parameters for the Pb-Cd system, the

calculated ratio of semi-major:semi-minor axes is approximately 1.5:1 or 2:1. This theory assumes that the penetration depth varies as $\cosh^{-1}[K_N x]$ from the NS interface and that the semi-minor axis length has the width of the normal lamella as its constraint. Use of variational principle techniques show that q_o^{-1} is the characteristic decay length of the field along the semi-major axis.

It is advantageous to develop a simple picture of how the pair potential behaves in the normal metal. The pair potential is a solution of the following differential equation (45):

$$\frac{d^2\Delta_N}{d\,x^2} - K_N^2\Delta_N = 0 \quad . \tag{38}$$

Solving this equation subject to the appropriate lamellar boundary conditions yields:

$$\Delta_N(x) = \Delta_{N\,min} \cosh K_N X \quad . \tag{39}$$

To make this relation meaningful, it would be useful to relate $\Delta_{N\,min}$ to the pair parameter in the superconductor. Applying the same boundary conditions as before (equation 21), it is found that:

$$\Delta_N(x) = \Delta_{SB} \frac{(NV)_N}{(NV)_S} \frac{\cosh(K_N X)}{\cosh(K_N d_N/2)} \quad . \tag{40}$$

This predicted variation in the pair parameter is shown in figure 2. It must be recognized that this solution is a one dimensional solution and that a three dimensional analysis would have to be made to accurately describe the induced pair potential in the normal metal. This analysis is further complicated as vortices form and move through the normal metal. Such a dynamic solution has not been reported as of this writing. A further complication of this problem is the prediction of how the superconducting pair parameter at the NS boundary compares to the bulk value of the superconducting pair parameter. An analysis of this situation is proposed by de Gennes(39), subject to the conditions that the interface is in the Ginzburg-Landau regime and that the normal metal doesn't screen the magnetic field at the NS interface. The first order approximation implies that the superconducting pair potential changes from the bulk value to the boundary value within approximately a coherence length.

When two superconductors are very loosely coupled together so that only a small supercurrent can pass between them, they are considered to form a weak link. One group of these weak links contains the oxide tunnel junctions

such as those first experimentally studied by Anderson and Rowell (46) and the superconductor-normal-superconductor (SNS) junctions first reported by Clarke (47). These inherently non-superconducting junctions sustain a supercurrent across them even though no voltage exists across the junction. This supercurrent was described by Josephson (5):

$$j_S = j_J \sin \phi \tag{41}$$

where j_J is the Josephson current density and ϕ is the difference between the phases of the two superconductors. Waldram, Pippard, and Clarke (48) proposed a large junction solution in which the electric and magnetic fields and the phase difference are spatially varying throughout the junction. By assuming that for small junction voltages the total current is the sum of the Josephson supercurrent and the injected current, Waldram, et al. were able to show that the conduction in a large junction occurs mainly at the edges of the junction. However, if the vortices are pinned upon entering the junction, this method of solution doesn't define the critical current and solutions involving the balance of flux pinning and Lorentz forces must be employed.

Directional Solidification of Eutectics

The distinctive properties of eutectic composition alloys have attracted the interest of metallurgists. Although these properties vary from system to system, there are certain common properties unique to eutectics which have been studied by metallurgists for many years (49,50,51,52). Because of the author's use of Pb-Cd eutectic composites in this dissertation, a basic understanding of the lamellar growth in eutectic systems is necessary.

The steady state growth of an array of lamellae (shown in figure 4) is the area of particular interest here and is also the easiest situation to model. The conditions imposed by steady state growth must first be considered. From these conditions an appreciation will be developed for the physical properties of the eutectic that control its growth.

Constraints in the solidification of eutectics may be the result of (53):

(i) Steady-state heat flow at the solid-liquid interface,

(ii) Steady-state diffusion in the liquid,

(iii) The maintenance of kinetic equilibrium at the growing interface,

(iv) The presence of $\alpha\beta$ phase boundaries in the solid,

and

(v) The nucleation characteristics of the two phases.

The two phases of the eutectic mixture will probably have different thermal conductivities and different heats of fusion. This implies that the heat flow problem at the solid-liquid interface will impose a constraint on the growth of the lamellae. A measurement of the temperature gradients on the interface will determine if such a constraint exists.

If the solid-liquid interface is approximated by a planar surface, then, according to Tiller (53), it is known from general heat flow calculations involving the thermal conductivities and latent heats of the α and β metals that the two phase interface will appreciably bend the isotherms in the liquid and in the solid only within a distance of the order of a few lamellar periods from the solid-liquid interface. This distortion of the isotherms (figure 5) allows heat flow parallel to the solid-liquid interface to occur in both the liquid and the solid such that the continuity of heat flow boundary condition may be satisfied at both interfaces.

The boundary conditions to be satisfied at the α and β interfaces are

$$K_L \nabla T_L^i + L^i R = K_S^i \nabla T_S^i \quad , \tag{42}$$

where $i = \alpha, \beta$, K_L = thermal conductivity of liquid, K_S^i =

thermal conductivity of the solid, ∇T_L^i = temperature gradient in the liquid ahead of the i phase, ∇T_S^i = temperature gradient in the solid i phase, L^i = latent heat of fusion of the i phase, and R = rate of freezing. The requirement of heat flow continuity across the α interface leads to:

$$(d_\alpha/2)[K_L(dT/dy)_{a-a}] + K_L \int_o^{a-a} (dT/dx)_{c-c}dy + K_S^B \int_{b-b}^{o} (dT/dx)_{c-c}dy + (d_\alpha/2)L^\alpha R = (d_\alpha/2)K_S^\alpha(dT/dy)_{b-b} \quad , \tag{43}$$

where d_α is the width of the α lamellae.

If it is assumed that there is no lateral diffusion in the liquid phase, the solute distributions in the liquid ahead of the α and β lamellae would increase to equilibrium values given by

$$C_L^i = C_E[(1 - k_i)\exp(-R/D)/k_i] + C_E \quad , \tag{44}$$

where i = α, β, C_L^i = concentration of the β constituent in the liquid ahead of the i interface, C_E = eutectic concentration, k_i = partition coefficient of the constituent in the i phase at the eutectic concentration, D = diffusion coefficient of the B constituent in the liquid, R = rate of advance of the interface, and y = distance measured ahead of the interface. Under these conditions, a buildup of the β constituent would occur ahead of the α

phase. If the interface concentrations, C_L^i, and the slopes of the liquidus lines, m_i, are known, the interface temperatures for the two phases may be calculated:

$$T_L = T_E + m_i(C_L^i - C_E) \quad , \tag{45}$$

where T_E is the eutectic temperature. Since $k_\alpha \neq k_\beta$ and $m_\alpha \neq m_\beta$, in general, $T_L^\alpha \neq T_L^\beta$ and one phase must lead the other by a significant amount if no lateral diffusion is allowed.

Another result of no lateral diffusion would be the instability of the lamellae. This is because the interface of one phase will be supercooled with respect to the other phase. Under these circumstances nucleation would either occur on the solid in an epitaxial arrangement with the substrate or in the liquid ahead of the supercooled phase.

However, it is natural to expect a lateral diffusion process as the liquid redistributes the solutes for a uniform liquid composition. According to (54) natural convection is inherent in liquid metal alloys because of their low viscosity and high density. This is a large force in the redistribution of the liquid toward uniform liquid composition. However, it is found that when a fluid flows past a solid interface, the velocity of the fluid right at the surface is always found to be zero (the no-slip condition of fluid dynamics). This implies that even when lateral diffusion is present there will be a

slight buildup of the β constituent ahead of the α phase and vice versa, since the fluid convection velocity parallel to the solid-liquid interface must approach zero at the interface itself.

As the α lamellae freeze, they eject B atoms which will increase the concentration of the β constituent in front of the α lamellae, and vice versa. By allowing the condition of lateral diffusion, we will lower the concentration of α constituent ahead of the β phase and lower the concentration of β constituent ahead of the α phase. This, in turn, makes the interface temperatures, T_L^i, closer to each other (equation 45) and will cause the lead distance between the tips of the lamellae to decrease appreciably.

No assumptions have yet been made about the shape of the solid-liquid interface. The concentration of the liquid at the point of intersection of the solid-liquid interface with the α-β interface is the concentration at which the liquidus lines cross in the phase diagram. Most likely, mechanical equilibrium will occur at this junction to balance the solid-liquid interface tensions and the phase boundary tension. Since the equilibrium condition requires that the α constituent is built up slightly ahead of the β lamellae and vice versa, the interface temperature must be below the eutectic temperature as shown in figure

6. Also, the solid phases will have compositions such that $C_S^{\alpha} > C^{\alpha}$ and $C_S^{\beta} < C^{\beta}$ because of this undercooling. The above arguments imply that the most probable interface profile for steady-state growth is that shown in figure 7. Although lamellar interfaces of completely positive curvature seem to be more probable, occasionally negative curvature interfaces may be necessary under certain conditions of critical constraint. The morphology shown in figure 7 is called nonfaceted/nonfaceted growth and is typical of such systems as Pb-Sn, Al-Zn, and Pb-Cd (54).

An examination of the solute profile is shown in figure 8. The liquid concentration gradients cause the B atoms to move from the regions ahead of the α lamellae to the regions ahead of the β lamellae. In actual eutectic systems, the lamellar spacing is so small that large concentration gradients are not required to produce sufficient diffusion rates for lamellar growth, allowing the liquid concentrations C_L^{α} and C_L^{β} to be very close to C_E. This implies that a faster rate of advance of the solid-liquid interface requires a smaller lamellar spacing to accommodate the required rate of lateral diffusion. One may write the flux of B atoms leaving the α lamellae as:

$$J(\text{reject}) = (1/A^{\alpha}) \frac{dm}{dt} = R(C_L^{\alpha} - C_S^{\alpha}) \approx R(C_E - C^{\alpha}) \quad , \quad (46)$$

where A^{α} is the area of the α-liquid surface, R is the rate of interface advance, and C_E and C^{α} are defined in figure

6. A similar expression holds for the flux of A atoms leaving the β lamellae. To calculate the lateral diffusion of these rejected atoms, the equation for three dimensional diffusion must be written:

$$\frac{d^2C_L}{dy^2} = \frac{R}{D}\frac{dC_L}{dy} = 0 \quad , \tag{47}$$

where D = diffusion coefficient. This equation has been solved rigorously, subject to the boundary conditions at the solid-liquid interface, by Jackson and Hunt (55), but this presentation will detail only a first order analysis following the ideas of Zener (56). The lateral diffusion of the ejected A and B atoms will occur mostly in the x direction, parallel the interface. This can be approximated by

$$J(\text{diff}) = D\Delta C/(d/2) \quad , \tag{48}$$

where ΔC is some mean composition difference in the liquid between the α and β interface fronts, and the diffusion distance has been approximated by $d/2$. When a steady-state condition is reached the flux of B atoms from the α lamellae will equal the lateral diffusion flux transporting the B atoms to the β phase. This means that

$$J(\text{diff}) = J(\text{reject}) \quad . \tag{49}$$

Solving, one finds that

$$R = 2D\Delta C/[d(C_E - C^{\alpha})] \quad . \tag{50}$$

In order for a pure metal to freeze, the liquid-->solid reaction must be larger than the solid-->liquid reaction at the interface. This requires a small supercooling ΔT_K, which is called kinetic supercooling. When the metal freezes at a supercooling of ΔT_K a free energy $\Delta G = \Delta S_f \Delta T_K$ is released. This free energy is required to cause a net atomic reaction rate from liquid to solid, an irreversible process. When a eutectic freezes, then, there are three irreversible processes, each of which requires energy:

(i) A net atomic reaction rate from liquid to solid,

(ii) Diffusion in the liquid ahead of the α and β phases, and

(iii) Generation of the α-β interface area between the two solid phases.

The additional energy for eutectic growth is obtained by additional supercooling, so when a eutectic freezes the free energy released is given by

$$\Delta G_B = \Delta S_f \Delta T_E \quad , \tag{51}$$

where ΔS_f is the freezing entropy per unit volume of the eutectic liquid and ΔT_E is the undercooling of the liquid at the freezing interface. The free energy, ΔG_B, released is used to drive irreversible processes (i), (ii), and (iii) above. In the case of regular eutectic growth which

we are considering, process (i) is negligible compared to processes (ii) and (iii) . Consider the interface of figure 7 having advanced a distance dy in the y-direction and an energy balance is calculated on a volume (d)(L)(dy):

(i) Free energy released is given by $(\Delta G_B)(d)(L)(dy)$,

(ii) Free energy to produce two α-β interfaces is given by $(2\gamma_{\alpha\beta})(L)(dy)$, and

(iii) Free energy to drive diffusion is given by $(\Delta G_d)(d)(L)(dy)$,

where $\gamma_{\alpha\beta}$ is the α-β phase boundary surface tension and ΔG_d is the free energy per unit volume used to drive the diffusion process. Equating the released and absorbed free energies gives:

$$\Delta G_B = 2\gamma_{\alpha\beta}/d + \Delta G_d \quad . \tag{52}$$

If all the free energy ΔG_B released went into forming α-β interfaces, there would be a maximum amount of α-β surface area per unit volume and therefore the lamellar spacing would be a minimum, $d = d_{min}$. If these numbers are substituted into equation 52, the result is

$$d = d_{min} = 2\gamma_{\alpha\beta}/\Delta G_B \tag{53}$$

which is the minimum possible spacing for the eutectic lamellae. Substituting equations 51 and 53 into equation 52 gives

$$\Delta G_d = \Delta S_f \Delta T_E [1 - d_{min}/d] \tag{54}$$

which is the free energy to drive the lateral diffusion process.

A total supercooling was defined above to determine the total amount of free energy available to drive the eutectic reaction. This free energy was divided, to first approximation, into two parts for surface energy and diffusion. Hence, ΔT_E may be thought of as being divided into two parts ΔT_S and ΔT_D, where ΔT_S is the amount of supercooling needed to drive the surface generation and ΔT_D is the amount of supercooling needed to drive the diffusion process,

$$\Delta T_E = \Delta T_D + \Delta T_S \quad . \tag{55}$$

The concentration difference available for lateral diffusion is shown on figure 8. From the geometry involved, it may be calculated that

$$\Delta C = \Delta T_D \left[\frac{1}{|m_\alpha|} + \frac{1}{|m_\beta|} \right] \quad . \tag{56}$$

Equation 54 may be rewritten as

$$\Delta T_D = \frac{\Delta G_d}{\Delta S_f} = \Delta T_E \left[1 - \frac{d_{min}}{d} \right] \quad . \tag{57}$$

Substituting equations 56 and 57 into equation 50, it is found that the rate may be expressed as

$$R = \left[\frac{1}{|m_\alpha|} + \frac{1}{|m_\beta|} \right] \frac{2D\Delta T_E}{(C_E - C^\alpha)d} \left[1 - \frac{d_{min}}{d} \right] \quad . \quad (58)$$

The constants in equation 58 may be lumped into one constant and the eutectic supercooling, ΔT_E, may be rewritten as

$$\Delta T_E = \frac{(\text{constant})Rd}{(1 - d_{min}/d)} \quad . \quad (59)$$

Since the rate of solidification may easily be controlled at a constant value in the lab, ΔT_E is only a function of the spacing d and is typically about 0.02°C for nonfaceted-nonfaceted interfaces. This gives rise to a concentration difference ΔC_E of about 0.018 at/o in Pb-Cd eutectic alloys to drive the diffusion. Tiller (53) first proposed that the spacing would reach a value to minimize undercooling at the interface. Although this is not supported by any clear theory, the principle is supported by experiment and the optimum spacing is given by finding the minimum for ΔT_E by taking the derivative of equation 59 and equating to zero. This shows that

$$d_{opt} = 2d_{min} \quad . \quad (60)$$

Now, the relations

$$d_{min} = \frac{d_{opt}}{2} \quad , \quad d = d_{opt} \quad , \quad \text{and} \quad (61)$$

$$\Delta S_f \Delta T_E = \Delta G_B = 2\gamma_{\alpha\beta}/d_{min} = 4 \frac{\gamma_{\alpha\beta}}{d_{opt}} \quad (62)$$

may be substituted in equation 58 to give

$$R = \left[\frac{1}{|m_\alpha|} + \frac{1}{|m_\beta|} \right] \frac{4\gamma_{\alpha\beta}D}{\Delta S_f (C_E - C^\alpha) d_{opt}^2} \quad , \tag{63}$$

which may be rewritten as

$$d_{opt} = \frac{\text{constant}}{\sqrt{R}} \quad , \tag{64}$$

Equation 64 agrees well with experiments investigating eutectic structures, including experiments at Iowa State University on Pb-Cd (57) and the results of this dissertation illustrated in figure 9. The phase diagram for Pb-Cd (58) is shown in figure 10. Above $d \gtrsim 10$ μm the lamellar structure becomes wavy and discontinuous. Lamellar spacings have been reported from 0.1 μm to greater than 8 μm for Pb-Cd (57).

EXPERIMENTAL SYSTEM AND PROCEDURE

Directional Solidification Apparatus and Procedure

All the samples were directionally solidified on the vertical solidification apparatus shown in figure 11. A strip of the alloy to be solidified was sealed in a stainless steel tube of 0.012 inch to 0.020 inch wall thickness, 0.25 inch to 0.63 inch wide, and 6 inches to 8 inches long. The bottom of the sample tube was clamped to the lower support rod as shown in figure 12. The cooling cylinder sealed water tight around the sample with a neoprene seal at the top and around the lower support rod with an O-ring seal at the bottom. These water seals had to be kept lubricated to prevent sticking which could cause variations in the rate of movement of the solid-liquid interface. A hollow lava spacer to control the temperature gradient rested on top of the clamping plate of the neoprene water seal. On top of the lava spacer was a stainless steel jacket which contained a thermocouple that regulated the furnace temperature. The furnace used to heat the alloy was 20 cm in height and contained noninductively wound nichrome wire heating elements. A transite spacer on the top plate of the water chamber supported the furnace.

The samples were all made from a eutectic composition of 82.6 wt/o Pb and 17.4 wt/o Cd (72 at/o Pb and 28 at/o Cd). Initially a master alloy was cast in 5mm Pyrex tube from high purity materials: nominally 99.999% pure Pb from Cominco (Lot EM2287) and nominally 99.999% pure Cd from Cominco (Lot HPM2437). A total of about 300 grams of the starting materials were weighed and placed into a Pyrex crucible. The crucible was transferred to a vacuum chamber situated in a resistance furnace. After the chamber was evacuated, it was backfilled to approximately one half atmosphere of argon. The Pb-Cd alloy was then melted by the furnace heated to 350° C. At 350° C, the vacuum chamber was completely backfilled to one atmosphere of argon. When the melting was complete, a tantalum stirring rod with a paddle attached was lowered into the melt and oscillated to insure complete mixing. The stirring rod was then removed from the melt and the end of a 5mm Pyrex tube was inserted into the melt. The tube was then evacuated, drawing the Pb-Cd alloy into the Pyrex tube. The alloy rapidly solidified in the Pyrex tubes which were then removed from the vacuum chamber and allowed to cool.

The alloy was removed from the tubes by carefully breaking the glass tubes. The cast alloy rods were then rolled in a rolling mill to the desired thickness, which varied between 0.0005 inch and 0.0020 inch for use in the

directional solidification apparatus.

The stainless steel molds were made from flattened 7/16 inch o.d.-0.020 inch wall stainless steel tube cut to 6 inches or 8 inches in length. Each stainless steel tube was first partially flattened and a piece of 0.010 inch copper sheet was inserted into the center of the tube. The tube was then flattened onto the copper sheet with the rolling mill. Great care had to be exercised not to roll the tubes too much, since the tubes had a tendency to develop curves when over-rolled. The copper was removed from the tubes using a 50 v/o nitric acid-water solution. When the copper was completely dissolved, the tubes were sealed into a 22 mm quartz tube under vacuum and annealed for one half hour at 1100°C to remove strains developed from the cold rolling.

The flattened Pb-Cd alloy was then cut to fit inside the flattened stainless steel tubes. The cut Pb-Cd foil was then coated with graphite-methanol solution to prevent the melted alloy from sticking to the inside of the stainless steel tube. After the methanol evaporated, leaving the graphite coating the surface of the Pb-Cd, the foil was drawn into the stainless steel tube using a 0.001 inch feeler stock.

The tube was then inserted into a vacuum chamber heliarc welder and fastened into place using a copper clamp

which also served as a heat sink. The chamber was evacuated and allowed to pump to approximately 30 millitorr pressure and then backfilled to an absolute pressure of 0.75 atmosphere of He gas. One end of the stainless steel tube was then arc-welded shut and the sample was removed from the chamber. The weld was ground smooth and inspected for leaks. A rolling mill was used to flatten the tube onto the Pb-Cd foil, again exercising care not to over-roll the sample. A #41 hole was drilled into the other end of the tube to fit the sample anchor in the solidification apparatus. Both the end of the tube and the hole were then sealed with Dow Corning 732 RTV silicone rubber or by heliarc-welding to prevent moisture from entering the tubes.

The sealed tube was then screwed to the sample anchor in the directional solidification apparatus described elsewhere. After the cooling water was turned on, the furnace was heated to 500°C. The solidification runs were all carried out at constant rates of solidification to grow uniform lamellar spacings in the samples. The rate could easily be determined by using a stopwatch and a dial indicator which was accurate to 0.001 inch or by using a teletype interfaced into the system.

Sample Preparation

When the directional solidification run was completed, the stainless steel tube was removed from the apparatus and taken to a sheet metal shear where the edges and ends of the tube were very carefully sheared off. This process exposed the directionally solidified duplex structure in the form of a thin foil covered with graphite. Much of the graphite could be removed by carefully swabbing and ultrasonically cleaning in methanol. The desired shape of the sample needed was carefully outlined on the surface and then cut out with a new razor blade with sharp corners using a small steel straight edge as a guide for the razor blade.

The cut sample was then carefully grasped with a tweezers and painted with microstop lacquer on all surfaces except the edges cut with the razor blade. The edges were then electropolished for 1 to 1.5 minutes at 30 volts in a 1 v/o perchloric acid-methanol bath maintained at -60°C by a flow of liquid nitrogen controlled by an alumel-chromel thermocouple in the polishing bath itself. Any smearing effects caused by the razor blade when the sample was cut out were removed by severely electropolishing the edges of the sample. The edges were examined in a microscope to ascertain that the "smearing" on the edges of the sample had been removed, then the sample was placed in acetone and

the microstop lacquer was removed from the surfaces by ultrasonically cleaning the sample. Each of the broad surfaces of the sample was remasked, in turn, as the other broad surface was carefully electropolished using 5 second intervals and then carefully examining the surface for severe defects and improper surface cleaning.

The sample was next mounted on a substrate for the experiment by soldering to indium tabs which had previously been mounted on a properly cut glass slide using GE 7031 varnish. The soldering process was carried out using a soldering iron with a tip prepared for use with indium solder. The temperature of the soldering iron was controlled by a variac which was set at about 65 % of full scale. Copper heat sinks were placed on the sample to protect all portions of the sample from excessive heating except that portion which was being soldered. A small drop of Indalloy Flux #4 was applied to the region of the sample being soldered and the soldering iron was lowered to the sample with a drop of heated indium on the tip. The drop of heated indium was allowed to touch the sample until the sample just began to melt, at which time the soldering iron was removed, making a good solder joint. Scanning electron microscope (SEM) micrographs revealed that the lamellar structure of the sample remained undisturbed except adjacent to the region where the joint was made.

Connections could easily and safely be made to the sample using this type of indium solder joint, eliminating the problems of contact resistance, silver paint smear and cracks, and other annoyances of painted contacts.

A portion of the lamellar structure near the sample was removed and electropolished on one surface. This piece of Pb-Cd was viewed in the SEM to measure the lamellar spacing of the sample. In this manner the dependence of the lamellar period on the solidification rate in figure 9 was shown to be

$$d(\text{angstroms}) = 500[R(\text{cm/sec})]^{-\frac{1}{2}} \tag{65}$$

High Current Cryostat

The high current and magnetic field properties of the Pb-Cd specimens were studied in the apparatus shown in the block diagrams of figures 13 and 14. Both the sample and the thermometer were in direct contact with the helium-4 bath. Temperature control of the cryostat between 2.2K and 4.2K was accomplished by pumping directly on the bath through a manostat with a large ballast (59,60). The large ballast allowed very stable temperature control. The temperature was never observed to drift more than 2mK during the measuring time interval at a fixed temperature.

The temperature was measured with a germanium resistance thermometer (GR20601) which was near the sample

in the helium bath. The thermometer was previously calibrated by Delfs (61) below 18K against the paramagnetic salt temperature scale of Cetas and Swenson (62) and between 18K and 77K against the NBS 1955 platinum resistance thermometer scale. These data were fit to

$$\ln T = \sum_{n=1}^{9} A_n (\ln R)^{n-1} \qquad (66)$$

with a rms deviation of less than 1 mK. The temperature was determined from the thermometer's resistance using computer generated tables based on this polynomial fit.

A Leeds and Northrup K-3 potentiometer was used in a 4 terminal arrangement to measure the thermometer's resistance. A Keithley 150B null detector was used to determine the potentiometer null. The measurements of resistance were accurate to ±0.025%, which implies a maximum temperature uncertainty of ±1mK in the temperature range of 2K to 4.2K. No self-heating effects were observed in the thermometer. A 4 terminal arrangement was used to measure the V vs. I and V vs. H characteristics of the samples. The current was supplied to the sample through two 250 amp vapor cooled, superconducting current leads (63). The sample voltage was read directly on the y-axis of a Hewlett-Packard 7000 AMR x-y recorder. The accuracy of the HP 7000AMR x-y recorder was ±0.2% of full scale, which gives a maximum error of ±2 microvolts on the most

sensitive scale (50 microvolt/cm).

The apparatus for recording V vs. I (I-V) plots is shown in the block diagram in figure 13. Current was supplied to the sample with a Harvey-Wells CFC-100 constant current supply designed for use with a superconducting solenoid. The current could be controlled manually or with an electronic ramp up to 100 amps. The output of a Keithley 150B microvolt meter monitoring the sample voltage was used to drive the quench control of the constant current supply. The output of the Keithley 150B was calibrated such that a full scale deflection of the meter would cause the activation of the quench control, thereby discontinuing the flow of current to the sample. This procedure prevented the destruction of the sample through excessive Joule heating within the sample.

The x-axis of the x-y recorder was driven by the voltage generated across a 0.001 ohm standard resistor in series with the sample. By simply ramping the current, a V vs. I plot could be generated.

A uniform magnetic field up to 14 KOe could be applied to the sample from a Systron-Donner Alpha magnet with flat 11 inch pole faces. The magnetic field was measured near the center of the pole faces with a Rawson Type 720 rotating coil gaussmeter. Fields could be determined with an accuracy of ±1% with this rotating coil gaussmeter. By

incrementing either the temperature or the magnetic field, families of V vs. I plots were generated.

Figure 14 shows the block diagram representing the apparatus which generated V vs. H plots. The sample current was controlled manually and measured with a voltmeter. The x-axis of the x-y recorder was driven by the output of the rotating coil gaussmeter which was rectified to a dc voltage. A ramp generator controlled the field applied to the sample. Changing the current or the temperature in increments allowed the generation of families of V vs. H plots.

Critical Current and Critical Field Measurements

Because of the high anisotropy of the lamellar Pb-Cd eutectic system, a great deal of information characterizing this structure may be obtained by making resistive measurements in two orthogonal geometries. Passing the transport current parallel to the lamellae and then perpendicular to the lamellae are the most apparent geometries to measure.

If the transport current is passed parallel to the lamellae, then one might surmise that any fluxoids or bundles of flux forming from self-field effects or an applied magnetic field should be pinned at the sharp phase interfaces between the Pb-Cd lamellae (64,65,22). SEM

micrographs show that these interfaces can be expected to be defined on the order of 10 angstroms. A critical current could be defined when the Lorentz force on these flux bundles exceeds the pinning forces and the flux bundles start moving across the sample (66).

To study the phenomena occurring when a transport current is passed parallel to the lamellae, samples were prepared so that a 4 terminal resistive measurement could be made. Shown in figure 15 is the sample geometry employed. The Pb-Cd lamellar structures were purposely grown in such a manner so that the Pb-Cd adhered to the stainless steel molds on one surface. This was done to provide a material with relatively low conductivity to shunt any hot spots which might form in the Pb-Cd and to promote self-healing of these hot spots. This is a technique employed in commercially available superconducting cable. The samples were stored in liquid nitrogen from the time of removal from the directional solidification apparatus until they were prepared for the experimental measurements. The samples were normally at room temperature less than one half day while being prepared for the experiment. First, they were cut into the proper geometry for a 4 terminal measurement, then they were electropolished to clean the surface of oxides and graphite so that it could be microscopically ascertained

that the lamellar structure was good. Superconducting Nb-Ti wire was soldered to the sample to provide high current input into the sample. Indium solder was used to make the joints, since In would wet the Pb-Cd at a temperature lower than the melting point of the Pb-Cd. This guaranteed the Pb-Cd lamellar structure would remain undisturbed away from the joint. A large surface area was provided between the In and Pb-Cd to minimize heating in the normal In metal. No heating was observed due to the In. The resistivity of the annealed hypodermic stainless steel was 54.1 $\mu\Omega$-cm in the temperature range 2.2K to 4.2K and for magnetic fields between 0 Oe and 10 KOe. The magnetoresistance was less than $\Delta\rho/\rho = 0.002/KOe$, which is negligible compared to the magnetoresistance expected for Pb-Cd (67,68,69,70). However, the total resistance of the stainless steel substrate is comparable to the Pb-Cd sample and must be subtracted from the total resistance to find the resistance of the Pb-Cd lamellar sample. Indium solder was used to solder #30 copper wires to the samples for voltage leads. All wires in the magnetic field had to be tightly twisted in pairs to minimize the induced emf's caused by the rapidly changing magnetic field.

This geometry allows the measurement of the resistance of an equal number of Cd lamellae and Pb lamellae in parallel. Because the resistivity of the Pb lamellae is

approximately 40 times that of the Cd lamellae, and the volume fraction of Pb is only 4 times the volume fraction of Cd, the parallel resistance is dominated by the behavior of the Cd.

Helium-3 Cryostat

A conventional helium-3 refrigerator (71) was used to measure low power characteristics of the Pb-Cd lamellar system over a temperature range of 10K to 0.3K. Figure 16 shows the physical details of the low temperature tail of the helium-3 cryostat. The principles of operation of this system are described in various texts (72,59,60). The operating efficiencies have been discussed by Haskell (73) for the particular system used in this experiment, therefore, only the details of this experiment will be discussed here.

The Pb-Cd lamellar sample was mounted on a glass substrate using indium solder tabs and GE7031 varnish. The glass substrate was secured with Apiezon N grease to the copper sample holder which was in good thermal contact with the helium-3 chamber. A germanium resistance thermometer was mounted in a close fitting hole in the copper directly behind the substrate. Good thermal contact between the thermometer and the copper was achieved using Apiezon N grease. Temperature control in the sample holder was

achieved using two carbon resistors: one as a thermometer and one as a heater, both located above the sample in the copper block. The good thermal contact of the various components of the helium-3 cryostat and the observed response times assure that the thermometer readings measure the true temperature of the substrate and the sample. The electrical leads in the cryostat were thermally anchored with GE7031 varnish at the helium-3 chamber and again at the helium-4 chamber to reduce thermal gradients in the leads and, therefore, to reduce the heat leak to the sample.

The primary thermometer for this work was germanium resistor GR1592. The thermometer was calibrated by Finnemore (74) in the range 4.2K using paramagnetic salt thermometry and He vapor pressure. The thermometer was calibrated against the germanium thermometer GR65 in the temperature range 4.2K to 20K (3). The calibration points were fit to equation 66 with a rms deviation of less than 0.002K over the entire range of temperatures (73). The temperature was determined from the resistance of the thermometer using a computer-generated table for the polynomial fit. A Leeds and Northrup K-3 potentiometer was used in a four terminal arrangement to measure the resistance of the germanium thermometer. A Fluke 845AB null detector determined the potentiometer null. A

measuring current of 10 μA was used for temperatures above 1K and 1 μA was used below 1K. No self-heating effects were observed in the thermometer using these measuring currents. These measurements were accurate to ±0.025% which causes a maximum uncertainty in the temperature of approximately ±0.003K for temperatures under 10K.

Temperature control of the system above 4.2K was achieved using a 3 wire, lead compensated Wheatstone bridge. The control thermometer resistance, a 470 Ω Spear carbon resistor described elsewhere as SR-2 (74), was balanced against a decade resistance. The off balance signal of the bridge was detected and amplified by a Fluke 845AR null detector. The output of the null detector operated a microswitch which controlled the amount of current flowing through a 50 Ω carbon resistor used as a heater. The heater current was adjusted so that the Joule heating in the resistor nearly balanced the heat loss of the cryostat. If the sample cooled, the heater current was increased to compensate for the cooling until the bridge was again balanced.

For temperatures between 1K and 4.2K, temperature control could be achieved by regulating the helium-4 vapor pressure above the liquid helium in the helium-4 chamber. This regulation was accomplished by pumping on the helium-4 chamber through a manostat (60). More sensitive

temperature control was developed using the control bridge and heater in conjunction with the helium-4 cooling system. The helium-3 system could be used to cool the sample to temperatures between 0.3K and 1K. The vapor pressure above the liquid in the helium-3 chamber was controlled by pumping through a series of needle valves. More sensitive control was achieved, as before, using the control bridge and the heater. At low temperatures, the most precise temperature control was maintained because both the germanium and carbon thermometers are most sensitive in this region.

Proximity Effect Measurements

The characterization of the electrical properties of the Pb-Cd eutectic lamellar structures may be completed by studying the resistivity and critical current with the transport current flowing perpendicular to the lamellae. The sample geometry is shown in figure 17. Because the Cd is a normal metal above 0.5K, it is desirable to study how the superconducting Pb affects the Cd when the two metals are in very good electrical contact with a sharply defined interface between them. The proximity effect predicts that Cooper pairs will exist in the normal Cd lamellae for a finite lifetime, so the Cd will display some superconducting properties (45,75,76). Because the

resistivity of Pb is approximately 40 times as large as the resistivity of the Cd and the volume fraction of Pb is only 4 times that of Cd, the Pb resistance is expected to dominate the sample resistance in this geometry.

A 4 terminal measuring technique was used to study the electrical properties of the Pb-Cd lamellar structures in the perpendicular current geometry. The sample (shown in figure 17) was cut from a highly aligned region of directionally solidified Pb-Cd using a sharp razor blade. The Pb-Cd was stored in liquid nitrogen until prepared for the experiment. The cut sample was severely electropolished along the edges to remove the smearing caused by the razor blade cross-cutting the lamellae. Preferential electropolishing was achieved by masking regions not to be electropolished with Microstop lacquer. The sample was connected electrically and mechanically with In solder to In solder tabs mounted on the substrate. Apiezon N grease was applied to guarantee good thermal contact between the sample and the substrate.

Low sensitivity measurements were made on the sample using a Leeds and Northrup K-5 potentiometer in a 4 terminal arrangement to measure the resistance of the sample. A Guildline Type 5214 photocell galvanometer amplifier and a Guildline Type SR21 secondary galvanometer determined the potentiometer null. A current was supplied

to the sample from a constant current supply of Ames Lab design (Ames Lab circuit design #MF369). The voltage measurements were accurate to ±0.0037% with a resolution of ±0.05 microvolt in the voltage range used. The maximum current normally attainable without heating effects in the helium-3 cryostat was approximately 300 mA.

Superconducting Nb-Ti wires were used to carry current to the sample and to reduce Joule heating in the current leads. The voltage leads were #36 copper wire tightly twisted together to eliminate induced emf pickup. All voltage connections were made with all copper connecting joints or low thermal solder. Magnetic fields up to 80 Oe could be applied to the sample by coils mounted on the vacuum can. The critical current was studied as a function of temperature and magnetic field. V vs. I curves were plotted for each sample for several magnetic fields and temperatures. The resistivity was measured for each sample as a function of temperature for several currents in increasing magnetic fields. In this manner the transition temperature was determined resistively for the samples.

Very sensitive studies of these samples were carried out using a superconducting quantum interference device (SQUID). The particular SQUID used was a System 330 manufactured by S.H.E. Corporation. Connected and operated in the helium-3 cryostat as a voltmeter, the SQUID had a

voltage gain of 10^8 and a resolution of ±10 picovolts. A complete discussion of the theory of SQUID operation is given elsewhere (77) and will not be elaborated upon here. Current was supplied to the sample with a Model CCS constant current supply manufactured by S.H.E. The SQUID output was detected using a Keithley 172 digital multimeter. Because of the nature of a SQUID apparatus, currents above 20 mA caused Johnson noise levels which interrupted SQUID operation. This very sensitive nature of the SQUID requires that all sample leads are very tightly twisted together and shielded from rf signals everywhere in the circuit. All SQUID leads in the cryostat consisted of pairs of tightly twisted 0.003" diameter annealed Nb wire inside 0.013" diameter bore 60% Pb, 40%Sn tubing. Except for sample connections, all connections were made to Nb terminals with screws inside machined Nb shields. The length of wires from the SQUID probe to the sample should be minimized so as to minimize parasitic inductances and capacitances in the cryostat. The sample was specially shielded from rf radiation using a grounded copper foil shield. The thermometers in the cryostat represented especially good antennae for rf radiation and were carefully shielded with Pb foil to effectively shield any thermometer-received rf noise from the sample. The Pb foil shielding was far enough from the sample so as not to

effectively distort any magnetic fields applied to the sample.

The sample preparation and geometry is the same as described previously in this section, with the exception of the current and voltage leads. Because Nb wire does not solder readily to In, manganese tabs were spot welded to the Nb wires. The manganese tabs were then liberally covered with In and soldered to the In solder tabs on the sample substrate.

The measurements made with the SQUID were 4 terminal measurements as described previously with the exception that the SQUID had a much better resolution than the K-5 potentiometer. Critical currents were determined when the sample voltage reached a level of 20 picovolts with various temperatures and applied magnetic fields. The V vs. I characteristics were plotted for several magnetic magnetic fields and temperatures. Resistance measurements were made for several currents as a function of temperature at various magnetic fields. The best resistance resolution with the SQUID was $\pm 5 \times 10^{-10}\ \Omega$ as operating in this cryostat. This is approximately 5 orders of magnitude more sensitive than needed to measure the expected resistance of the Cd lamellae in the normal state.

RESULTS AND DISCUSSION

Sample Quality

The directional solidification technique described previously is a very successful method of growing lamellar Pb-Cd eutectic structures with the lamellae all aligned perpendicular the broad sample surface. The size of the samples with aligned lamellae could be as large as 4 cm long by 1 cm wide by 0.005 cm thick, where length is measured parallel to the lamellae. SEM micrographs indicate that the phase boundaries are very sharp (on the order of 10 angstroms) and that the lamellae align themselves very much as expected from theory (figure 18a,b,c). However, SEM electron channeling techniques indicate that the lamellae within a single domain may be misaligned by as much as 1^{o}. The experiments conducted here indicate that 0.5 micron is the minimum lamellar period which can be achieved by this technique with the lamellae still oriented perpendicular to the broad sample surface. Using faster solidification rates, the lamellae tend to orient at acute angles with respect to the broad surface to the sample (figure 18d). This type of orientation was not demonstrated to grow in large single grains as the experiments demanded. Lamellar periods much larger than 10 microns were not achieved because uniform

solidification speeds were difficult to achieve below 0.5×10^{-4} cm/sec.

Initially, the problem of making electrical contact to the samples without destroying the lamellar structure was of concern. Indium was found to be a satistactory low temperature solder. By carefully soldering the electrical leads to the sample using copper heat sinks, it was found that no structural damage was caused to the sample away from the solder joint.

Because these structures are formed by cooling the alloy through a sharp temperature gradient, the Cd solute is supersaturated in the Pb phase at room temperature. Samples stored at liquid nitrogen temperatures or below show no change in electrical or thermal conductivities in time, but samples allowed to anneal at room temperature show marked changes in their transport properties. SEM micrographs of annealed samples show small cellular precipitates of Cd forming within the Pb lamellae as the Cd diffuses out of the Pb (figure 19). Annealing appears to have little effect on the Cd lamellae or on the Pb solute within the Cd lamellae. No precipitation of the Pb within the Cd phase was noticed. The Pb-Cd structures have been shown to have a Ginzburg-Landau parameter, κ, as high as 1.5 before any annealing has been allowed to take place. Upon annealing, κ has been seen to drop below 0.70,

indicating that the precipitation of the Cd out of the Cd-rich Pb phase is causing the Pb lamellae to change from type II to type I superconductivity. This effect will be further discussed in later sections.

An attempt was made to control the mean free path of the electrons in the Cd by alloying. Cadmium does not readily form solid solutions in any concentration with many metals. During directional solidification of the Pb-Cd eutectic, the phase diagram predicts that 0.14 at/o Pb will go into solid solution in the Cd lamellae. This concentration of Pb does not significantly change the resistivity of the Cd. In an attempt to further increase the resistivity of the Cd phase, dilute concentrations of Mg were alloyed into the Pb-Cd eutectic. The solubilities of Mg in Pb and Cd were seen to be about equal. Magnesium forms a solid solution at all concentrations with Cd, so Mg was a likely candidate for alloying.

Alloys containing enough Mg to form concentrations of 0.25 at/o, 1.0 at/o, and 2.0 at/o were cast and then directionally solidified. The resultant structures were lamellar, but no significant change in the Cd resistivity was detected. The resistivity of the Cd lamellae with Pb solute remained approximately 0.056 μΩ-cm regardless of the Mg concentration. It is seen that Mg and Cd have the same valence and approximately the same atomic radii, so it can

be assumed that these factors facilitate the formation of the Mg-Cd solid solution, but limit any increase in the electrical resistivity. In order to determine the effect the Pb solute has on the Cd phase, a series of alloys of Cd with dilute concentrations of Pb was cast into 0.015" rods and the resistivity measured. The results are shown in figure 20. Increasing amounts of Pb are seen to increase the resistivity of the Cd. This is consistent with Nordheim's concentration rule (78) which states that for a small, homogeneous concentration x of solute atoms in a solvent metal, the resistivity is proportional to x(1-x). A linear regression fit indicates that at 4.2K, the resistivity of the Cd is given by $\rho \approx 0.120\ (x)\ \mu\Omega\text{-cm}$, where x is the amount of Pb solute in the Cd measured in wt/o. The resistivity of pure Cd was not measured, but the linear regression fit yields a pure Cd resistivity of 0.0022 microhm-cm. A calculation of the resistivity of the Cd-rich phase of the Pb-Cd eutectic system from this linear regression fit predicts a resistivity of 0.032 $\mu\Omega$-cm, somewhat lower than the 0.056 $\mu\Omega$-cm resistivity value measured for the Cd-rich phase in the eutectic lamellar structures.

When a transport current is passed through a Pb-Cd sample perpendicular to the lamellae, the resistance of the sample is mostly a measurement of the resistance of the Pb

lamellae in series. The low resistivity and small volume fraction of the Cd dictates that the resistance due to the Cd lamellae will be approximately 2% to 3% that of the Pb. Therefore, in this series electrical measurement, the Cd resistance will only be detectable when the Pb is in a nearly superconducting state. A series of measurements was made to determine the dependence of the Pb resistivity on the lamellar period. The results are shown in figure 21. At 8K, the Pb resistivity typically had a value of 2 microhm-cm. Scatter in the data is due to the uncertainty in accurately measuring the geometries of the various samples studied. These data indicate that the percentage of Cd dissolved in unannealed Pb lamellae is a constant, independent of the directional solidification rate. Measurements were also made of the total Pb-Cd sample resistivity with the transport current parallel to the lamellar structure. The total sample resistivity is shown in figure 22 as a function of lamellar spacing. For solidification rates which yield lamellar periods of less than 1 micron, the sample resistivity is seen to rise. If the lamellar period is larger than 1 micron, the sample resistivity is approximately constant. This result has been independently observed by Zaitlin (4) and is thought to be the result of a supersaturation of Pb in the Cd lamellae because of the extremely rapid solidification

rates involved.

Very little is known, as of this writing, about the crystallography of the directionally solidified Pb-Cd structures. Electron beam channeling studies done on Pb-Sn by Mourer (79) indicate that there are four idealized eutectic crystallographic relationships displayed in the Pb-Sn lamellar system. The study of the crystallography in the Pb-Cd eutectic lamellar structures has been limited because the width of the Cd lamellae cannot easily be made large enough to allow adequate resolution for crystallographic techniques.

Magnetization measurements made by the author and by Livingston (80,81) on Pb-Cd eutectic alloys confirm the change of the Pb lamellae from type II superconductivity (as quenched) to type I superconductivity (as appropriately annealed). H_{c2} is seen to drop from a quenched value of 1800 Oe (figure 23) to 1300 Oe with three hours of room temperature annealing. The precipitation rate appears to slow after the first few hours at room temperature. H_{c2} was seen to approach bulk Pb critical field values after approximately one week of annealing at room temperature.

Superconducting Transition Temperature

A number of experiments (82,83,84,3,85) have shown that the superconducting properties of normal and

superconducting materials in good electrical contact are noticeably different from the original isolated metals. The transition temperature of the superconducting metal is depressed and superconductivity is induced into the otherwise normal material. These effects were both apparent in our Pb-Cd lamellar structures. The superconducting transition temperatures were determined by linearly extrapolating the temperature dependence of the resistance of the Pb lamellae. The resistance of the sample was measured with the transport current perpendicular to the lamellae, so the Pb resistance dominated the sample resistance. Figure 24 shows the transition temperatures determined for Pb-Cd by our work and by the thin film tunneling experiments of Toplicar (3). The two sets of data can be expected to converge according to the de Gennes-Werthamer theory (12,13) of the proximity effect. This theory studies the spatial variation of the order parameter using Gor'kov's (86) Green's function. It should be noted that the tunneling data represents a fixed Cd thickness in the thin film regime while the lamellar data represents a fixed Pb:Cd thickness ratio of 4:1 for all samples studied.

The dependence of the measured T_c of the samples on the lamellar period is shown in figure 25. The solid line shows the predictions of the de Gennes-Werthamer theory.

Our samples fall in the thick normal metal regime of this theory. It was found that this theory best fits our data when T_{cS} = 7.150K, using the experimentally determined value of 600 angstroms for the Pb mean free path. As seen in the figure, the data agrees rather well with the theory, indicating that there is qualitatively good agreement to this theory. The de Gennes-Werthamer theory assumes both metals are identical in the normal state. The results are insensitive to the properties of the normal metal and strongly dependent on the superconducting metal thickness. Our samples are only approximated by the thick normal film limit, so the changing thickness of the Cd lamellae has not been taken into account. It is probable that all of the Pb lamellae and all of the Cd lamellae are not identical. Since Pb and Cd are not very miscible, no spurious diffusion processes which will affect the transition temperature are expected at the lamellar interface.

The transition temperature theory of Deutscher and de Gennes (45) solves the Ginzburg-Landau equation (36) subject to the superconducting-normal boundary conditions. The effects of the normal metal are introduced in the boundary conditions through the extrapolation length b. The SN transition temperature turns out to be a function of the transition temperature of the superconducting material and of two adjustable parameters α' and b, where α' is

related to the Ginzburg-Landau parameter α and b represents the extent of a non-zero order parameter into the normal metal from the SN interface. In order to best fit the data to this theory, a linear regression fit was applied to d_S as a function of $(T_{cS} - T_{cNS})^{-1/2}$ for several values of T_{cS}. The best fit (figure 26) was determined by the highest correlation coefficient, which yielded fit values of $T_{cS} = 7.165K$, $\alpha' = 2.48 \times 10^{-19}\ K^{-2}$, and $b = 1.262$ microns. This value of b compares favorably with the value of b = 1.40 microns (37) obtained by the Orsay group in (SnIn)-Al thin film proximity sandwiches. The order parameter in the normal metal cannot be described by a single exponential function. Since the order parameter can be expected to extend at least 1.26 microns into the Cd from each Pb-Cd interface, the lamellar period will have to be at least 12 microns before the order parameter will become zero in the center of the Cd lamellae.

Because of the uncertainty in determining the mean free paths and coherence lengths accurately in our Pb-Cd lamellar systems, we haven't strongly quantitatively tested either the de Gennes-Werthamer theory or the Deutscher-de Gennes theory. These theories both suggest that the order parameter varies qualitatively as shown in figure 2. But the good general agreement of both these theories with our experimental results emphasizes that our observed

depression of the transition temperature is caused by true proximity effects induced by the intimate contact of the Pb and Cd.

Flux Pinning and Flux Flow in Pb-Cd

The forces which cause fluxoids to move in these composites are difficult to analyze because the spatial dependence of the currents and fields is rather complicated. In the initial flux pinning experiments for these composites, the transport current was passed parallel to the lamellae and the external field was applied perpendicular to the flat side of the sample as shown in figure 15. With this geometry, the currents in the sample will flow within a penetration depth of the surface providing the magnetic field is less than the lower critical field of the Pb and Cd. In this Meissner state the current is distributed between the Pb and Cd lamellae according to the self-inductances, L_{Pb} and L_{Cd}, and the mutual inductance, M_{Pb-Cd}. The ratio of the two currents is given by (11):

$$\frac{I_{Pb}}{I_{Cd}} = \frac{L_{Cd} - M_{Pb-Cd}}{L_{Pb} - M_{Pb-Cd}} \quad ,$$

Once flux begins to enter the specimen, it is difficult to predict the current distribution because the penetration

depth has a spatial distribution which is only partially understood (equation 33). Much more work needs to be done before a full microscopic understanding of flux patterns in inhomogeneous systems is available. Despite these difficulties, there are some very general conclusions which can be drawn from the flux flow data. According to the Silsbee criterion (87), magnetic flux first enters a type I superconducting specimen when the sum of the self and applied fields at any point on the surface exceeds the critical field of the superconductor. Huebener, Kampwirth, and Clem (88) have shown that for wide thin superconducting samples carrying current I, the applied field, H*, required to produce a field of H_c at the edge of the strip is given approximately by

$$H^* = H_c L_y/(L_x + L_y) - (0.4\ G - cm/A)\, I/(L_x + L_y) \quad , \quad (67)$$

where L_x is the width and L_y is the thickness of the specimen. It is assumed in this equation that the sample cross section can be approximated by an ellipse with major and minor axes given by the length and width of the sample. For the geometry of the samples reported here the Silsbee criterion for type I behavior of pure bulk Pb requires that the critical current density be approximately 1.3×10^4 amp/cm^2 at 4.2K when no magnetic field is applied. If the material is type II, as was the case for many samples, one

might expect flux to enter the sample and flux flow to begin at some entry field H_E which could range in value all the way from H_{c1} up to H_{c2} depending on the barriers involved. For these samples H_{c2} of the Pb regions exceeds H_c of pure bulk Pb by factors which range from 1 to 3 and the surface superconducting critical field H_{c3} might be larger by another factor of 1.7. Hence, an upper limit on the critical currents would be on the order of 7×10^4 amp/cm^2.

A second important factor affecting the flux flow is that vortices can enter the Cd regions at field H_{c1Cd} on the order of 30 Oe, which is much lower than the bulk critical field of Pb. If a transport current is applied parallel to the lamellae, a Lorentz force acts on the vortices in the Cd, tending to move them perpendicular to the lamellae. When the applied field is less than the lower critical field of Pb, the Lorentz force pulls the flux vortices in the Cd toward the Pb interface. Flux quanta are prevented from moving into the Pb because the Pb lamellae are in the Meissner state and flux entry would raise the vortex free energy. This spatial dependence of the free energy is the fundamental pinning force in the material. Because the transport current resides on the surface of the sample, the Lorentz force on a fluxoid in the Cd is mostly applied at the ends of the vortex,

distending it like a piece of spaghetti until finally it is dragged into a Pb lamella where the existence of flux is energetically unfavorable. The vortex moves rapidly through the Pb into the next Cd lamella, where it resides until a large enough force exists to drag it through the next Pb lamella. In the absence of an applied magnetic field, the Lorentz forces cause vortices to move from each edge of the sample to the center of the sample where the vortices of opposite field direction annihilate. Applying a magnetic field shifts the region of annihilation from the center of the sample toward a sample edge. Analytically, a description of this process would involve a three dimensional solution of the Ginzburg-Landau equations subject to the constraints imposed by the lamellar system. As of this writing, the solution to this dynamic situation has not been thoroughly studied. The Silsbee criterion is only a crude approximation to explain one aspect of the critical current behavior in this regime.

As the applied magnetic field exceeds the lower critical field of the Pb lamellae, vortices begin to form in the Pb and are subject to flux flow conditions. In order to move a fluxoid from the Cd to the Pb, its energy needs to be increased appropriately over some distance characteristic of the change in the magnetic field in the sample. Dobrosavljevic and de Gennes (44) calculate that

within the Cd the length of field penetration is given by equation 34 and the energy per unit length of flux is given by equation 36. Calculations show that ρ is on the order of 1000 angstroms in this theory. To estimate the critical current density of the Pb-Cd samples when the Pb lamellae are in the mixed state, the flux was considered to change energy over a length ρ. The energy per unit length of flux within the Pb may be written as

$$F_{l\ Pb} = H_{cl}\ \phi_o/4\pi \quad , \tag{68}$$

where H_{cl} for the Pb lamellae may be approximately determined from Clem's vortex core model (89) using a bulk thermodynamic critical field for the Pb lamellae of 540 gauss at 4.2K. In the Cd the energy per unit length of flux may be expressed as (44)

$$F_{l\ Cd} = H_{cl\ Cd}\ \phi_o/4\pi \tag{69}$$

where H_{clCd} has been shown experimentally by Zaitlin (4) to vary approximately between 20 gauss and 100 gauss. Balancing the Lorentz force and the pinning force due to the change in flux line energy length, the critical current may be written as

$$J_c = 0.80(H_{cl\ Pb} - H_{cl\ Cd})/\rho \tag{70a}$$

Solutions of this equation with the above values predict that the critical current density for Pb-Cd lamellar structures should approach 10^7 amps/cm^2. Equation 70, at

best, is a very rough approximation because the configuration of the vortex as it moves from the Cd to Pb regions has not been solved. The other characteristic lengths such as the penetration depths and the lamellar thickness are comparable, however, so the order of magnitude is about right.

Unfortunately, we have never been able to achieve these high critical current densities, possibly because the pinning force doesn't act over the full length of the vortex or possibly because the spatial gradient of the free energy is not well represented by these equations. One final comment is in order concerning the Pb-Cd boundary. Because the solubilities are very low at the two ends of the phase diagram, one expects much sharper boundaries at the Pb-Cd interface than previously reported for Pb-Sn. Studies of the concentration profiles in Pb-Sn eutectic lamellar structures by Blanchin, et al. (90) show that the concentration of Sn dissolved in Pb lamellae increases from a low concentration at the Pb-Sn interface to the maximum amount of solute at the center of the Pb lamellae. This concentration gradient undoubtedly causes the coherence length and penetration depth to be spatially dependent within the Pb-rich lamellae. No such experimental work is yet available on Pb-Cd lamellar structures from which to extract concentration gradients involved in the Pb lamellae

that would give a quantitative evaluation of the distance involved in the change of energy per unit length of flux. It should be noted that the Sn in the Pb-rich phase of the Pb-Sn eutectic system does not form precipitates within the Pb-rich phase of the Pb-Sn eutectic system upon annealing as Cd does in the Pb-rich phase of the Pb-Cd system. Instead, Sn diffuses out of the Pb-rich phase into the Sn-rich phase.

Experimental results for the critical current measurements with J_T parallel to the lamellae are shown in figure 27 for an unannealed sample and in figure 28 for an annealed sample. There is a supercurrent up to a critical depinning current density, J_c, and above this current density flux flow behavior is seen to dominate the V vs. I behavior. J_c here is defined to be the current density at which the first detectable (5 microvolt for this apparatus or 2×10^{-11} volts in the SQUID apparatus) voltage appeared. The normal state ohmic character does not appear until the upper critical field, H_{c2}, is reached. Typically, H_{c2} is 1.4 KOe for samples which have been annealed at room temperature for a few hours while the cryostat was being assembled. If the sample was annealed further at room temperature for two weeks, the values of J_c and H_{c2} dropped but the general character of the I vs. V curves remained the same. After the samples were annealed, a voltage free

supercurrent region was observed and flux flow was still an important factor as shown on figure 28. For the 2.53 micron sample and the 3.00 micron sample, the upper critical field was observed to drop rapidly and approach the thermodynamic critical field of bulk Pb after annealing. For the 1.46 micron sample H_{c2} dropped much less. Values of J_c dropped by about 25% for all three samples indicating that J_c is not closely linked to H_{c2} but to other properties of the sample. The characteristic parameters d, d_S, d_N, L, W, Z, J_c, J_S, and H^*_{c2} for all the samples are given in Table 1.

For all the samples measured here, the flux flow critical current, J_c, values are 3 to 5 times larger than the Silsbee flux entry critical current J_S. This simply means that the flux which enters the sample above J_S does not flow across the sample but is pinned part way across. If the Bean critical state model (91) is used to describe the profile of flux across the sample with the critical state current density, J_{cS}, independent of field, then one expects the flux front to be linear in position with a slope

$$\frac{\Delta B}{\Delta x} = \frac{4\pi}{c} J_{cS}. \qquad (70b)$$

With increasing transport current, the flux will first enter the edge of the specimen at J_S and the linear flux

Table 1. Summary of critical current data

sample	CRS-29	CRS-28	CRS-26	CRS-27	CRS-30	CRS-33	CRS-34
d(μ)	0.65	0.985	1.46	2.53	3.00	inf.	inf.
d_{Pb}(μ)	0.51	0.772	1.14	1.98	2.35	inf.	inf.
d_{Cd}(μ)	0.14	0.213	0.32	0.55	0.65	0.0	0.0
L(cm)	3.82	3.62	2.89	4.24	3.42	3.80	3.69
W(mm)	1.06	1.39	1.49	1.63	1.42	1.39	0.83
Z(mm)	0.016	0.028	0.040	0.030	0.043	0.043	0.043
J_S(10^4 A/cm²)	1.27	0.97	0.91	0.83	0.95	0.97	1.63
Measurements made at 4.2K							
anneal			No	No	No		
R_{Pb-Cd} (mΩ)			1.42	2.29	2.06		
ρ_{Pb-Cd} (μΩ-cm)			0.287	0.256	0.370		
J_c(10^4 A/cm²)			6.0	7.12	6.93		
H^*_{c2} (KOe)			1.34	1.46	1.44		
J_c/H^*_{c2}			44.8	48.8	48.1		
anneal	2 wks.	2 wks.	2 wks.	2 wks.	2 wks.	2 wks.	2 wks.
R_{Pb-Cd} (mΩ)	14.91	4.24	0.88	1.73	1.24	0.040	0.072
ρ_{Pb-Cd} (μΩ-cm)	0.67	0.45	0.18	0.19	0.22	0.0063	0.0070
J_c(10^4 A/cm²)	5.86	8.88	5.13	6.33	5.38	3.99	4.18
H^*_{c1} (KOe)	0.78	0.72	1.20	0.60	0.66	0.50	0.50
J_c/H^*_{c2}	75.1	123.3	42.8	105.5	81.5	79.8	83.6

front will progress across the sample. When the flux front reaches the center of the sample at a transport current, J_c, the driving force exceeds the pinning force at every point across the sample. The vortices will move to the center where they annihilate and a finite voltage will appear. It is important to note that a critical state model gives a J_{cS} which depends on the width of the sample. Typical values for critical state current densities to give the observed J_c are on the order of $3x10^4$ amp/cm^2.

In order to gain some insight about the factors which control the flux flow, the critical currents have been measured as a function of lamellar spacing, applied magnetic field, temperature, and electron mean free path in the Pb region. As shown on figure 29, J_c is essentially independent of lamellar spacing. The 0.985 micron repeat distance sample appears to have an anomalously high J_c of $8.88x10^4$ amp/cm^2 but the others all cluster around $6x10^4$ amp/cm^2. For these currents the self field is comparable to H_c and the vortex spacing is much smaller than the lamellar width. Hence, one would not expect any of the flux matching enhancement such as seen by Martinoli, et al. (92). To see matching effect it would be necessary to have fields on the order of 30 gauss or less.

The magnetic field dependence shown on figures 30 and 31 indicates that J_c is suppressed to zero at fields

comparable to the bulk critical field, but not numerically equal to it. The temperature dependence of J_c, shown on figures 32 and 33 follows a $1-t^2$ behavior similar to the temperature dependence of H_c. Figure 34 shows the temperature dependence of H^*_{c2} and how H^*_{c2} was experimentally determined. The apparent correspondence between J_c and H_c is to be contrasted with the connection between J_c and H_{c2}. The ratio of J_c/H^*_{c2} shown on Table 1 varies by large factors from sample to sample and, indeed, upon annealing the 2.53 micron sample and the 3.00 micron sample show factors of two changes in H_{c2} but only a 25% change in J_c. Hence, it would appear that the critical state currents and, hence, J_c are governed by basic free energy considerations related to H_c as a major factor and the connection to mean free path and H_{c2} is relatively less important. It is well to remember, however, that annealing did consistently lower J_c by 25%, so that either the mean free path or the formation of small Cd precipitates in the Pb lamellae must be important factors.

Proximity Effects in Pb-Cd

Directionally solidified Pb-Cd eutectic lamellar structures provide an especially attractive system in which to study the proximity effect because the contact between the two metals is unusually regular and clean. This system

then gives a set of about 5000 superconducting-normal-superconducting (SNS) junctions in series if the current is passed perpendicular to the boundaries as shown in figure 17. Figure 35 shows the temperature dependence of the sample resistance for a typical specimen measured with SQUID detection. At the transition temperature, the Pb undergoes a very sharp superconducting transition. During the Pb transition, the sample resistivity typically is lowered by 90% within a 10 to 20 mK temperature interval. A tailing at the lower end of the resistance vs. T curve is seen to extend approximately 100 mK below the sharp Pb transition. This is the decreasing resistance of the Cd lamellae as they are induced into an increasingly superconductive state by the superconducting Pb lamellae. The strength of the proximity effect is emphasized by the fact that the Cd, with a bulk transition temperature of 0.5 K, is superconductive at 7K in a proximity sandwich in no applied magnetic field. For this sample the resistance of the Cd layers, if they were completely normal, would be 0.005 mΩ and this is just the resistance at which the R vs. T curve breaks to a different behavior, the so-called tail region. We, therefore, believe this tail region is a manifestation of the onset of superconductivity in the Cd lamellae. Figure 35 also shows R vs. T for two applied fields. For small fields, the

critical field curve of Pb is approximated by

$$t = 1 - (\tfrac{1}{2})\{H_c(t)/H_c(0)\} \quad . \tag{71}$$

As the field is increased, the transition temperature is lowered according to the critical field curve of Pb and the R vs. T curve is linearly shifted to lower temperatures. It is important to note the resistance in the Cd regions obeys the same critical field curve as the Pb so the data confirm that the pair potential in the Cd is governed by the Pb pair potential. Figure 36 shows R vs. H for several temperatures. For t close to 1, the critical field equation reduces to

$$H_c(t) = 2H_c(0)\{1 - t\} \quad . \tag{72}$$

The magnetic field transition in Pb-Cd is seen to shift linearly as the temperature is changed.

From the normal state resistivity can be reaped a great deal of information about the superconducting properties of a material. According to Chambers (93) the resistivity and mean free path in a metal are closely related. Equations for Pb and Cd may be written:

$$\text{Pb:} \quad \rho l = 1.06 \times 10^{-11} \text{ ohm-cm}^2 \quad , \tag{73}$$

$$\text{Cd:} \quad \rho l = 1.75 \times 10^{-11} \text{ ohm-cm}^2 \quad . \tag{74}$$

Measuring resistivity values parallel and perpendicular to the lamellae allows the extraction of resistivity values for Pb and Cd. Chambers' equations yield effective mean free paths corresponding to these resistivities. Equation

32 relates the Pb mean free path to the Pb penetration depth. A reasonable first order approximation to the coherence length in Pb is given by de Gennes (39):

$$\xi(T) = \phi_o/[2\sqrt{2}\ \pi\lambda(T)H_c(T)] \quad , \tag{75}$$

where the critical field of bulk Pb can be used as a reasonable value for the critical field of the Pb lamellae. The characteristics of the samples measured are listed in Table 2.

For the samples measured, the Cd resistivity was treated as a constant, independent of annealing because the mean free path already was much greater than the Cd thickness. Using the Chambers' relation for Cd, the mean free path in Cd is shown to be 3.13×10^4 angstroms. Because this mean free path is much larger than ξ or λ, the Cd lamellae can easily be considered in the clean limit. Equating $\xi(T)$ and $K_N^{-1}(T)$, equation 75 was applied to the Cd lamellae in the Pb-Cd samples to find the coherence length. An expression for the spatial and temperature dependence of the penetration depth was derived in equation 33. In the range of typical values for $\xi_S(T)$ and for b = 1.262 microns, it was found that A is particularly insensitive to changes in $\xi_S(T)$ and has a value of 0.894. Experimental values of NV for Pb and Cd are (39) 0.39 and 0.18 respectively. The best calculated value of the London penetration depth at T = 0 for Cd is 1110 angstroms

Table 2. Summary of proximity effect samples

sample	CRS-12	CRS-11	CRS-10	CRS-15	CRS-13	CRS-31	CRS-32
d(μ)	0.947	1.45	2.05	2.89	3.11	9.07	9.07
d_{Pb} (μ)	0.742	1.14	1.61	2.27	2.44	7.11	7.11
d_{Cd} (μ)	0.205	0.31	0.44	0.62	0.67	1.96	1.96
L(cm)	1.02	0.78	0.73	1.05	1.05	0.49	0.66
W(mm)	1.51	1.67	1.39	1.45	1.26	0.88	0.24
Z(mm)	0.082	0.123	0.122	0.059	0.147	0.129	0.129
detector	K-5	K-5	K-5	K-5	K-5	SQUID	SQUID
anneal	no	no	no	no	no	2 wks.	2 mo.
T_c (K)	7.075	7.108	7.132	7.137	7.138	7.150	7.149
ρ_{Pb} (μΩ-cm,8K)	1.79	2.07	1.76	2.68	2.24	0.59	0.33
ρ_{Cd} (μΩ-cm,8K)	0.056	0.056	0.056	0.056	0.056	0.056	0.056
l_{Pb} (A,8K)	593	513	602	395	474	1785	3202
l_{Cd} (10^4A,8K)	3.125	3.125	3.125	3.125	3.125	3.125	3.125
λ_{Pb} (A,0.0K)	813	849	810	922	870	636	589
ξ_{Pb} (A,0.0K)	355	340	356	313	332	454	491
ξ_{Cd} (A,7.0K)	1378	1378	1378	1378	1378	1378	1378
ξ_{Cd} (A,4.2K)	2297	2297	2297	2297	2297	2297	2297
κ_{Pb} (7.0K)	1.35	1.47	1.34	1.73	1.54	0.72	0.61
κ_{Pb} (4.2K)	1.77	1.93	1.76	2.28	2.02	1.08	0.93

(94,95). Combining these values yields an equation for the penetration depth in the Cd lamellae as a function of temperature and distance from the NS boundary:

$$\lambda_{Cd}(x,T) = \frac{3596 \text{ (angstroms)}}{\sqrt{1 - t^4}} \frac{\cosh K_N d_N/2}{\cosh K_N X} \quad . \qquad (76)$$

The predicted spatial dependence of the penetration depth for the Cd lamellae is shown in figure 37 for several temperatures.

To further characterize the Pb-Cd eutectic lamellar system, the current-voltage (I-V) characteristics were studied with the transport current passing perpendicular to the lamellae. Using a Leeds & Northrup K-5 potentiometer and a Guildline galvanometer amplifier, the family of I-V characteristics in figure 38 was obtained. On these curves, the resistivity of the Cd is too small to be detected with this system so the behavior shown here is controlled by the Pb regions. These curves are characteristic of all the samples studied with this sensitivity of detection. Critical currents may be defined from these curves as the current at which the first non-zero voltage appears. At some value of current below the critical current, self-field effects induce the formation of vortices in the Pb lamellae. These vortices are pinned on defects in the Pb lamellae until the Lorentz forces exceed the pinning forces and the vortices from

either side of the sample flow within the Pb lamellae and finally annihilate at the center. An applied field tends to move the annihilation point from the center of the sample toward one edge. As the field increases, the sample approaches a critical state and abruptly undergoes the transition into the normal state.

To determine what dissipative processes can occur in the Cd lamellae, a SQUID was used to measure the I-V characteristics for the samples with very high sensitivity (10^{-11} volts). Figure 39 shows an I-V curve obtained with the SQUID on an annealed sample. These curves demonstrate flux flow within the Cd lamellae which is a direct consequence of the existence of vortices in the Cd lamellae as predicted by Dobrosavljevic and de Gennes (44). By studying the thermal conductivity of the lamellar Pb-Cd eutectic system, Zaitlin (4) has demonstrated that vortices form in the Cd lamellae in Pb-Cd as predicted by Dobrosavljevic and de Gennes for lamellar structures. A dip in the thermal conductivity data suggested that regions of the Cd lamellae were driven normal by a small applied magnetic field. The change in thermal conductivity indicated that much of the Cd remained superconducting and that the normal regions in the Cd were truly fluxoids. Even though vortices form within the Cd lamellae, the vortices are pinned so that no voltage is generated at low

currents. Because the Cd is known to be in the clean limit, the only pinning of the vortices within the Cd is expected to be to be caused by metallurgical inhomogeneities. When flux flow begins, a small voltage is generated as shown in figure 39. As the applied magnetic field is increased, the slopes of the I-V curves increase, indicating increased flux flow in the Cd. The Cd flux flow resistance approaches the Cd normal state resistance. As the applied magnetic field approaches the critical field of Pb, the resistance of the sample rapidly increases beyond the normal state resistance of the Cd, indicating that flux flow is beginning to occur within the Pb lamellae. The I-V curves then assume the character previously shown in figure 38.

A study of the magnetic field dependence of the critical current was undertaken to see if any interference associated with Josephson tunneling (5) behavior could be detected similar to the results reported for Pb-Sn. No such interference was found. An important parameter in this search is the Josephson penetration depth which is given by:

$$\lambda_J = \{\hbar c^2/[8\pi j_J e(d_N+2\lambda_B)]\}^{\frac{1}{2}}, \qquad (77)$$

where $e=4.8\times10^{-10}$ statcoulomb and j_J is the Josephson supercurrent. For these junctions, j_J is greater than 1 amp/cm^2. Using $d_N=2$ microns and $\lambda_B=0.5$ micron, it is found

that λ_J<0.1 mm for these samples. Hence, the data were taken in the large junction regime where multiple vortex modes are expected to occur. Aslamazov and Larkin (96) predict that in a wide superconducting bridge (of which we have approximately 1000 in series) the critical current for the bridge is determined when the current density at the edge of the bridge reaches its Josephson critical value. They also predict that the bridge characteristics are strongly geometry dependent, but these bridges have a rather simple rectangular geometry. Previous studies of Josephson effects in Pb-Sn eutectic lamellar structures (76) report the possible existence of Josephson tunneling in a series array of approximately 100 Pb-Sn junctions.

The results of an I_c vs. H study for Pb-Cd are plotted in figure 40. For applied magnetic fields up to 36 gauss parallel the junctions, no striking Fraunhofer-type diffraction effects were noticed in our samples. The shape of this curve is symmetric with field reversal. Owen and Scalapino (97) solved the Josephson equation subject to boundary conditions and found that the solution involved Jacobian elliptic functions. Figure 41 shows the results of their calculations for Z = 10 λ_J. Solymar (98) noted that the simultaneous existence of several vortex modes disguises the interference nature of each individual mode of the junction. The envelope representing the maximum

current of the simultaneous vortex modes shows maxima which only represent 10% to 15% changes in critical currents. This small expected amplitude of the interference pattern is complicated by the fact that we are studying approximately 1000 junctions, all of which surely have slightly different Josephson critical currents. Both of these effects tend to make the detection of existing Josephson effects nearly impossible. Indeed, if the Owen-Scalapino result applies, it is doubtful that the previous Pb-Sn results should be believed.

In order to possibly detect only Josephson effects due to the first vortex mode, the critical current was measured with field increments of 0.05 gauss. The results are shown in figure 42. Within limits of the scatter of the data, no interference effects are seen, indicating that no Josephson effects are detectable in this experiment. Notarys and Mercereau (99) have shown that Josephson effects rapidly disappear as the area of the junction exceeds $\phi_o/B_c(T)$. Because the metallurgical process involved demands that our junctions be at least 25 microns thick, this criteria requires a sample width of less than 1000 angstroms for significant Josephson phenomena to appear. These interference effects were not seen and, indeed, theory predicts that they should not be seen.

Even though the Pb-Cd system has provided a good system in which to study the proximity effect, it was somewhat disappointing to discover that the pair potential was so large throughout each entire Cd lamella. Recent reports by Lechevet, Neighbor, and Shiffman (100,101) on the specific heat of Pb-Sn showed that there are two superconducting-normal transitions: one at approximately 7.2K (Pb-rich phase) and one at approximately 4K (Sn-rich phase). This indicates that the Sn lamellae are never entirely induced into a superconducting state for reasonable lamellar periods (0.5 microns < d < 6 microns). However, specific heat measurements on Pb-Cd by Bevolo, et al. (57) indicated no such behavior in the Pb-Cd lamellar system. These specific heat experiments indicated only a single superconducting-normal transition at approximately 7.2K (Pb-rich phase) which depended on the lamellar period of the specimen. These measurements in conjunction with the thermal conductivity data of Zaitlin (4) and the resistive data of this dissertation indicate that each Cd lamella becomes very strongly superconducting within approximately 0.15K of the sharp Pb-phase transition temperature.

SUMMARY

Lamellar Pb-Cd eutectic composites provide a unique system in which to study superconductivity in inhomogeneous materials. In this work we have developed techniques for preparing samples with a nearly perfect lamellar structure over dimensions of 1 cm x 10 cm x 0.005 cm. These aligned lamellar structures offer a large number (on the order of 1000) of well-defined normal-superconductor interfaces in which to study flux pinning, flux flow, and the proximity effect. It has been demonstrated that the Cd lamellae are in the clean normal metal limit with mean free paths much longer than the Cd thickness. Attempts to grow samples with a shorter mean free path in the normal metal were only partially successful. The ternary Pb-Mg-Cd lamellar structures grew satisfactorily but the scattering cross section of the Mg dissolved in the Cd was not large enough to bring the Cd lamellae to the dirty limit.

The basic quantities which control the properties of the composites have been measured. Resistive measurements with the current parallel the lamellae allowed us to measure H_{c2} and J_c in these structures. Passing the transport current perpendicular the lamellae allowed us to determine T_c, ρ_S, ρ_N, l_S, l_N, ξ_S, ξ_N, $\lambda_N(x)$, and λ_S. By measuring T_{CNS} vs. d_S for our samples, we were able to extract a very reasonable bulk value of $T_{cS}=7.165K$ for the

Pb lamellae of our samples using the Deutscher-de Gennes theory. This theory also predicts an extrapolation length, b, for our system of 1.26 microns. This value of b determines the spatial extent over which the superconductivity of Pb is affected by the Cd. These results, combined with Zaitlin's thermal conductivity data, give us a fairly clear picture of how $\Delta(x)$ behaves in the Cd lamellae as shown in figure 2.

Flux flow data obtained by applying a transport current parallel the lamellae indicated that a critical state model was appropriate to describe entry of flux into the sample. Flux first enters the specimen at a current determined by the demagnetizing factor and the Silsbee criterion. As the current increases further the flux front moves toward the center at a rate determined by the critical state shielding current, J_{cS}. These samples typically show this J_{cS} to be 3×10^4 amp/cm^2. When the flux front reaches the center of the sample the vortices annihilate and flux flow begins. The I-V characteristics indicated typical flux flow behavior up to applied fields of H_{c2}, where the sample became totally normal.

Resistive measurements made with the transport current perpendicular to the lamellae showed that there were large Josephson supercurrents through the Cd lamellae. This verifies that a strong pair potential is induced throughout

the Cd lamellae by the Pb lamellae. The behavior of the Josephson current in an applied magnetic field can be qualitatively explained by the Owen-Scalapino solutions to the Josephson equation which show for large Josephson junctions several vortex modes with different critical currents are allowed to exist.

R vs. T measurements indicated a very sharp Pb transition followed by a tail which seems to indicate that the pair potential is still zero in the center of the Cd lamellae. A tail in the R vs. H data seems to indicate that Δ_{Cd} does not undergo a first order phase transition as a function of field, but Δ_{Cd} approaches zero smoothly as Δ_{Pb} goes to zero. If there had been a first order transition in the Cd region of our samples as a function of magnetic field, an abrupt step would have been apparent in the shape of the tail. None was observed. The critical field curve of the Cd regions is very nearly the same as the Pb regions and seems to be completely controlled by the value of the pair potential in the bulk Pb. Analysis of the flux flow data for current perpendicular to the lamellae indicates that J_c is proportional to H_c with the same proportionality constant as for the current parallel to the lamellae. The measurements then demonstrate that the pinning of vortices at the planar Pb-Cd interface is not an important factor limiting flux flow. The critical

current densities are independent of lamellar spacing and independent of whether vortices are driven parallel or perpendicular to the Pb-Cd interfaces.

Figure 1. Typical I-V characteristics for flat type II superconductor with a transport current and magnetic field applied as shown

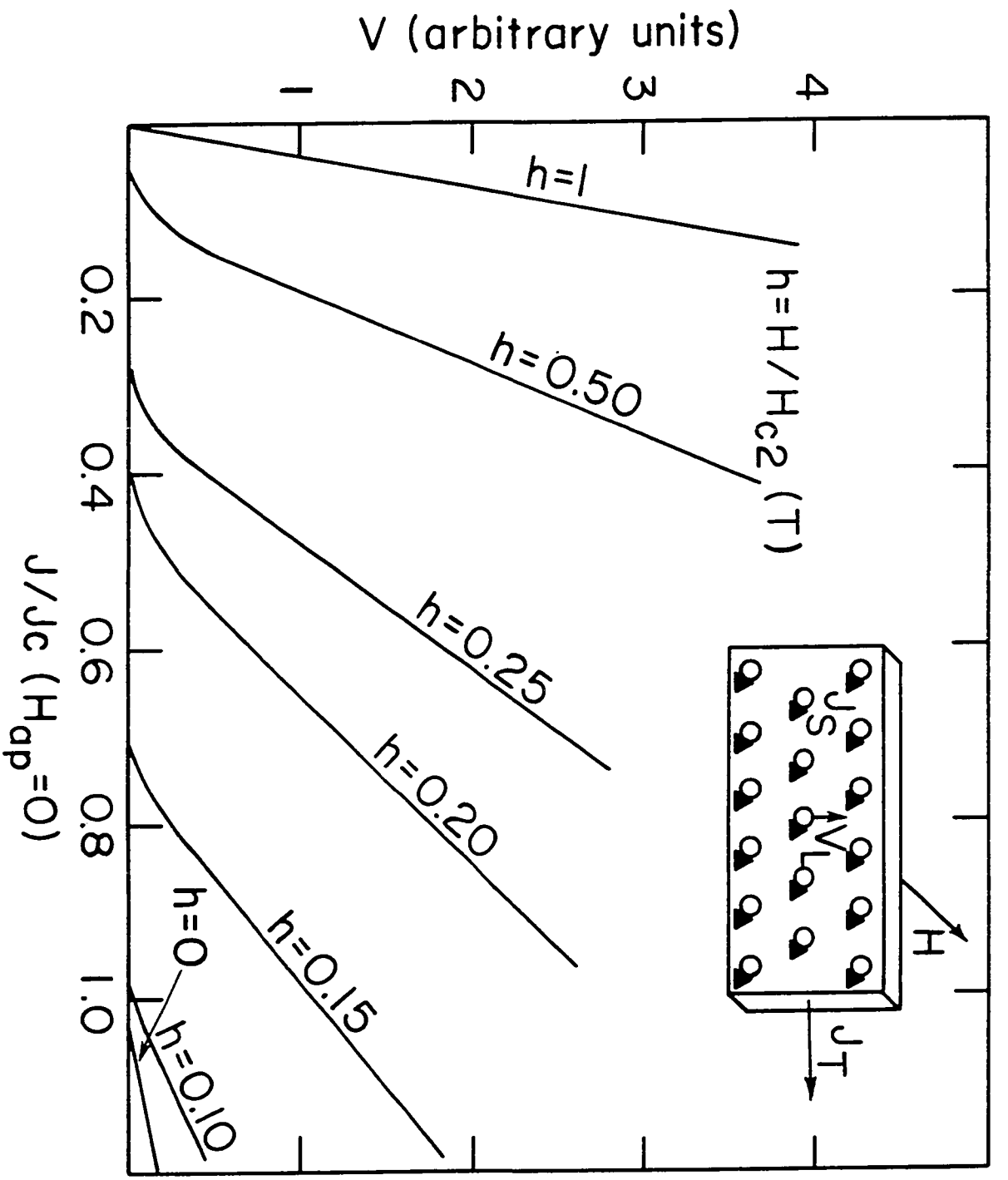
V (arbitrary units)
1
2
3
4
h=1
h=0.50
h=0.25
h=0.20
h=0.15
h=0.10
h=0
h=H/Hc2 (T)
J/Jc (Hap=0)
0.2
0.4
0.6
0.8
1.0
JS
VL
H
JT

Figure 2. Predicted variation of the pair potential as a function of distance from the center of the Cd lamella determined from solutions of the Ginzburg-Landau equation. Zaitlin (4) found that $\Delta_{Pb}/\Delta_{Cd} = 0.4$ at the interface for Pb-Cd eutectic lamellar structures. (_._._) indicates Zaitlin's experimental results; solid lines show predicted cosh dependence

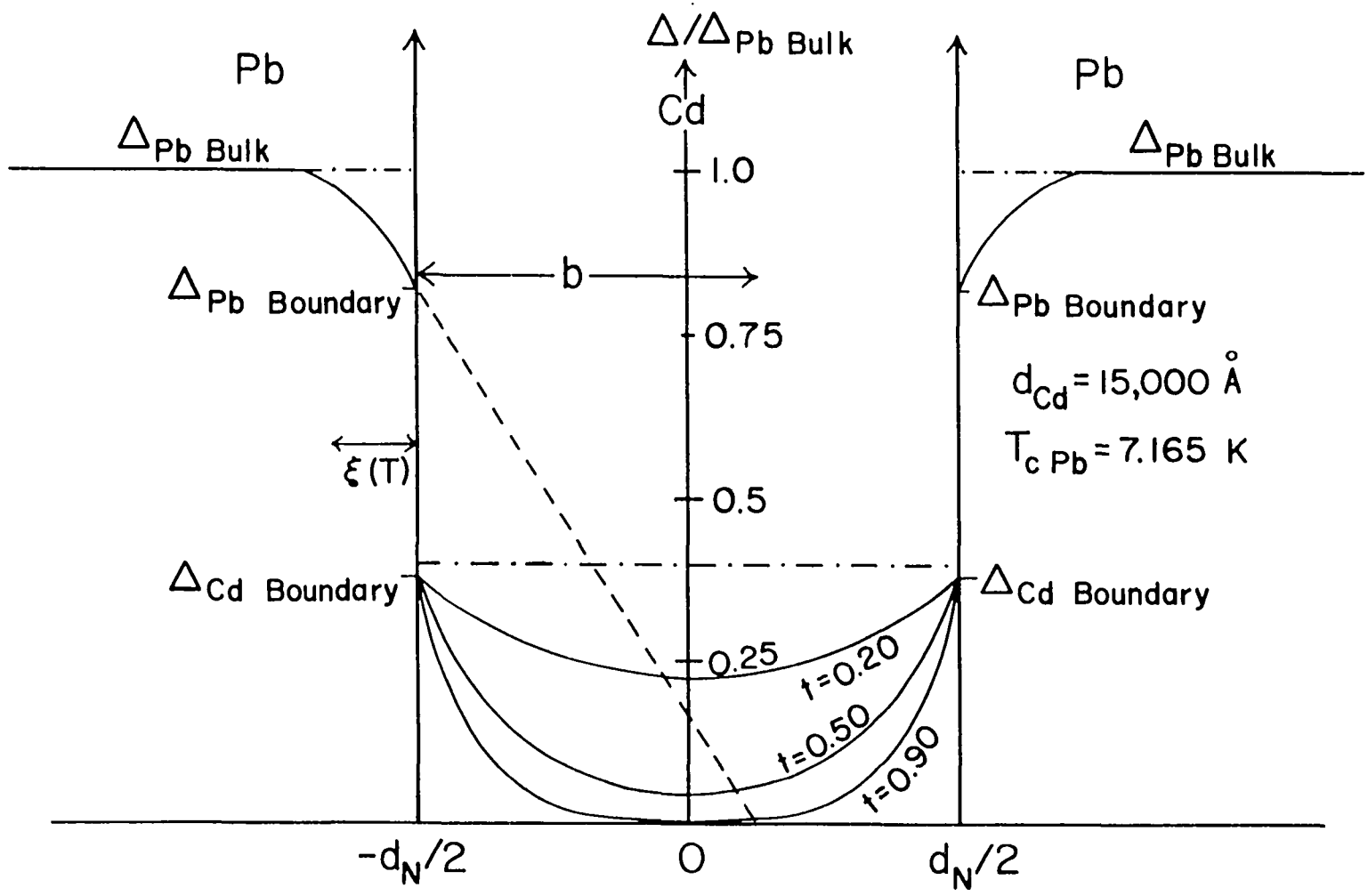
Pb
Δ Pb Bulk
Δ Pb Boundary
ξ(T)
Δ Cd Boundary
Δ/Δ Pb Bulk
Cd
1.0
b
0.75
0.5
0.25
t=0.20
t=0.50
t=0.90
-d_N/2
0
d_N/2
Pb
Δ Pb Bulk
Δ Pb Boundary
Δ Cd Boundary
d_Cd = 15,000 Å
T_c Pb = 7.165 K

Figure 3. Model of Dobrosavljevic and de Gennes: a) dimensions of vortex formed in N lamella, b) magnetic field profile in N lamella

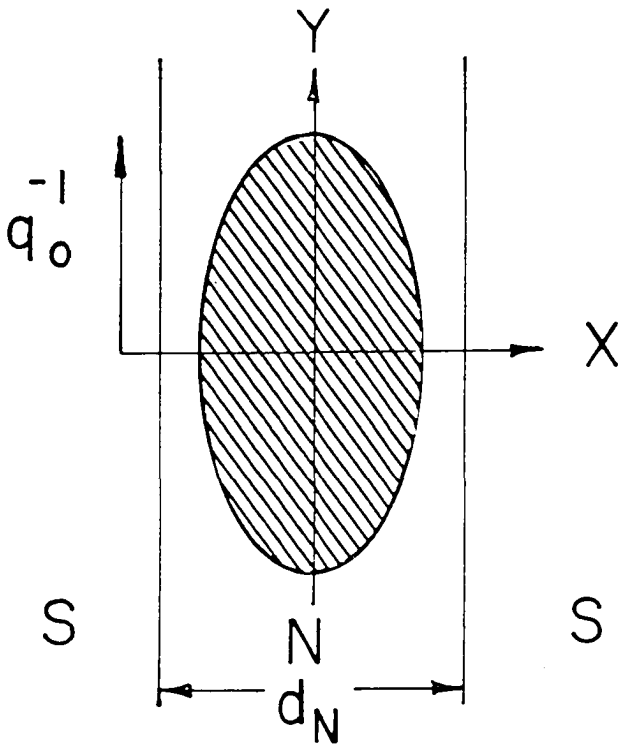

a.

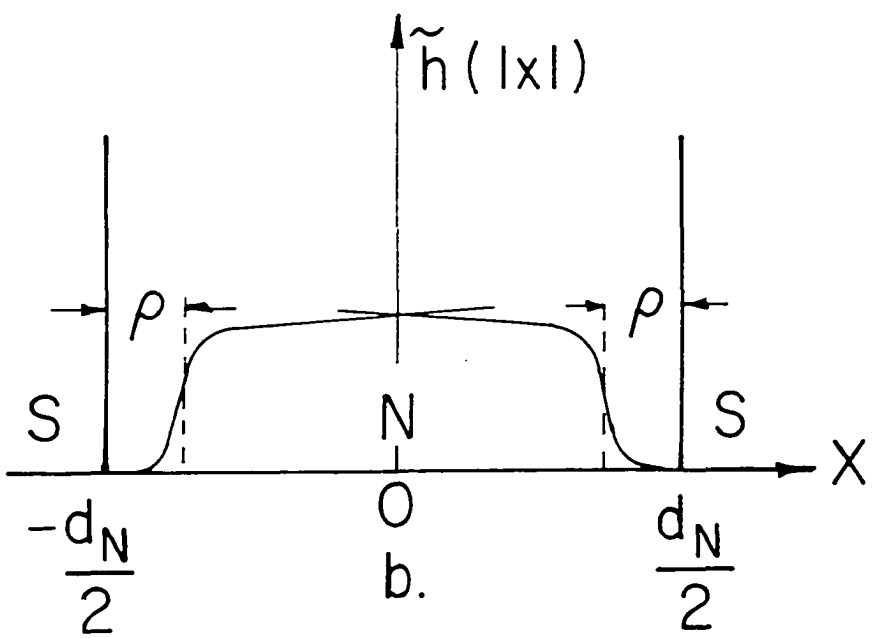

b.

Figure 4. Steady state growth of lamellar eutectic

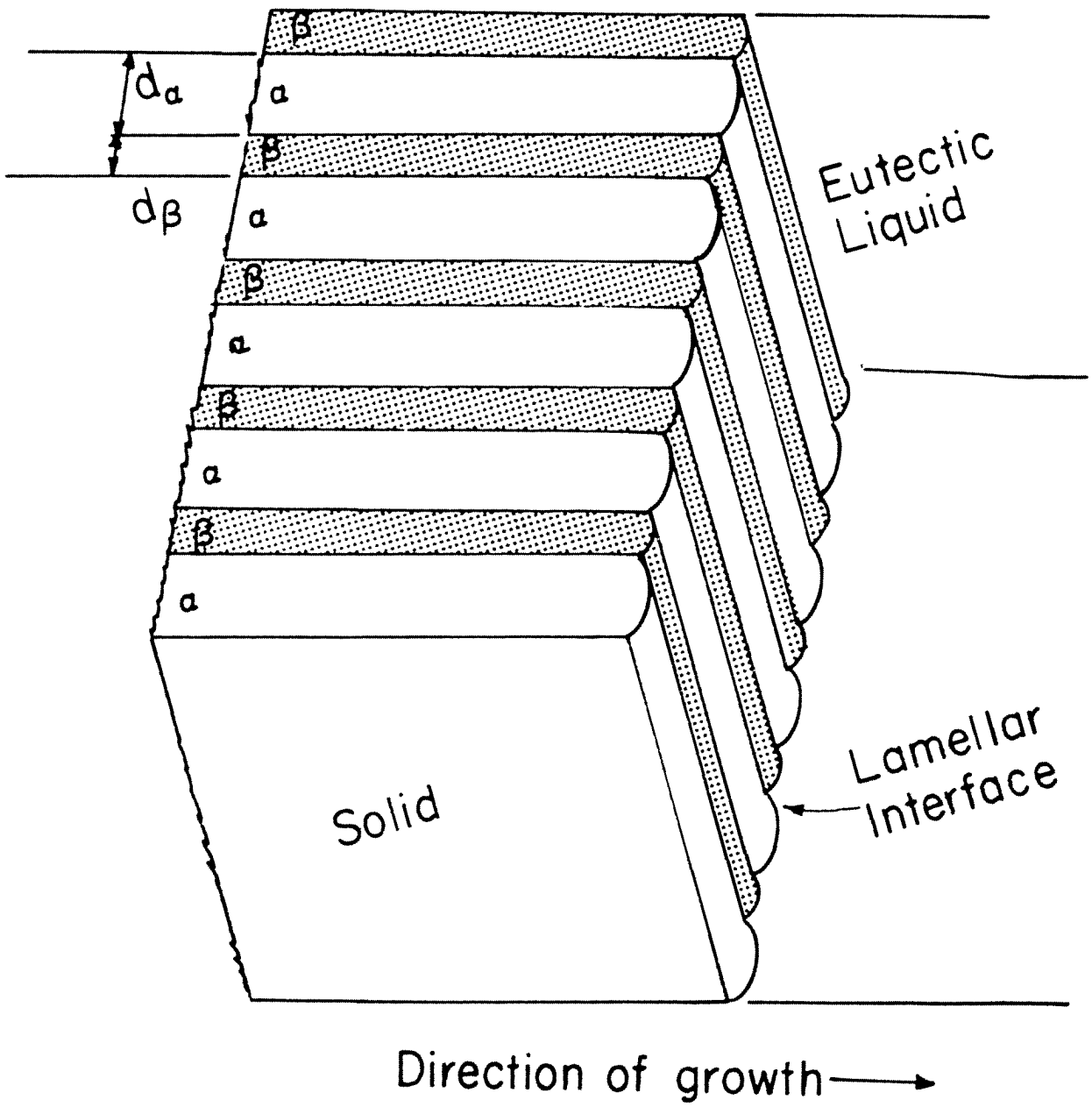
β
d_α
α
β
d_β
α
β
α
β
α
β
α
Eutectic
Liquid
Solid
Lamellar
Interface
Direction of growth

Figure 5. Isotherms in vicinity of solid-liquid interface during lamellar growth (53)

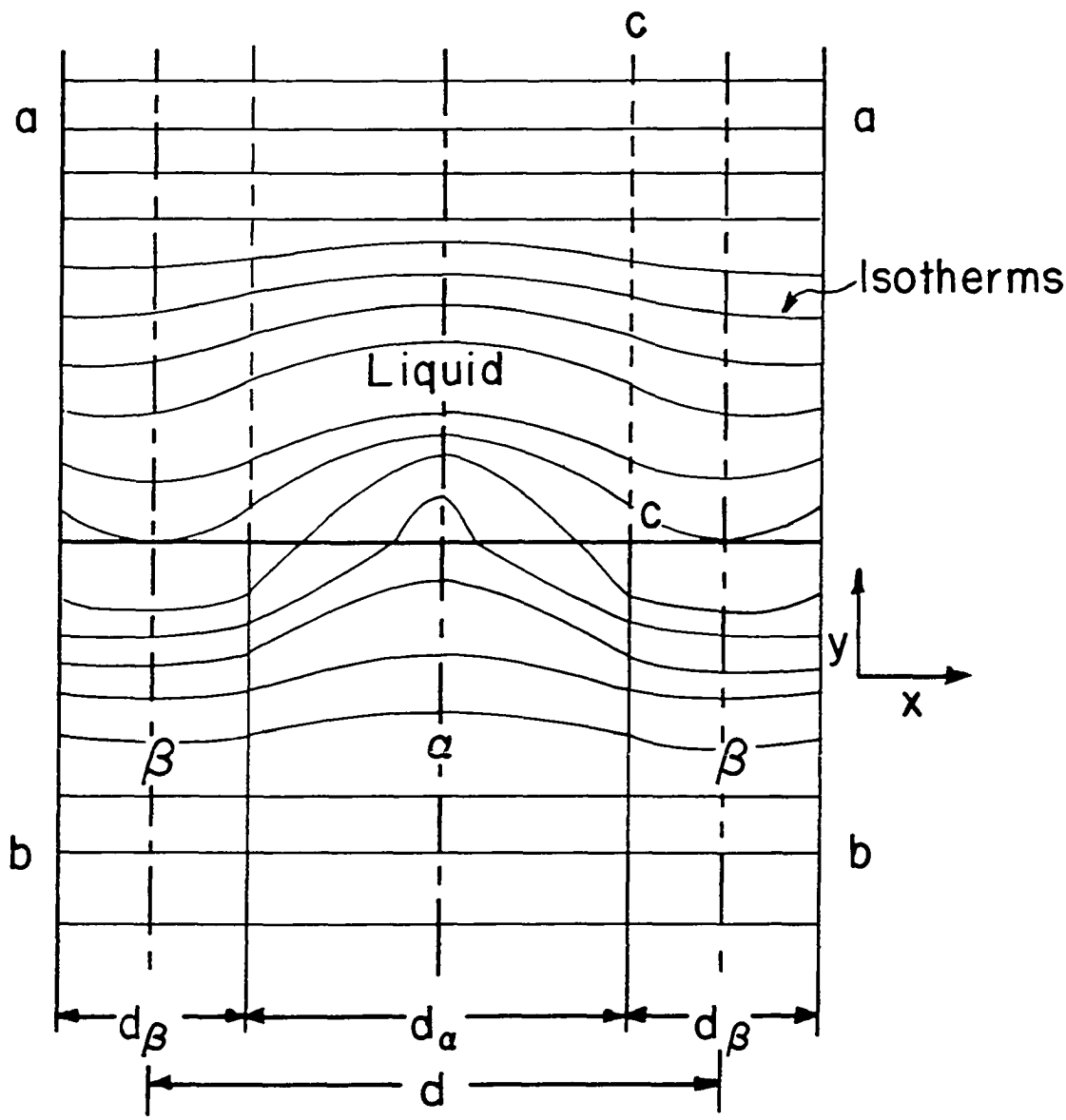
c
a
a
Isotherms
Liquid
c
y
x
β
α
β
b
b
d_β
d_α
d_β
d

Figure 6. Extrapolation of liquidus to the supercooled interface temperature (54)

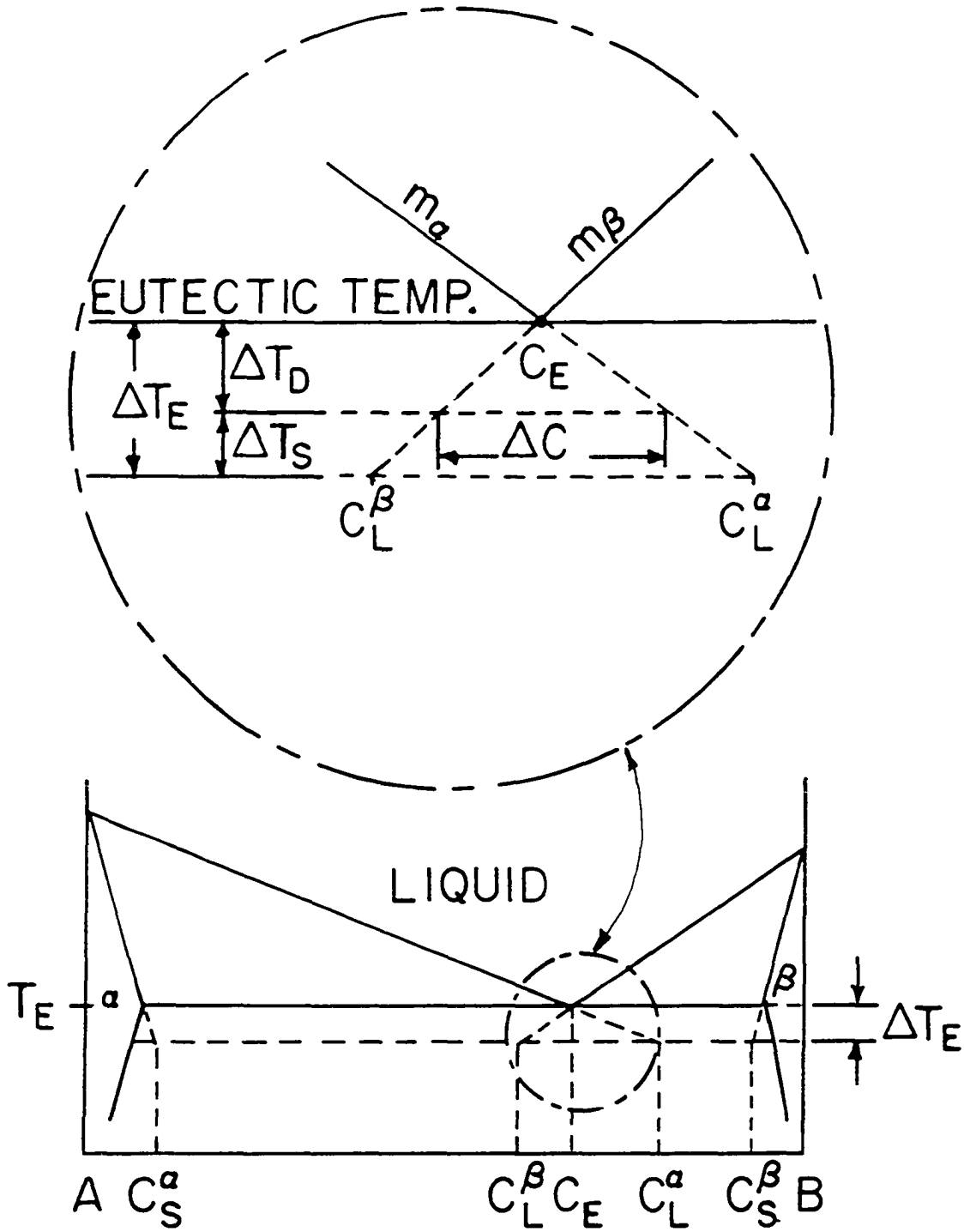
m_α
m_β
EUTECTIC TEMP.
ΔT_D
ΔT_E
ΔT_S
C_E
ΔC
C_L^β
C_L^α
LIQUID
T_E
α
β
ΔT_E
A C_S^α
C_L^β C_E C_L^α C_S^β B

Figure 7. Most probable interface shape during steady-state growth of lamellar eutectic

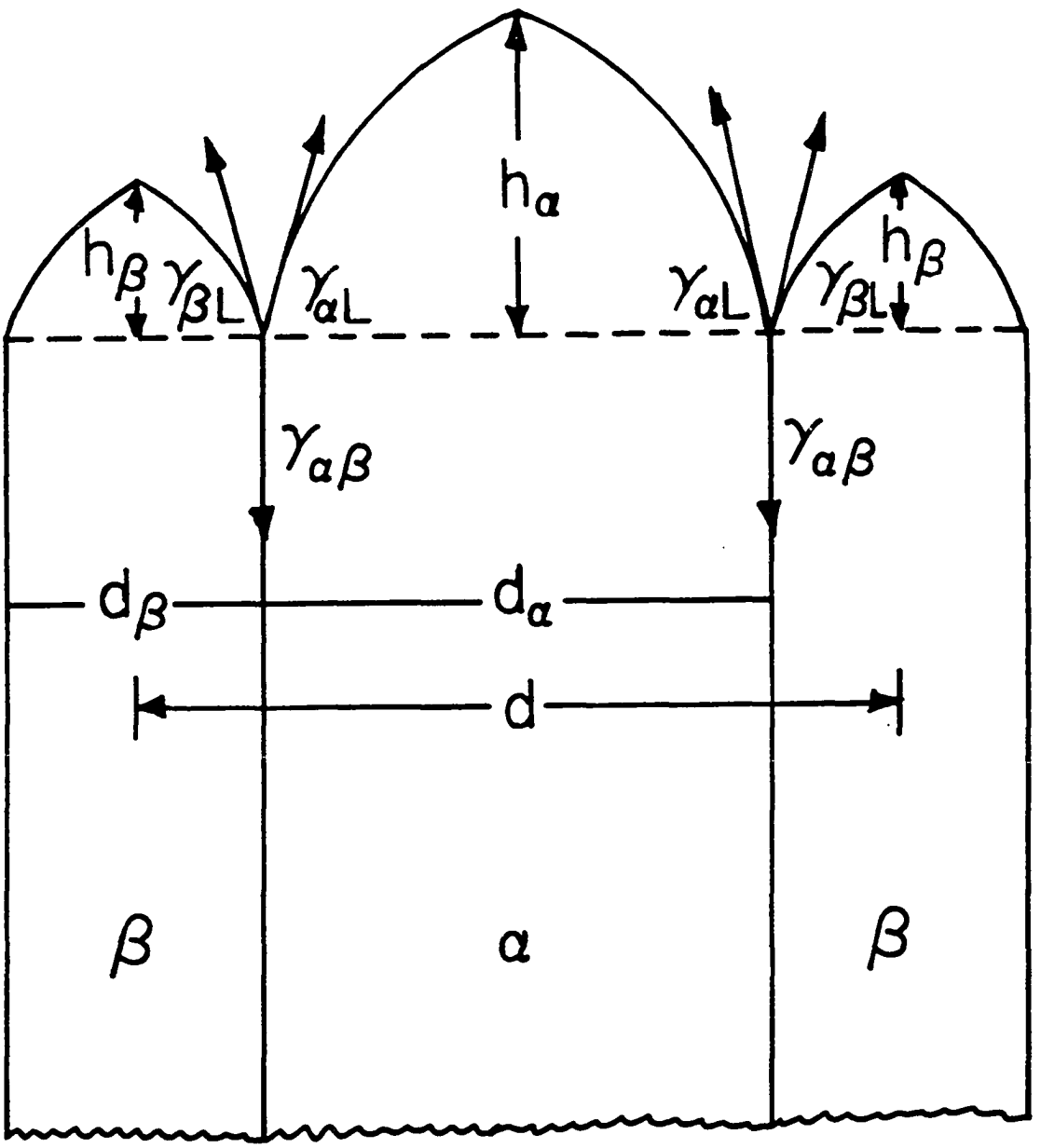
h_α
h_β
$\gamma_{\beta L}$
$\gamma_{\alpha L}$
$\gamma_{\alpha L}$
$\gamma_{\beta L}$
h_β
$\gamma_{\alpha\beta}$
$\gamma_{\alpha\beta}$
d_β
d_α
d
β
α
β

Figure 8. Diffusion paths required to produce solute redistribution and concentration profiles along the centerlines of the α and β lamellae (54)

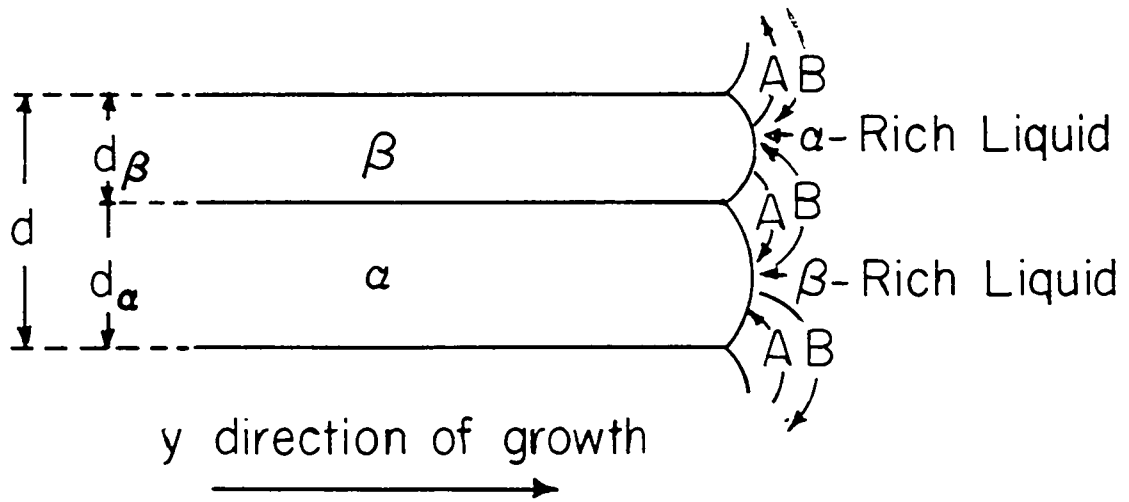
A B
α- Rich Liquid
A B
β- Rich Liquid
A B
d_β
d_α
d
β
α
y direction of growth

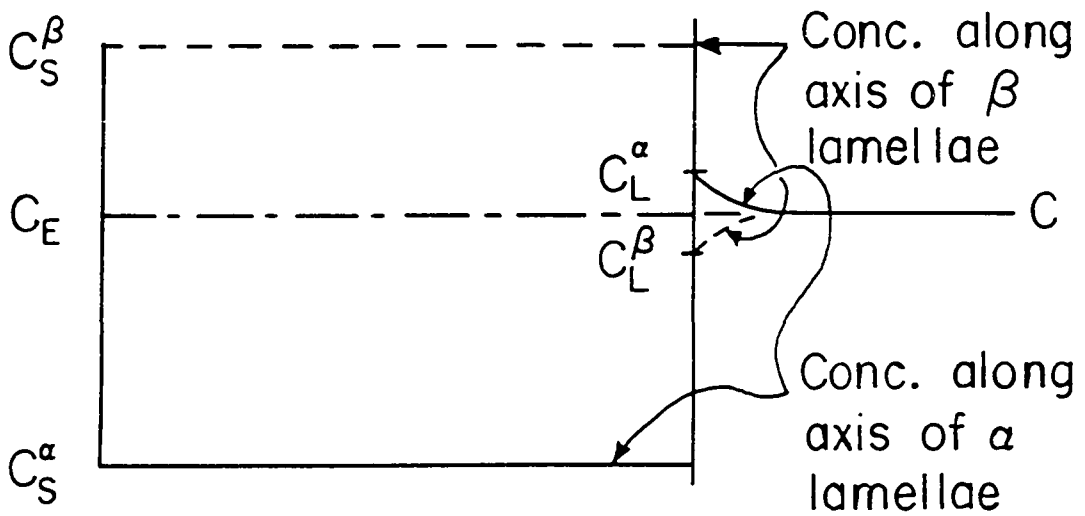
C_S^β
C_E
C_S^α
C_L^α
C_L^β
C
Conc. along axis of β lamellae
Conc. along axis of α lamellae

Figure 9. Plot of relation of lamellar spacing and directional solidification speed for Pb-Cd eutectic alloys

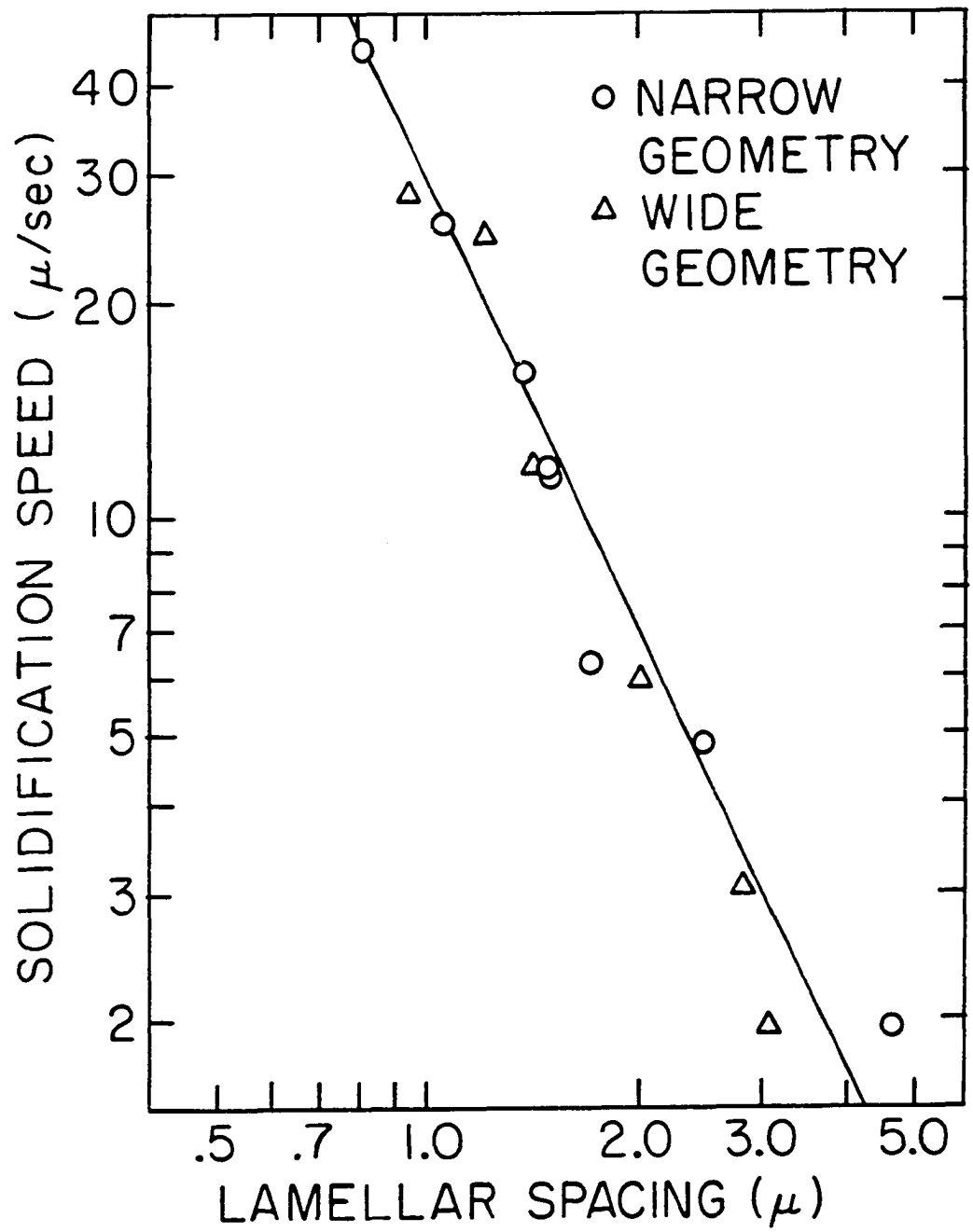
SOLIDIFICATION SPEED (μ/sec)
40
30
20
10
7
5
3
2
NARROW GEOMETRY
WIDE GEOMETRY
.5
.7
1.0
2.0
3.0
5.0
LAMELLAR SPACING (μ)

Figure 10. Pb-Cd phase diagram (58)

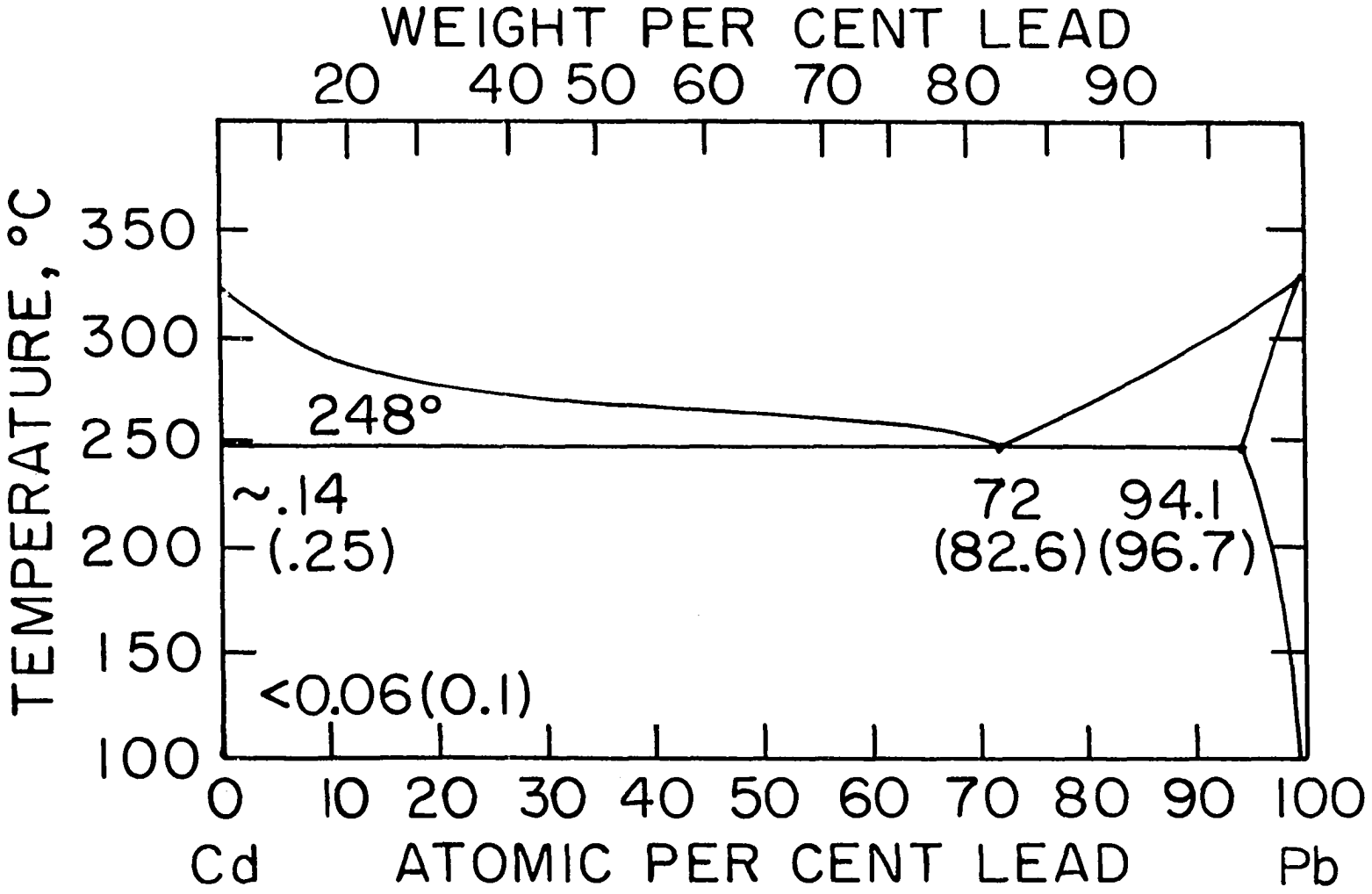
WEIGHT PER CENT LEAD
20 40 50 60 70 80 90
TEMPERATURE, °C
350
300
250
200
150
100
248°
~.14
(.25)
72
(82.6)
94.1
(96.7)
<0.06(0.1)
0 10 20 30 40 50 60 70 80 90 100
Cd
ATOMIC PER CENT LEAD
Pb

Figure 11. An overall view of the experimental apparatus for directional solidification experiments

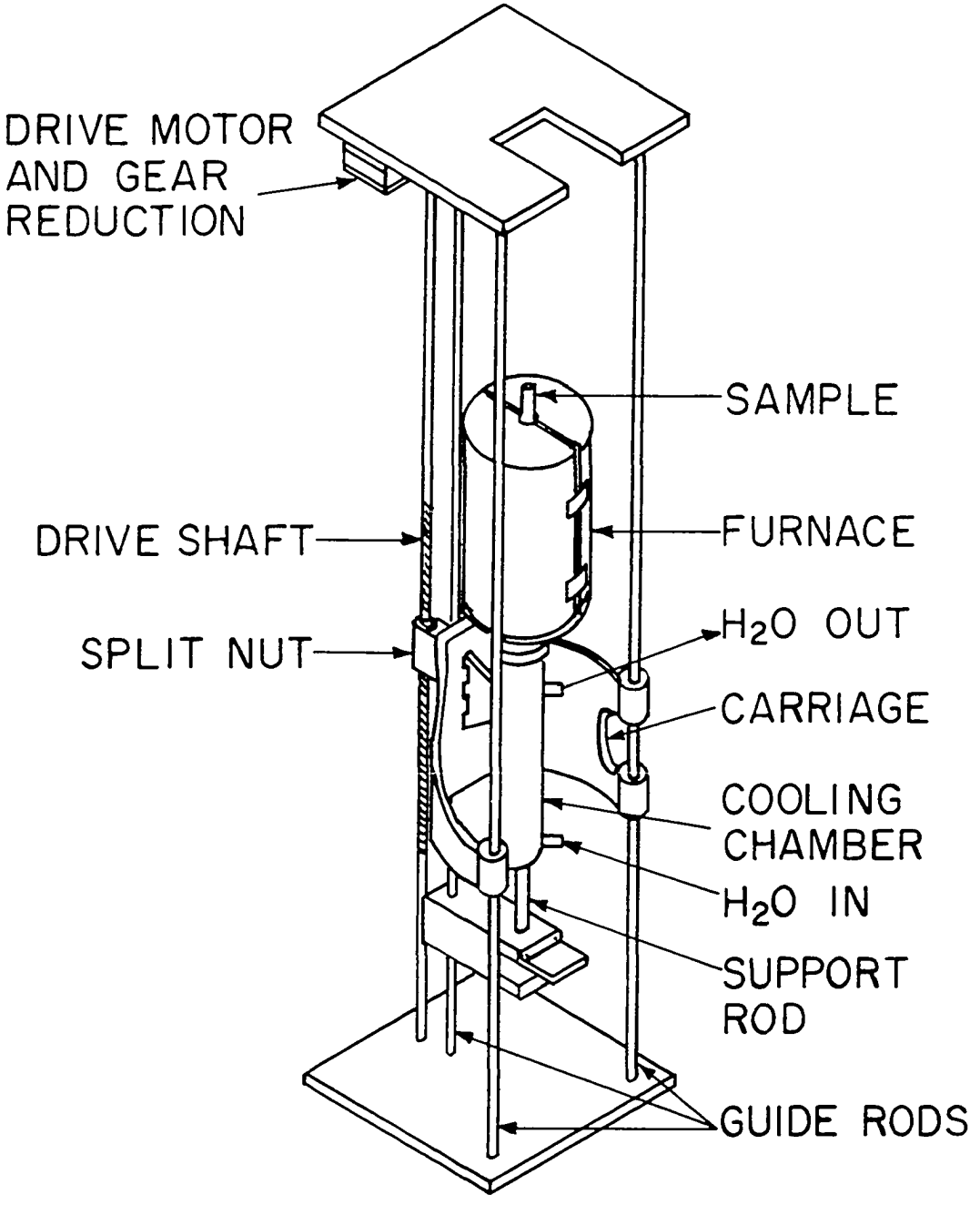
DRIVE MOTOR
AND GEAR
REDUCTION
SAMPLE
DRIVE SHAFT
FURNACE
SPLIT NUT
H_2O OUT
CARRIAGE
COOLING
CHAMBER
H_2O IN
SUPPORT
ROD
GUIDE RODS

Figure 12. A sectional view of the alloy and surrounding equipment

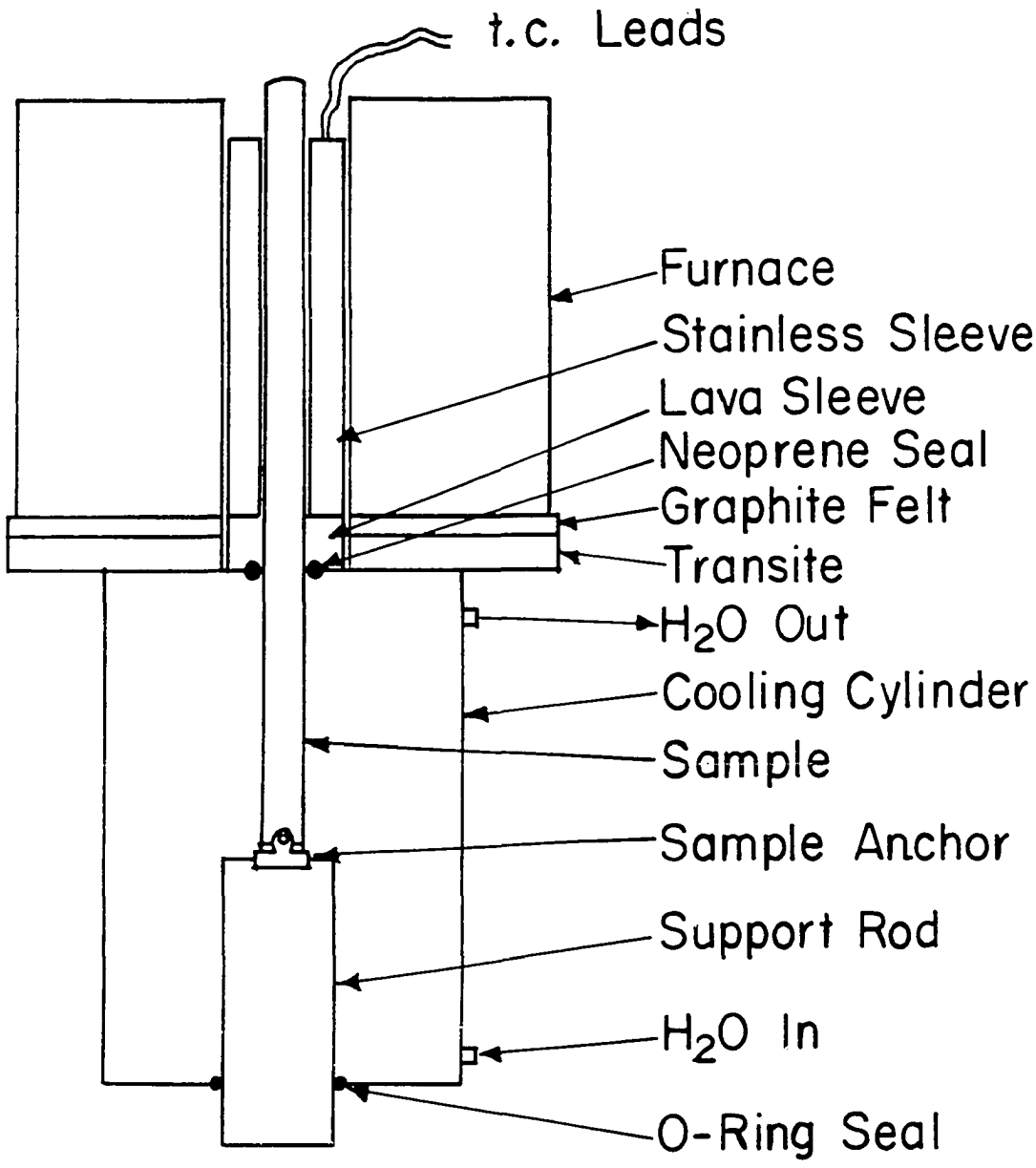
t.c. Leads
Furnace
Stainless Sleeve
Lava Sleeve
Neoprene Seal
Graphite Felt
Transite
H_2O Out
Cooling Cylinder
Sample
Sample Anchor
Support Rod
H_2O In
O-Ring Seal

Figure 13. Block diagram of apparatus used to record I-V characteristics in a magnetic field

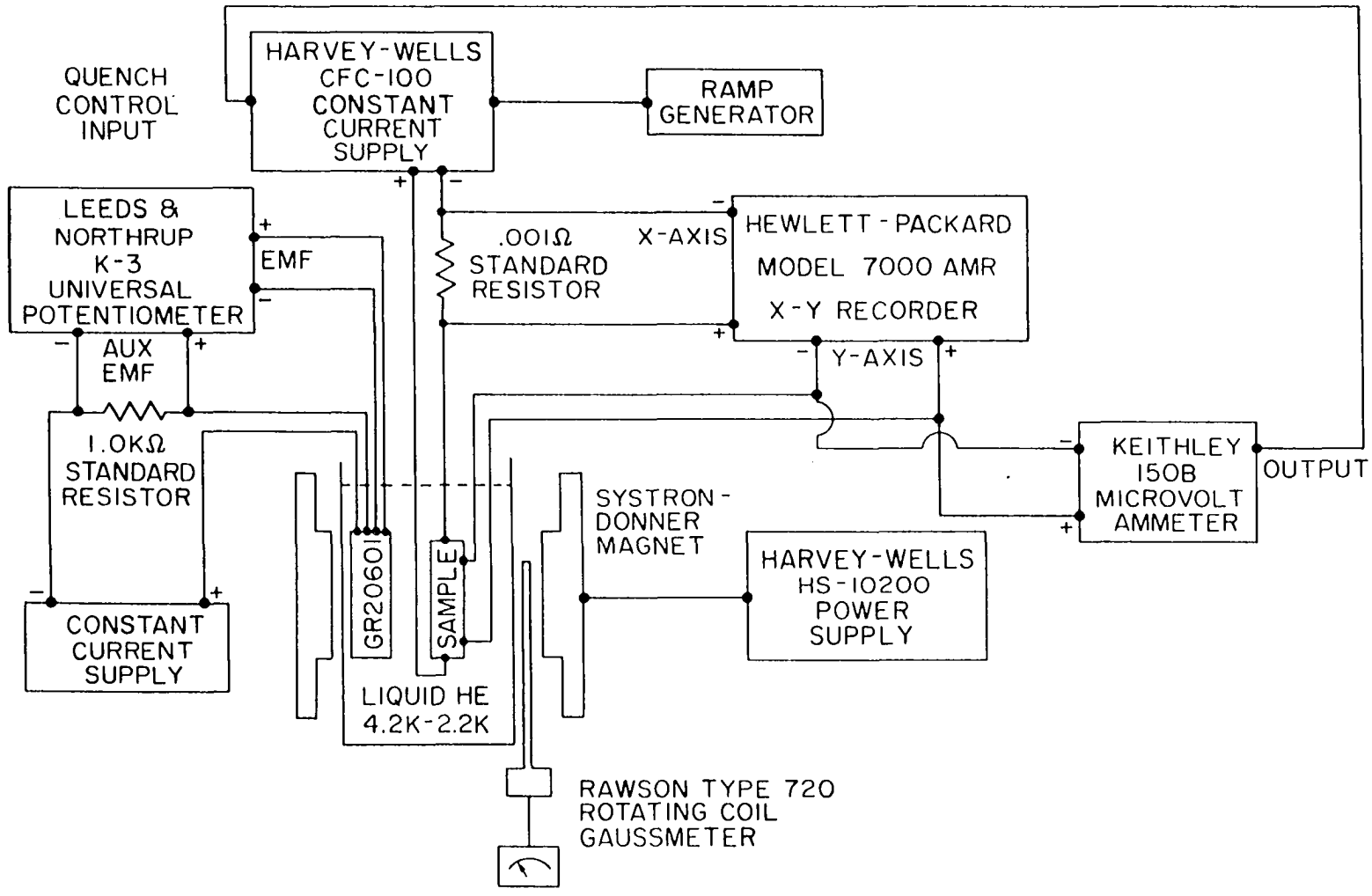
QUENCH CONTROL INPUT
HARVEY-WELLS CFC-100 CONSTANT CURRENT SUPPLY
RAMP GENERATOR
LEEDS & NORTHRUP K-3 UNIVERSAL POTENTIOMETER
EMF
AUX EMF
.001Ω STANDARD RESISTOR
X-AXIS
HEWLETT-PACKARD MODEL 7000 AMR X-Y RECORDER
Y-AXIS
1.0KΩ STANDARD RESISTOR
KEITHLEY 150B MICROVOLT AMMETER
OUTPUT
CONSTANT CURRENT SUPPLY
GR20601
SAMPLE
SYSTRON-DONNER MAGNET
HARVEY-WELLS HS-10200 POWER SUPPLY
LIQUID HE 4.2K-2.2K
RAWSON TYPE 720 ROTATING COIL GAUSSMETER

Figure 14. Block diagram of apparatus used to measure sample voltage as a function of magnetic field

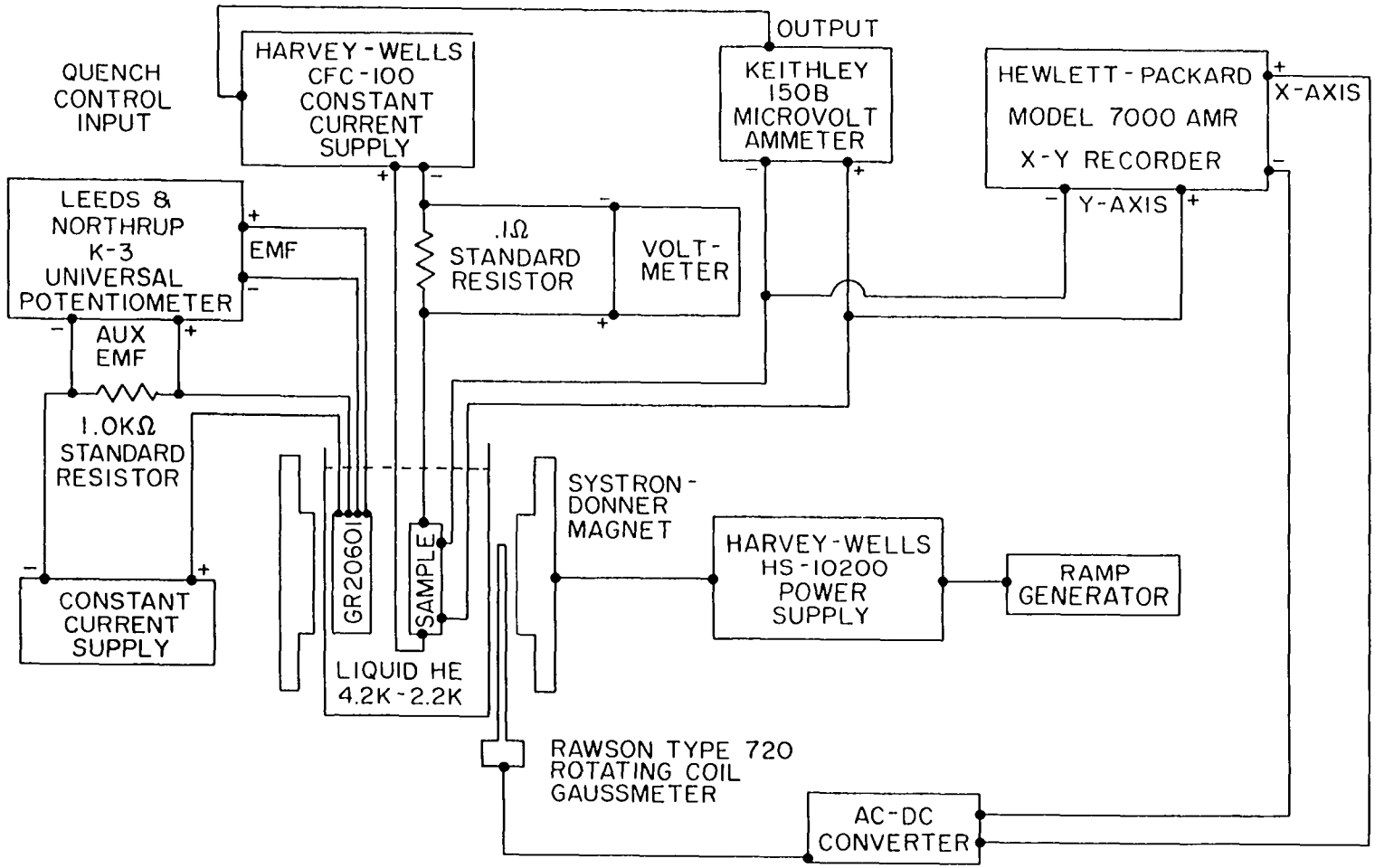
QUENCH CONTROL INPUT
HARVEY-WELLS CFC-100 CONSTANT CURRENT SUPPLY
OUTPUT
KEITHLEY 150B MICROVOLT AMMETER
HEWLETT-PACKARD MODEL 7000 AMR X-Y RECORDER
X-AXIS
Y-AXIS
LEEDS & NORTHRUP K-3 UNIVERSAL POTENTIOMETER
EMF
AUX EMF
.1Ω STANDARD RESISTOR
VOLT-METER
1.0KΩ STANDARD RESISTOR
CONSTANT CURRENT SUPPLY
GR20601
SAMPLE
LIQUID HE 4.2K-2.2K
SYSTRON-DONNER MAGNET
HARVEY-WELLS HS-10200 POWER SUPPLY
RAMP GENERATOR
RAWSON TYPE 720 ROTATING COIL GAUSSMETER
AC-DC CONVERTER

Figure 15. Sample geometry for resistive measurements with transport current parallel the lamellae (not drawn to scale)

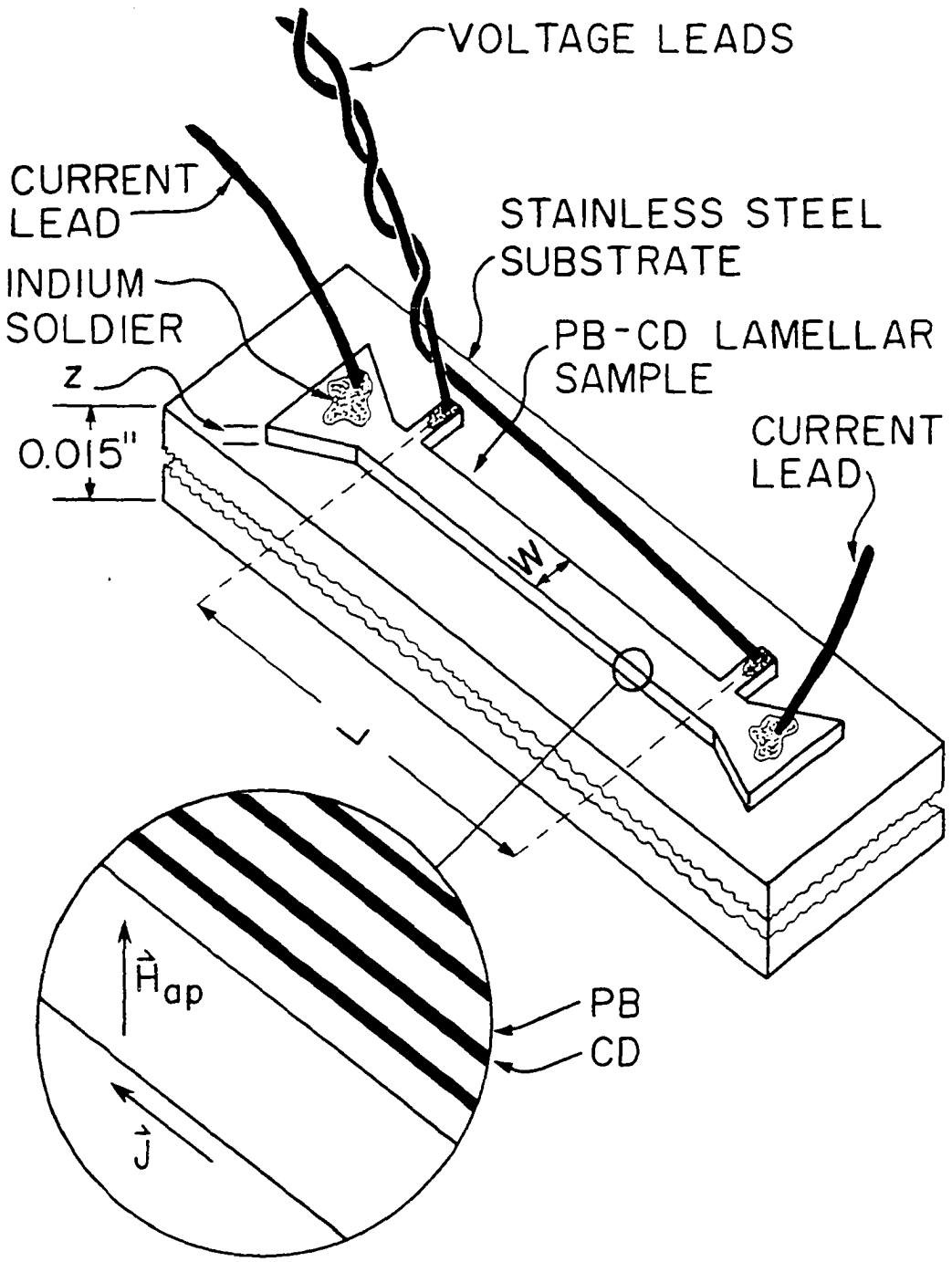
VOLTAGE LEADS
CURRENT LEAD
INDIUM SOLDIER
STAINLESS STEEL SUBSTRATE
PB-CD LAMELLAR SAMPLE
CURRENT LEAD
z
0.015"
W
L
$\vec{H}_{ap}$
$\vec{J}$
PB
CD

Figure 16. Low temperature tail of helium-3 cryostat

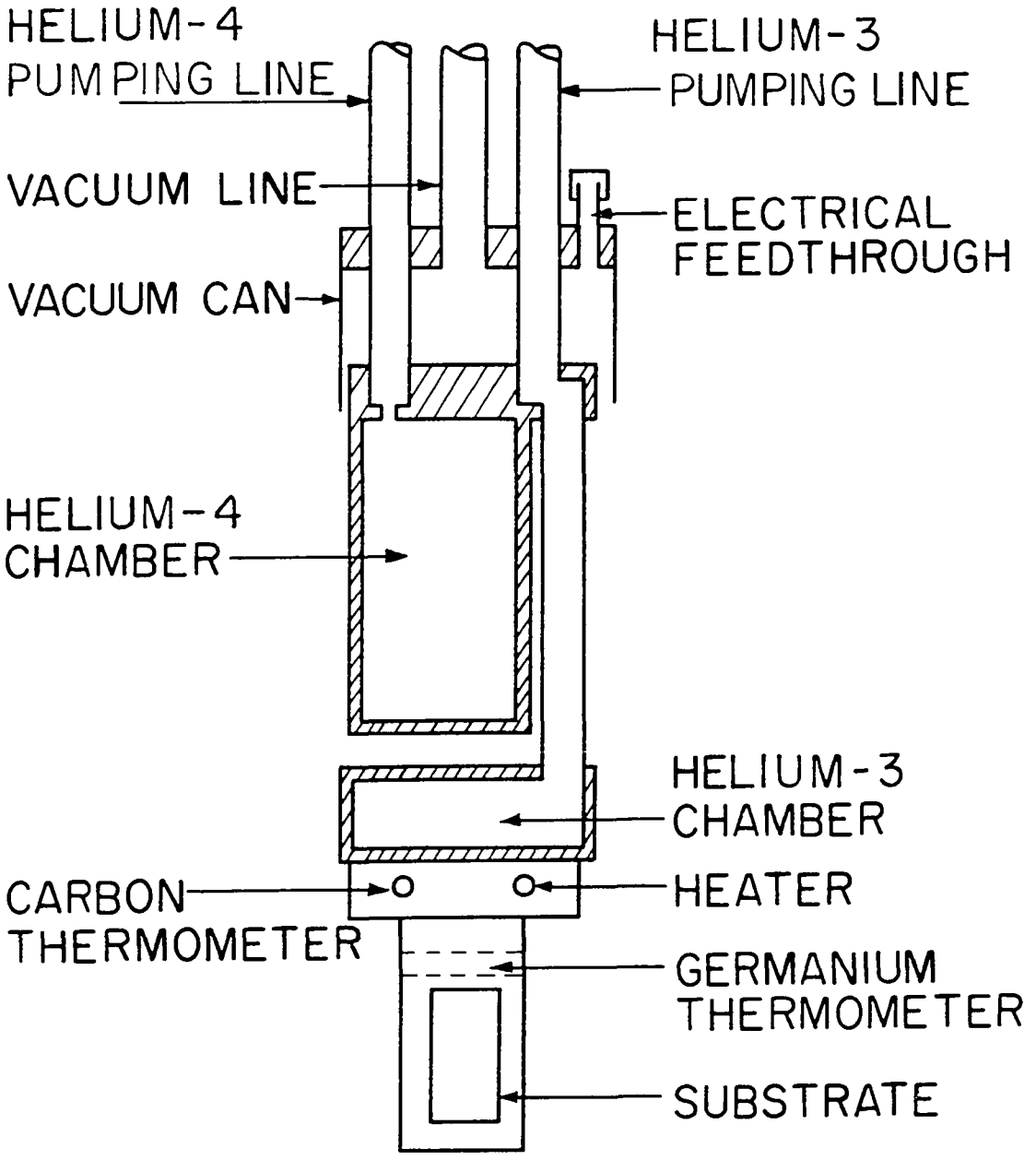
HELIUM-4
PUMPING LINE
HELIUM-3
PUMPING LINE
VACUUM LINE
ELECTRICAL
FEEDTHROUGH
VACUUM CAN
HELIUM-4
CHAMBER
HELIUM-3
CHAMBER
CARBON
THERMOMETER
HEATER
GERMANIUM
THERMOMETER
SUBSTRATE

Figure 17. Sample geometry for resistive measurements with transport current perpendicular the lamellae (not drawn to scale)

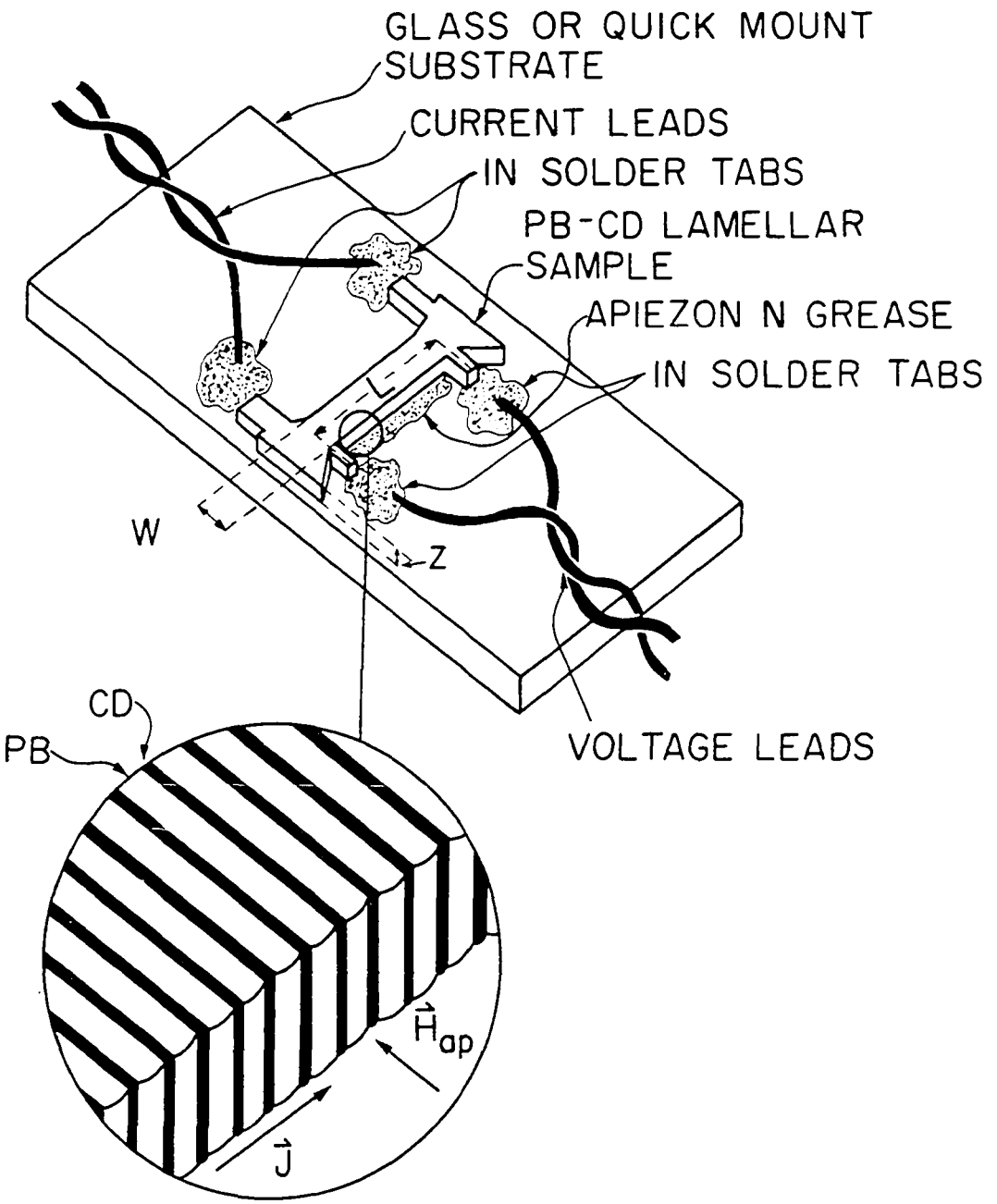
GLASS OR QUICK MOUNT
SUBSTRATE
CURRENT LEADS
IN SOLDER TABS
PB-CD LAMELLAR
SAMPLE
APIEZON N GREASE
IN SOLDER TABS
W
Z
VOLTAGE LEADS
CD
PB
$\vec{H}_{ap}$
$\vec{J}$

Figure 18. SEM micrographs of directionally solidified Pb-Cd eutectic alloy after 2 hours of room temperature annealing:
a) 17,500x, b) 4400x, c) 440x, d) 3800x

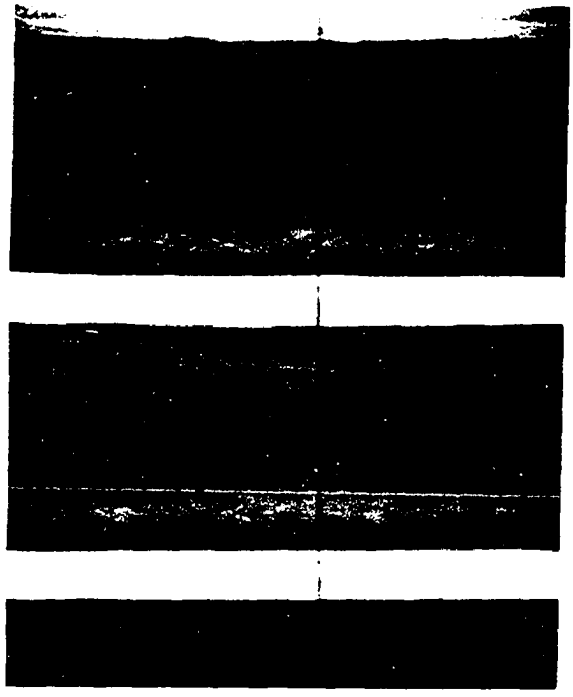

a

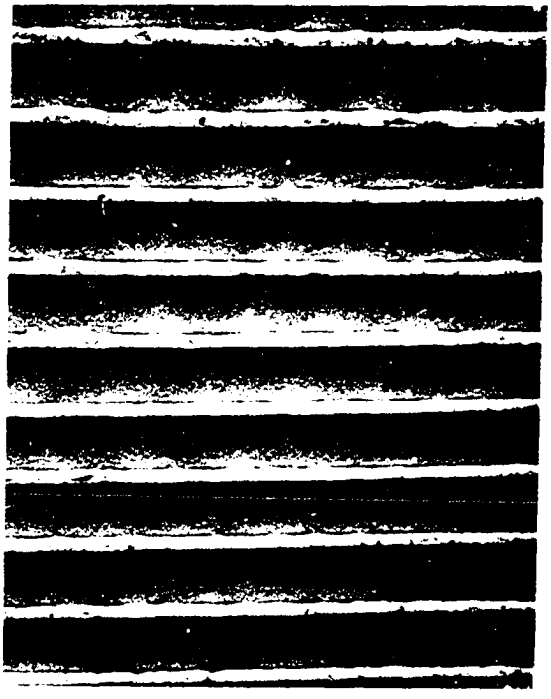

b

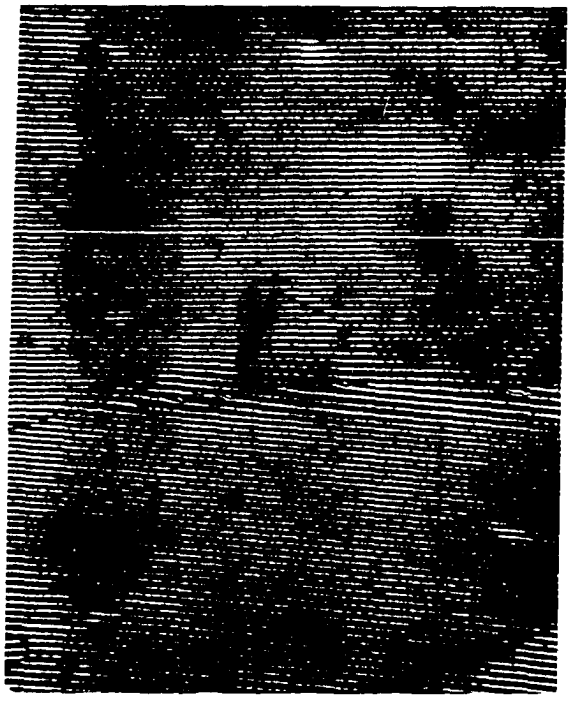

c

d

Figure 19. SEM micrographs of directionally solidified Pb-Cd eutectic alloy after increased annealing times at room temperature: a) 17,500x after 2 hours, b,c) 16,000x after 3 days, d) 15,500x after 1 month

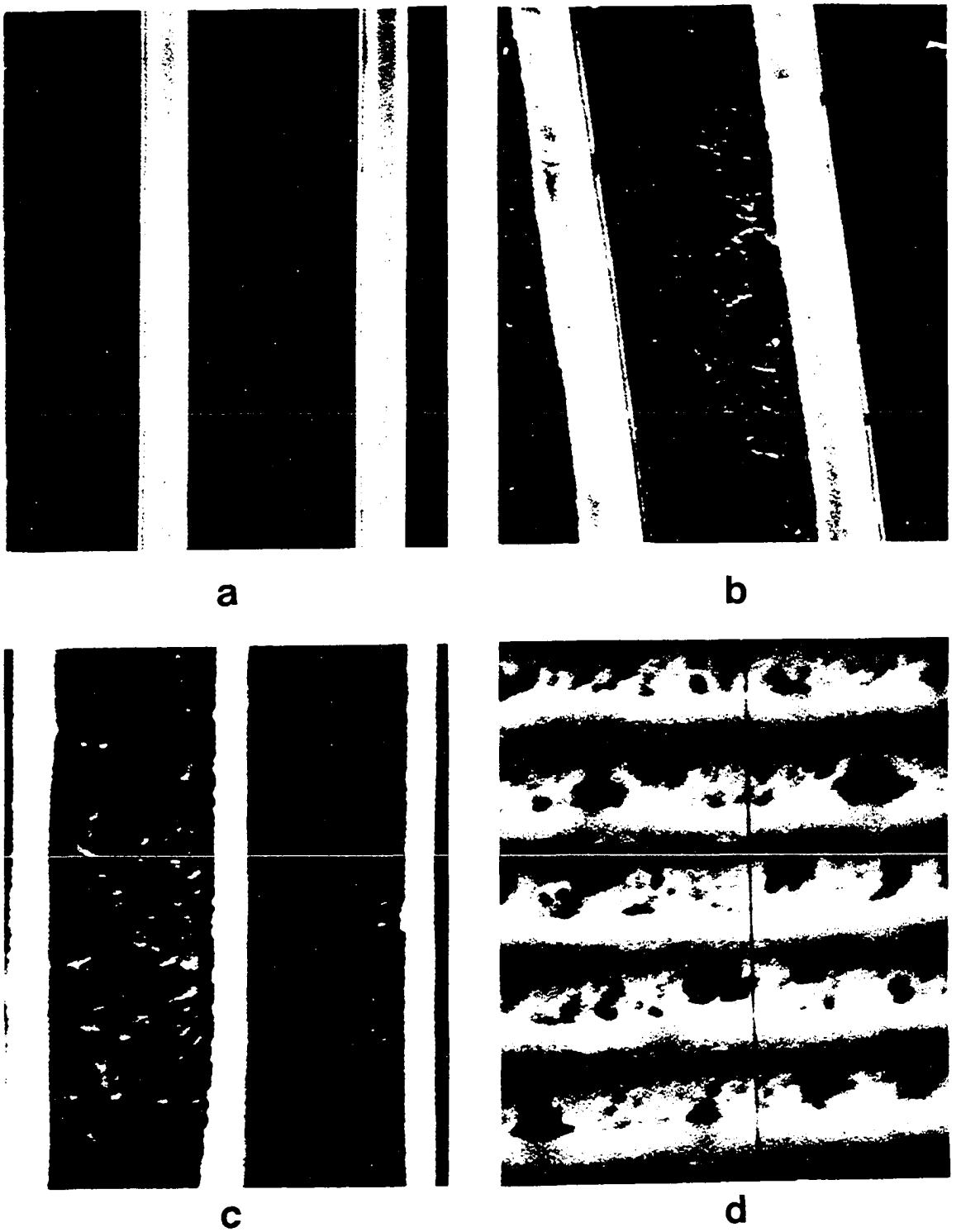
a
b
c
d

Figure 20. Resistivity of Cd rods as a function of Pb dissolved in the rods

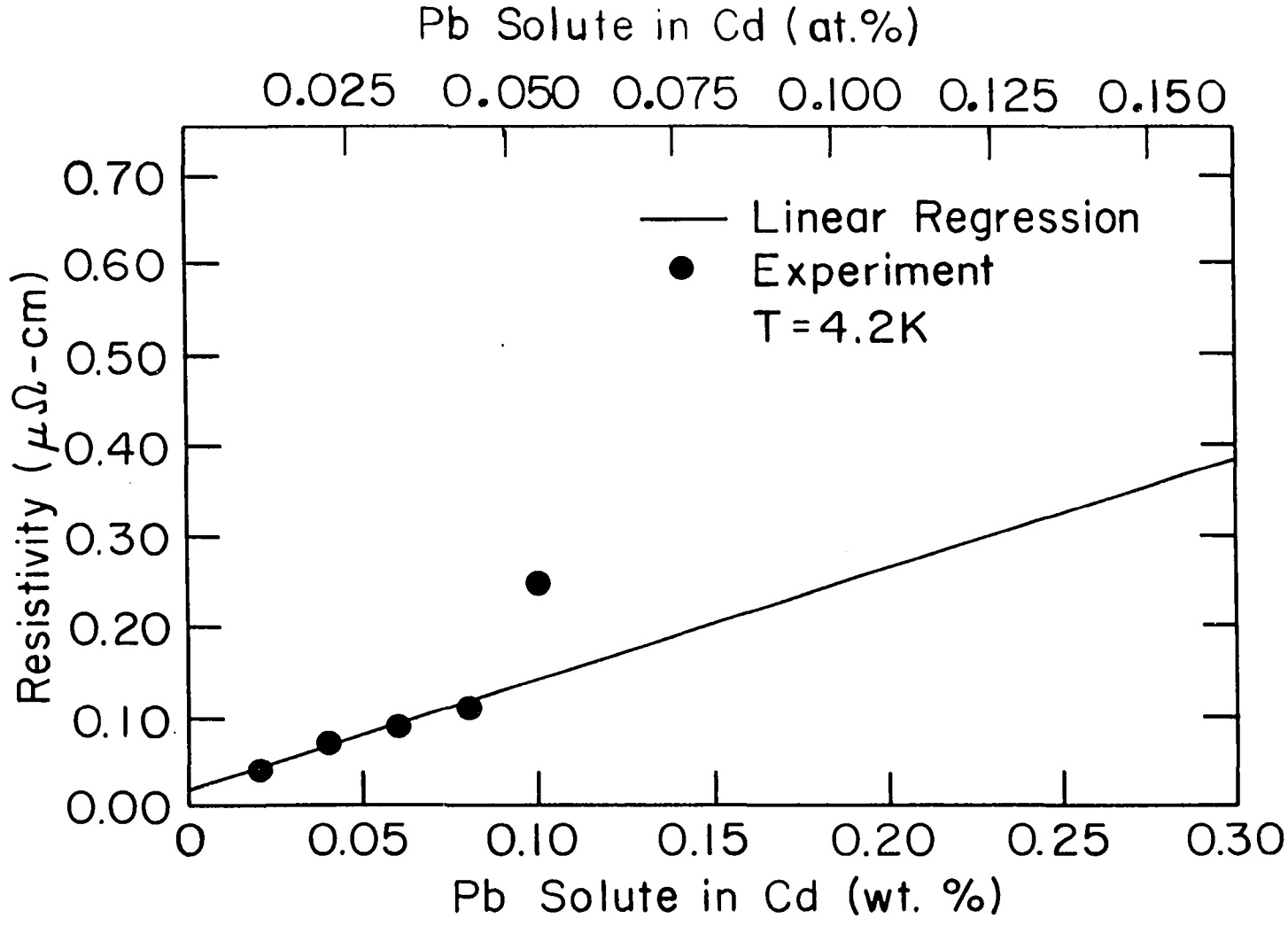
Pb Solute in Cd (at.%)
0.025 0.050 0.075 0.100 0.125 0.150
0.70
0.60
0.50
0.40
0.30
0.20
0.10
0.00
Resistivity (μΩ-cm)
Linear Regression
Experiment
T=4.2K
0 0.05 0.10 0.15 0.20 0.25 0.30
Pb Solute in Cd (wt. %)

Figure 21. Dependence of Pb resistivity upon lamellar period in directionally solidified Pb-Cd eutectic alloys

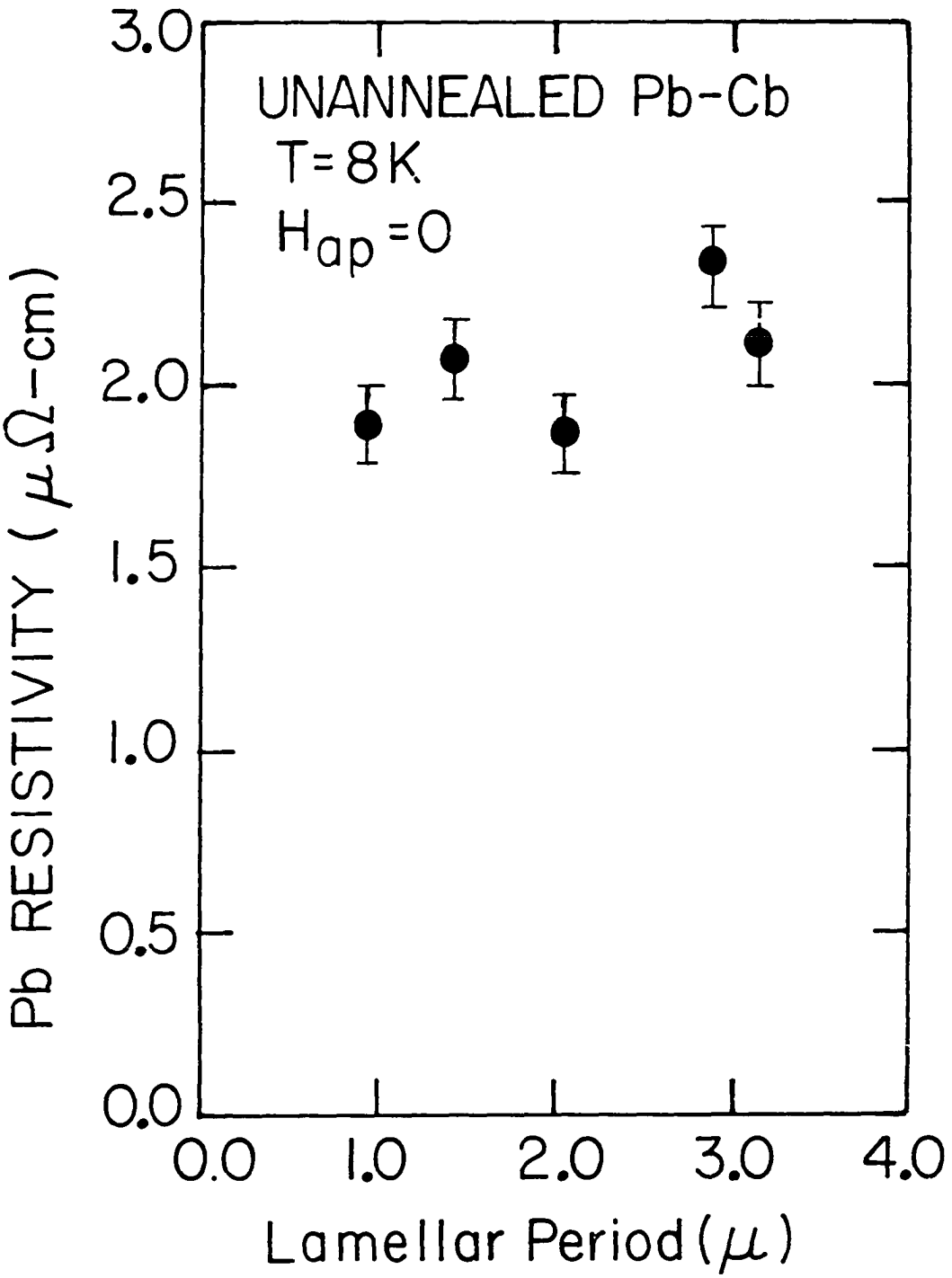
UNANNEALED Pb-Cb
T=8K
H_{ap}=0
Pb RESISTIVITY ($\mu\Omega$-cm)
Lamellar Period (μ)
3.0
2.5
2.0
1.5
1.0
0.5
0.0
0.0
1.0
2.0
3.0
4.0

Figure 22. Sample resistivity in parallel geometry as a function of lamellar period

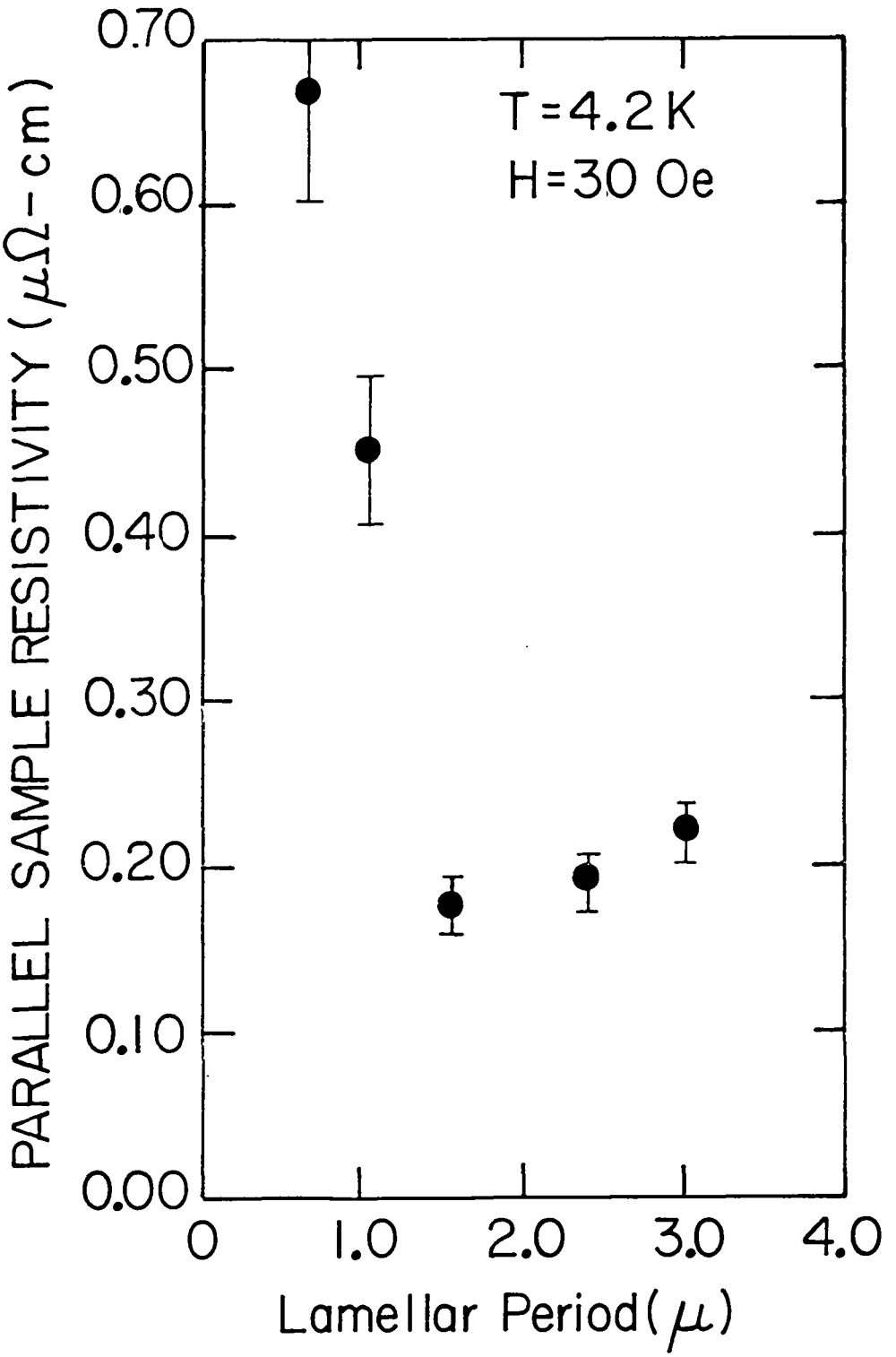
T=4.2 K
H=30 Oe
PARALLEL SAMPLE RESISTIVITY (μΩ-cm)
0.70
0.60
0.50
0.40
0.30
0.20
0.10
0.00
0
1.0
2.0
3.0
4.0
Lamellar Period(μ)

Figure 23. Magnetization data taken on quenched Pb-Cd eutectic alloy (from J. D. Livingston, General Electric Corporate Res. and Dev. Lab)

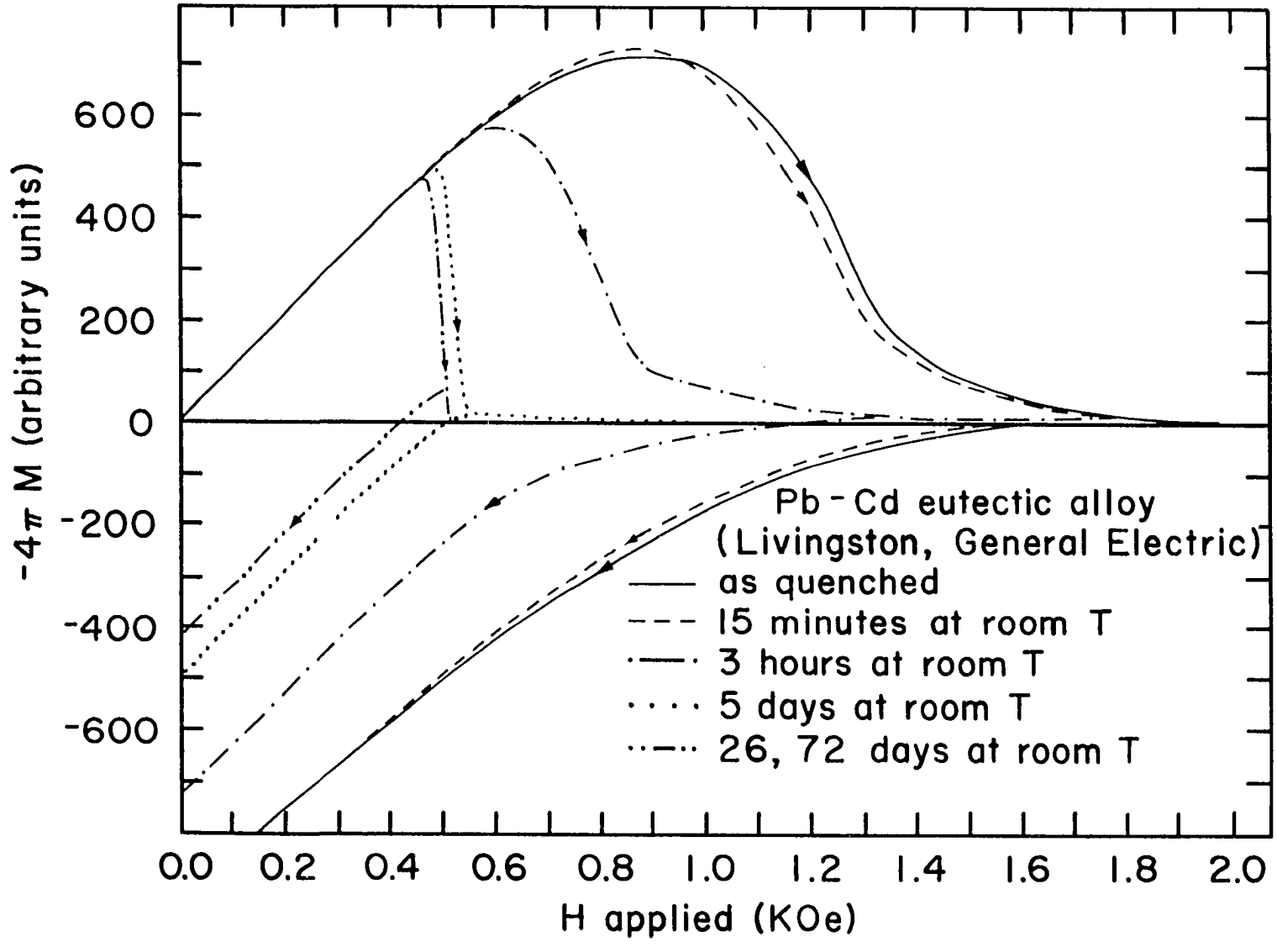
600
400
200
0
-200
-400
-600
-4π M (arbitrary units)
0.0
0.2
0.4
0.6
0.8
1.0
1.2
1.4
1.6
1.8
2.0
H applied (KOe)
Pb - Cd eutectic alloy
(Livingston, General Electric)
as quenched
15 minutes at room T
3 hours at room T
5 days at room T
26, 72 days at room T

Figure 24. Superconducting transition temperature plotted as a function of the Pb thickness. The circles depict the lamellar eutectic Pb-Cd system and the squares show thin film tunneling data on Pb-Cd sandwiches

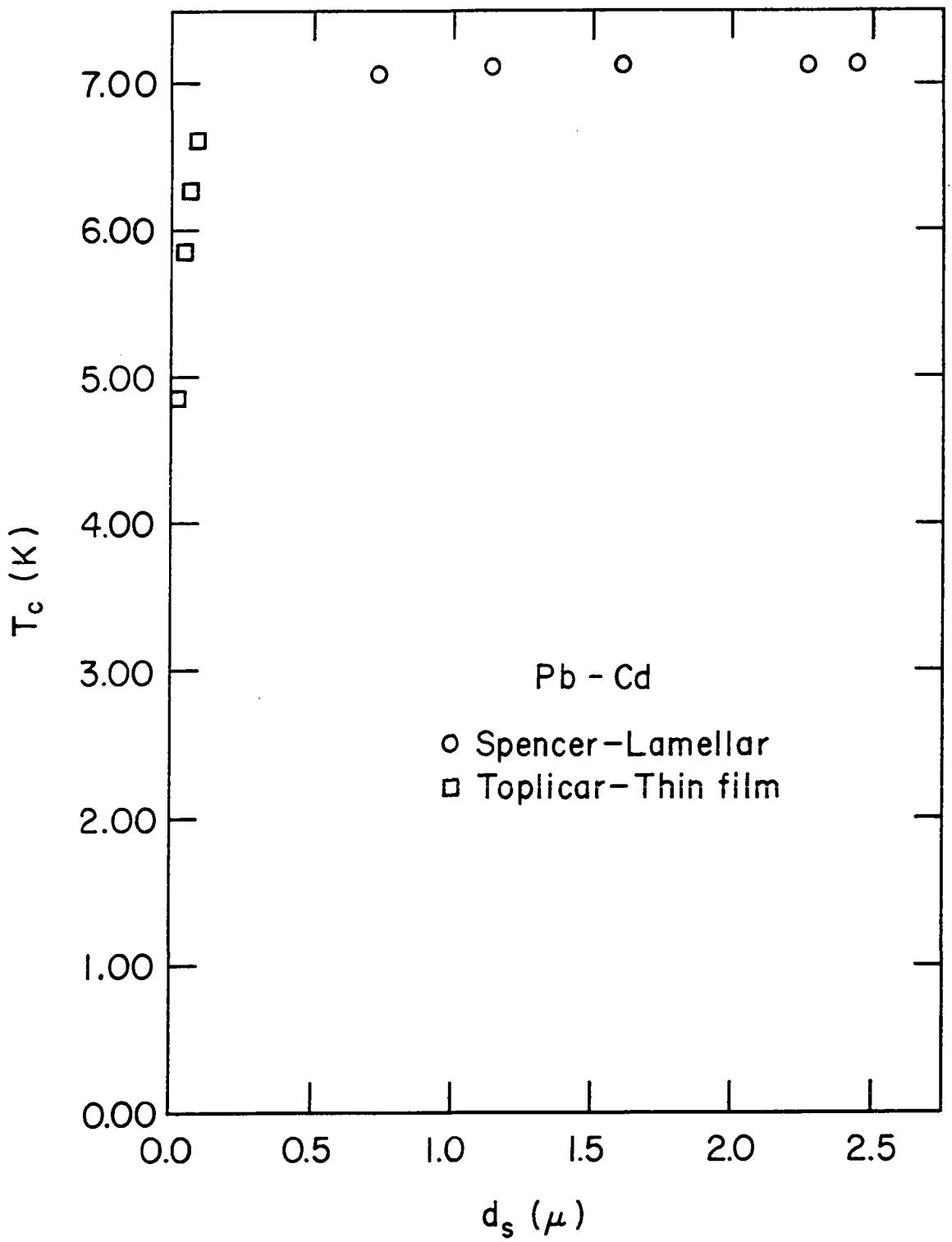
7.00
6.00
5.00
4.00
3.00
2.00
1.00
0.00
T_c (K)
0.0
0.5
1.0
1.5
2.0
2.5
d_s (μ)
Pb - Cd
o Spencer–Lamellar
□ Toplicar–Thin film

Figure 25. Superconducting transition temperature plotted as a function of lamellar period. The circles show the experimental data, the solid line shows the Werthamer theory, and the dashed line shows the Deutscher-de Gennes theory

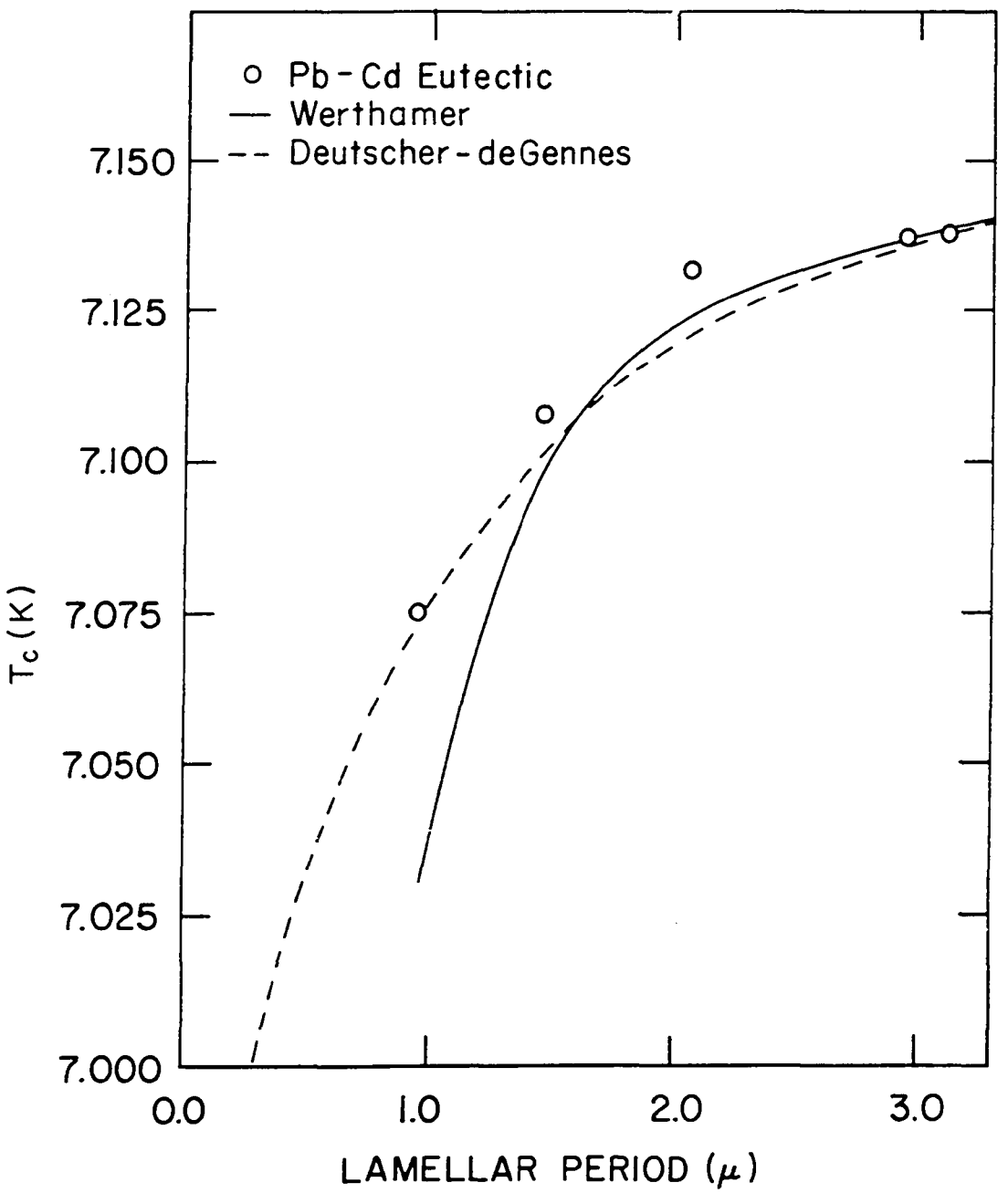
o Pb - Cd Eutectic
— Werthamer
-- Deutscher - deGennes
7.150
7.125
7.100
7.075
7.050
7.025
7.000
T_c (K)
0.0
1.0
2.0
3.0
LAMELLAR PERIOD (μ)

Figure 26. Linear regression fit of data to Deutscher-de Gennes theory. Inset shows significance of extrapolation length b

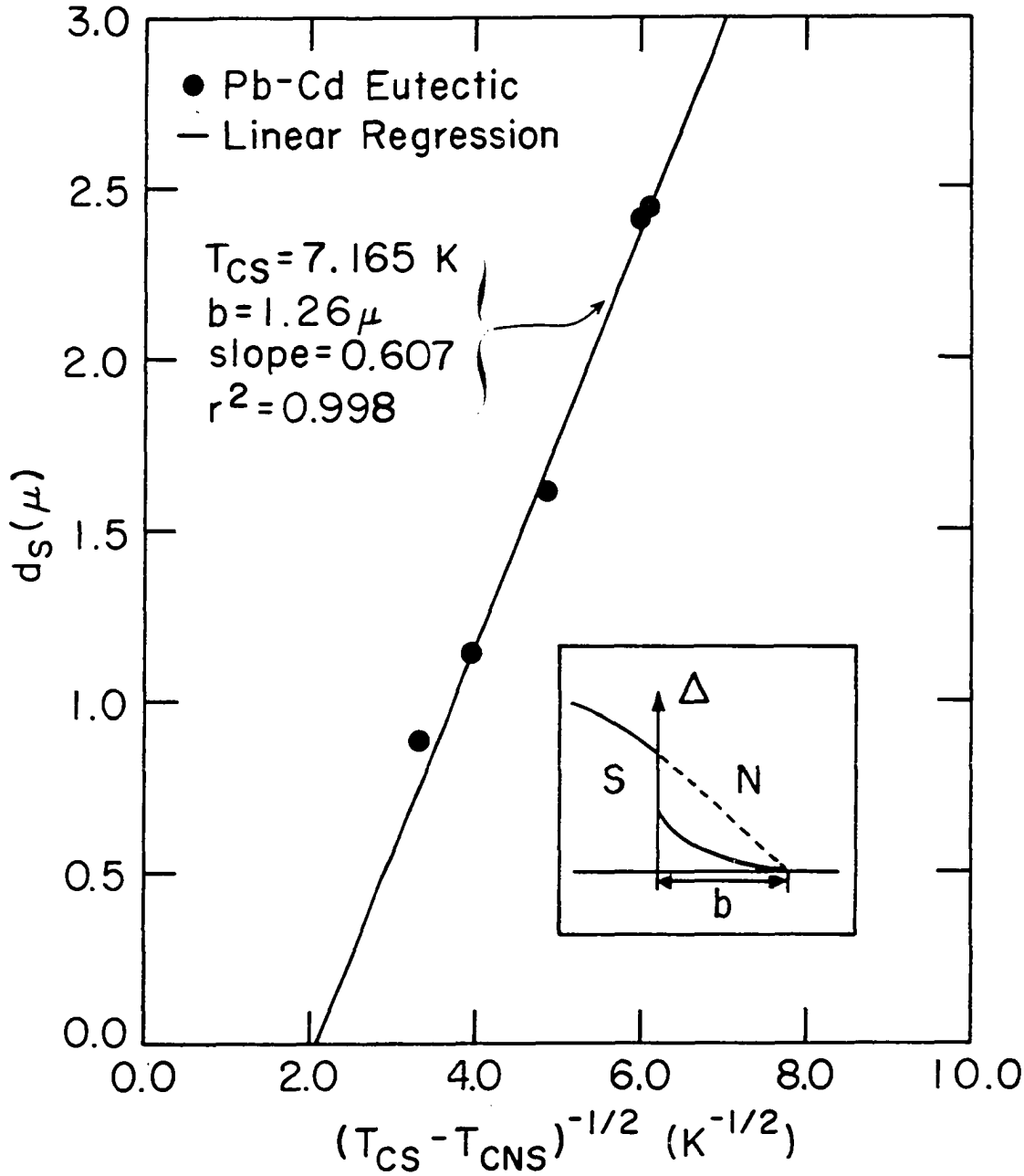
3.0
2.5
2.0
1.5
1.0
0.5
0.0
0.0
2.0
4.0
6.0
8.0
10.0
● Pb-Cd Eutectic
— Linear Regression
T_{CS} = 7.165 K
b = 1.26 μ
slope = 0.607
r^2 = 0.998
$d_S(\mu)$
$(T_{CS} - T_{CNS})^{-1/2}$ $(K^{-1/2})$
Δ
S
N
b

Figure 27. Family of I-V characteristics for typical unannealed sample in various applied magnetic fields

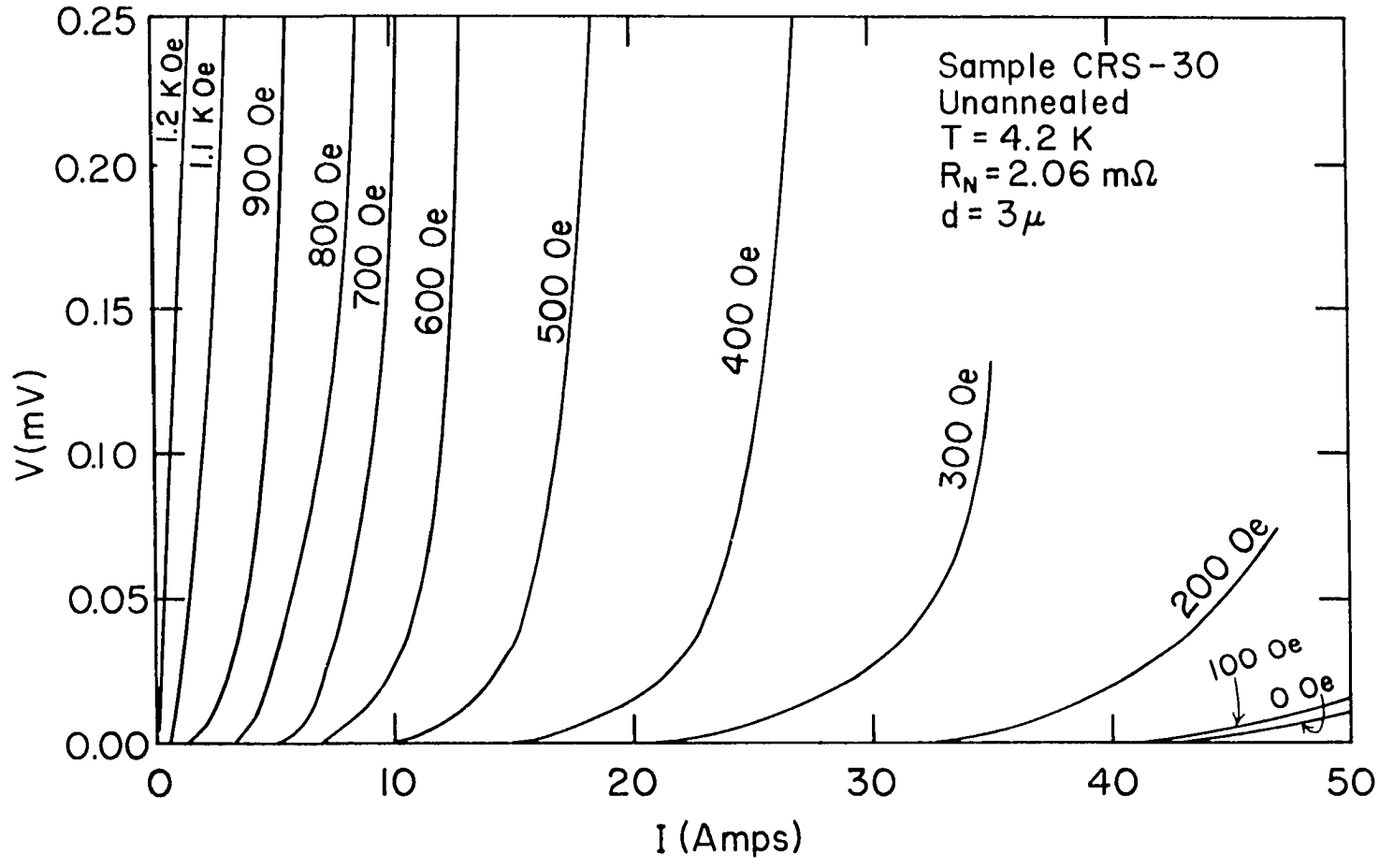
Sample CRS-30
Unannealed
T = 4.2 K
R_N = 2.06 mΩ
d = 3μ
1.2 K Oe
1.1 K Oe
900 Oe
800 Oe
700 Oe
600 Oe
500 Oe
400 Oe
300 Oe
200 Oe
100 Oe
0 Oe
V(mV)
I (Amps)
0.25
0.20
0.15
0.10
0.05
0.00
0
10
20
30
40
50

Figure 28. Family of I-V characteristics for typical annealed sample in various applied magnetic fields

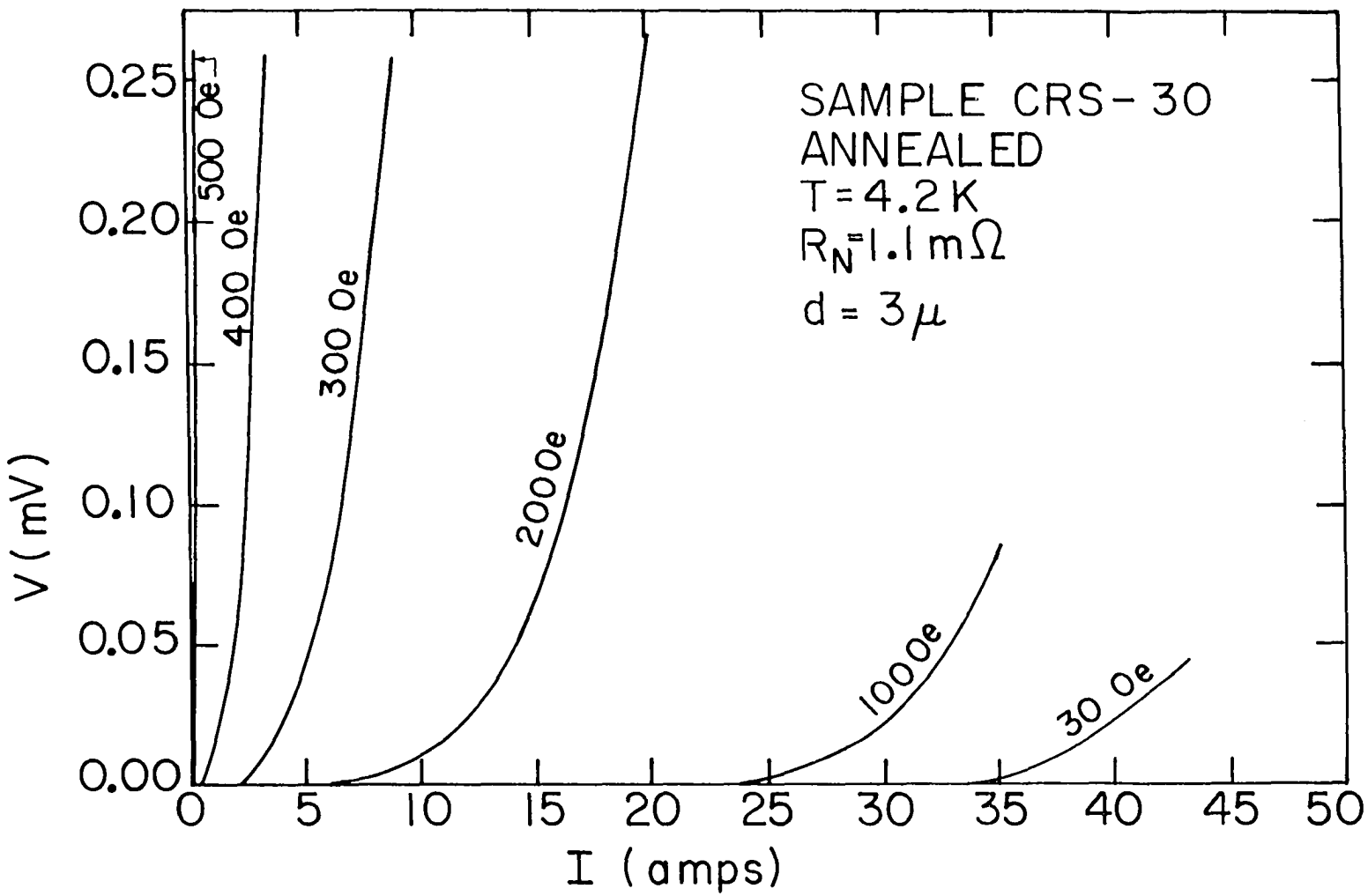
SAMPLE CRS-30
ANNEALED
T=4.2K
R_N=1.1mΩ
d = 3μ
500 Oe
400 Oe
300 Oe
200 Oe
100 Oe
30 Oe
V (mV)
0.25
0.20
0.15
0.10
0.05
0.00
0
5
10
15
20
25
30
35
40
45
50
I (amps)

Figure 29. Critical current density of Pb-Cd in parallel current geometry as a function of lamellar period

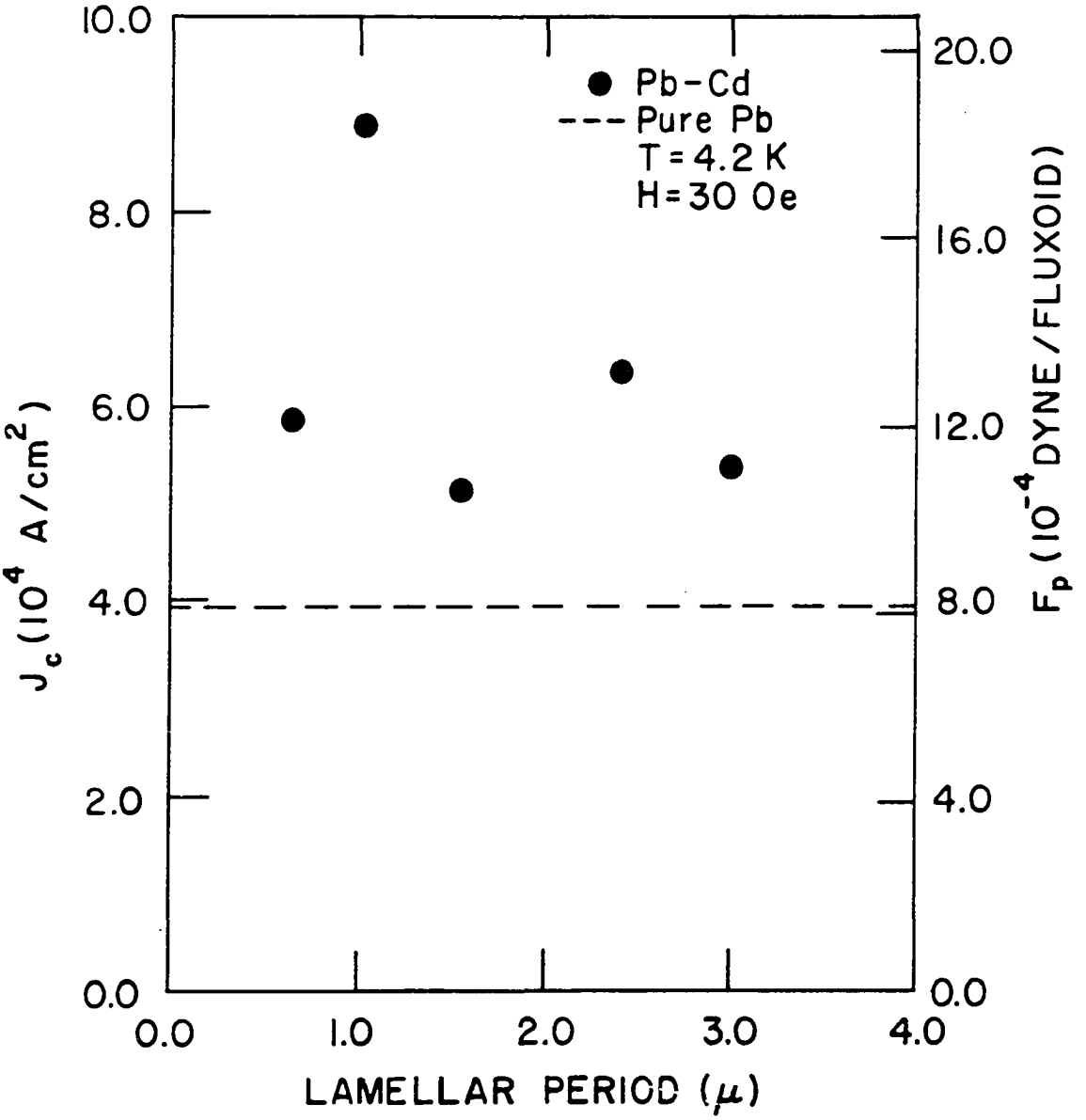
10.0
8.0
6.0
4.0
2.0
0.0
20.0
16.0
12.0
8.0
4.0
0.0
0.0
1.0
2.0
3.0
4.0
Pb-Cd
Pure Pb
T = 4.2 K
H = 30 Oe
J_c (10^4 A/cm^2)
F_p (10^{-4} DYNE/FLUXOID)
LAMELLAR PERIOD (μ)

Figure 30. Critical current density of typical Pb-Cd sample in parallel current geometry as a function of applied magnetic field. Circles show sample when unannealed and squares show annealed sample behavior

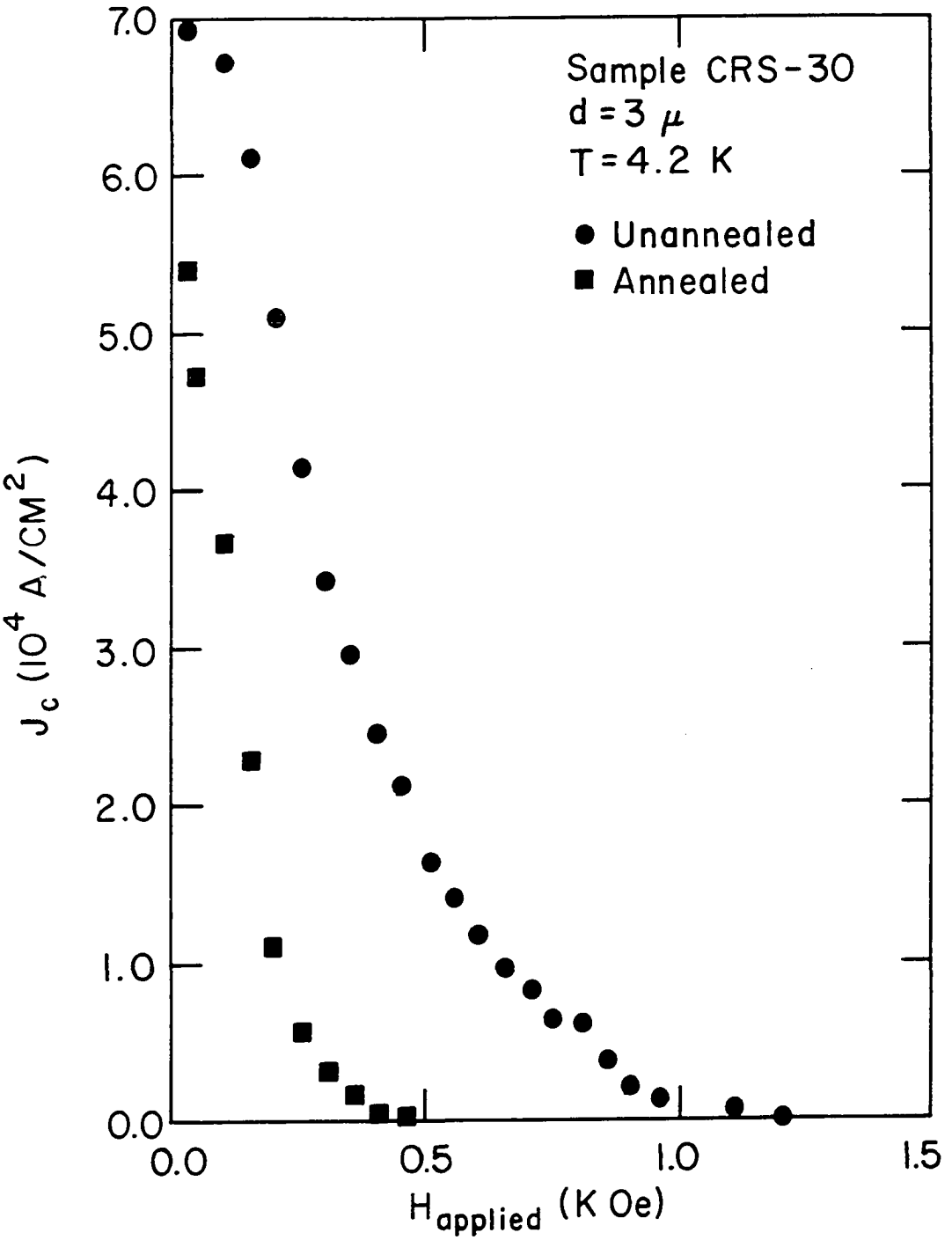
Sample CRS-30
d = 3 μ
T = 4.2 K
● Unannealed
■ Annealed
7.0
6.0
5.0
4.0
3.0
2.0
1.0
0.0
0.0
0.5
1.0
1.5
J_c (10^4 A/CM^2)
$H_{applied}$ (K Oe)

Figure 31. Critical current density of directionally solidified pure Pb in same sample geometry as Pb-Cd samples

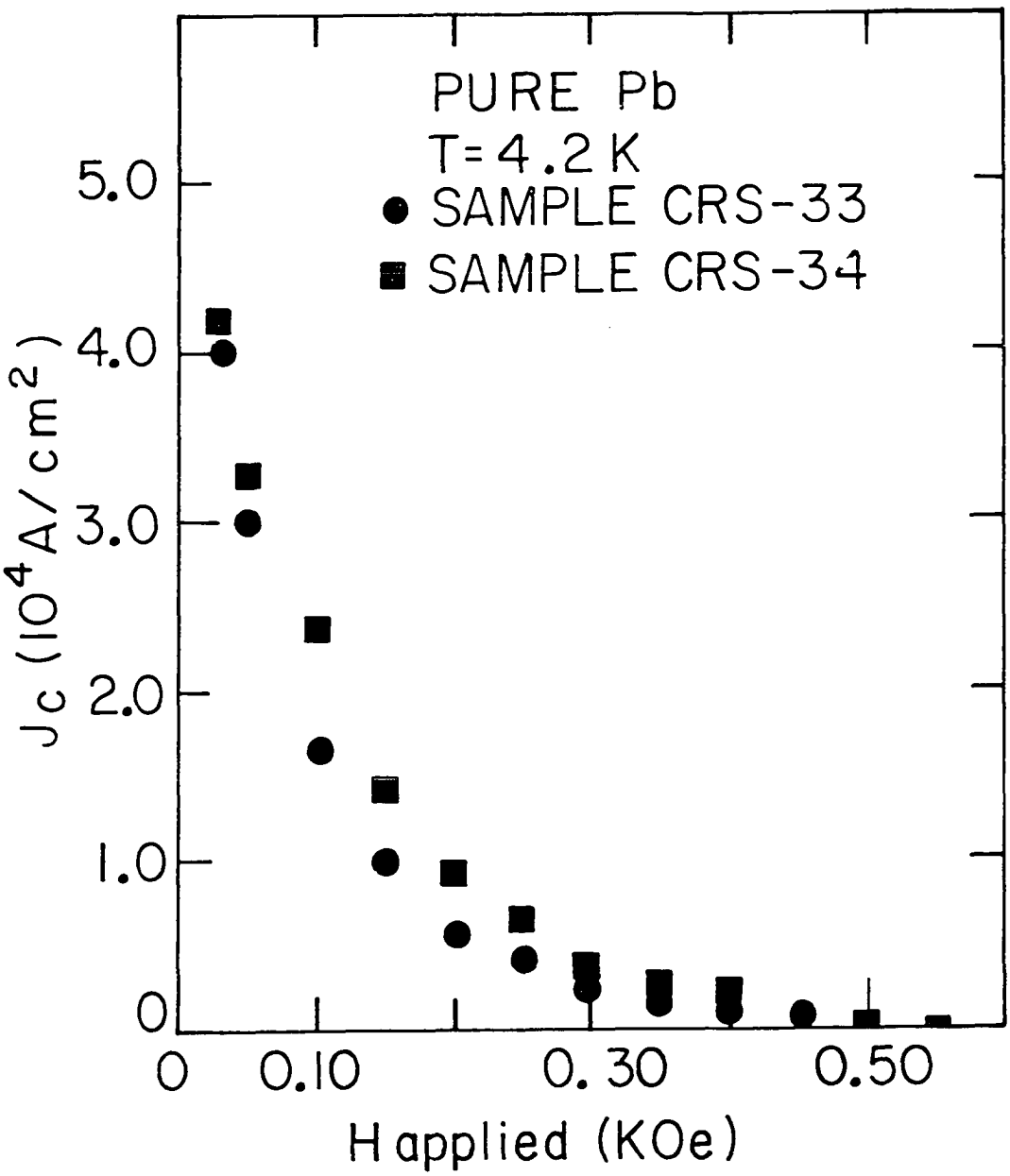
PURE Pb
T=4.2 K
SAMPLE CRS-33
SAMPLE CRS-34
5.0
4.0
3.0
2.0
1.0
0
Jc (10⁴A/cm²)
0
0.10
0.30
0.50
H applied (KOe)

Figure 32. Temperature dependence of critical current density of typical Pb-Cd lamellar sample in unannealed and annealed states

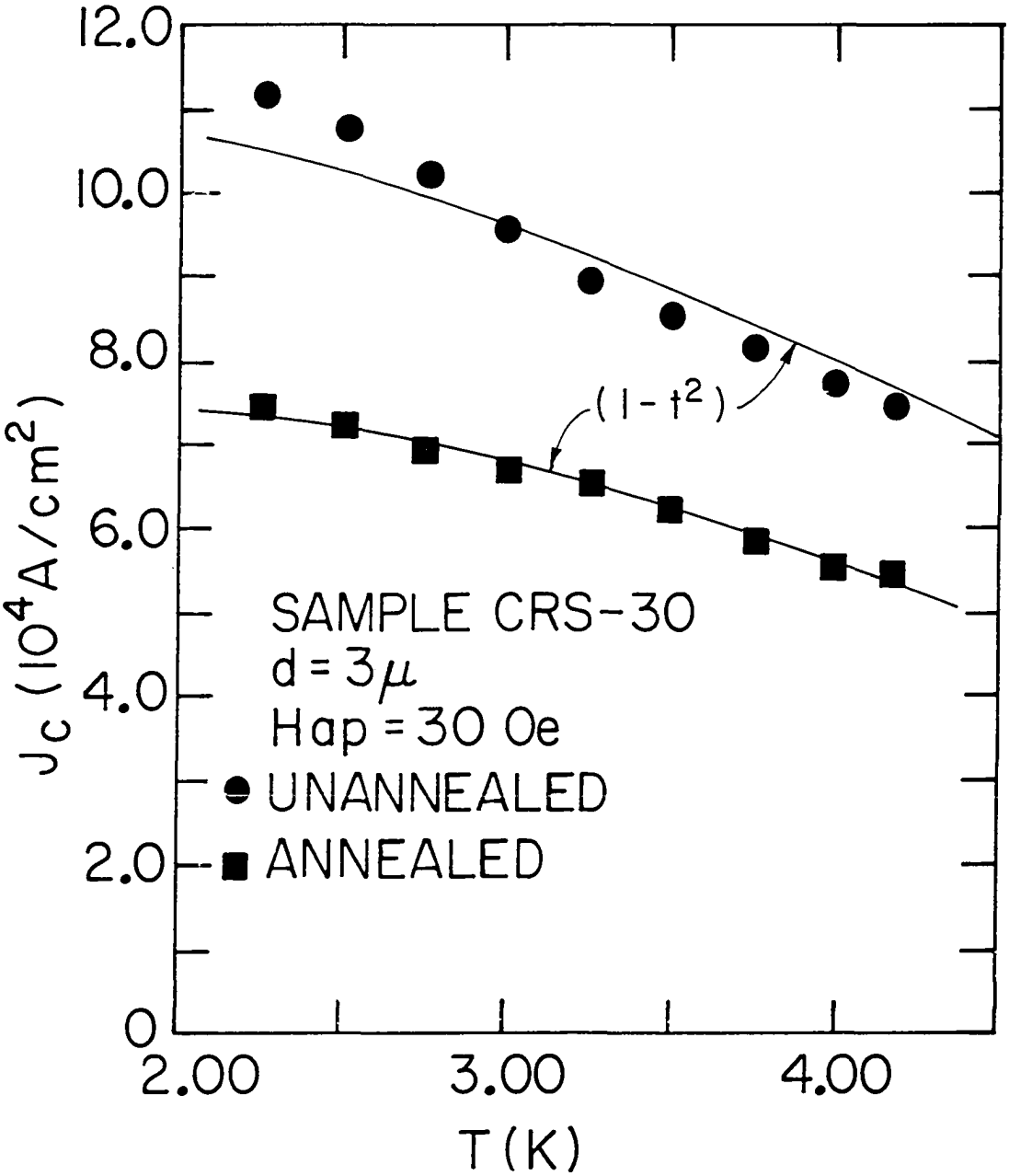
12.0
10.0
8.0
6.0
4.0
2.0
0
J_c (10^4A/cm^2)
$(1-t^2)$
SAMPLE CRS-30
d = 3μ
Hap = 30 Oe
UNANNEALED
ANNEALED
2.00
3.00
4.00
T(K)

Figure 33. Temperature dependence of critical current density of directionally solidified pure Pb samples

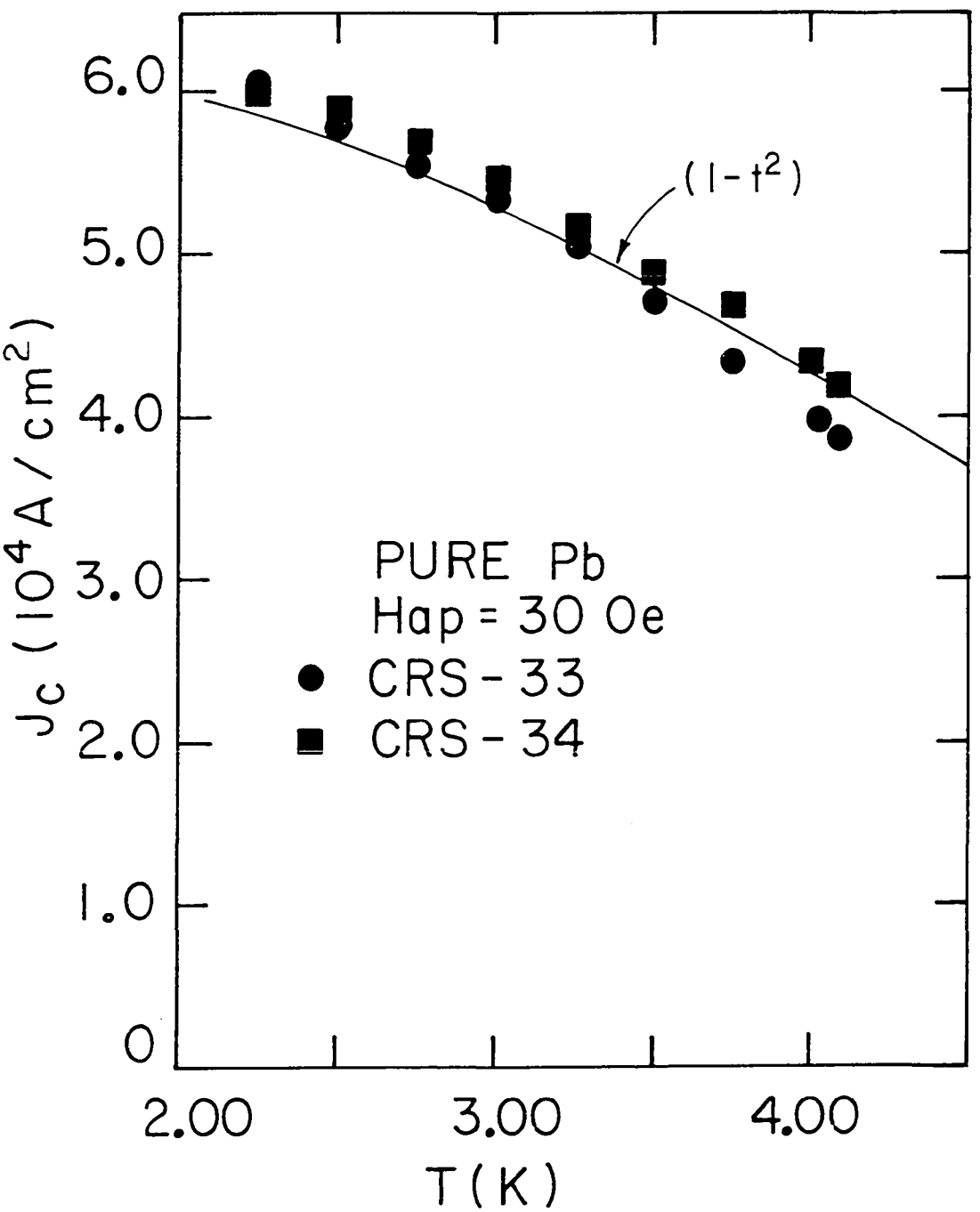
6.0
5.0
4.0
3.0
2.0
1.0
0
J_c (10^4 A / cm^2)
$(1-t^2)$
PURE Pb
Hap = 30 Oe
CRS - 33
CRS - 34
2.00
3.00
4.00
T(K)

Figure 34. Temperature dependence of critical fields of unannealed and annealed Pb-Cd sample. Solid line shows pure Pb bulk critical field

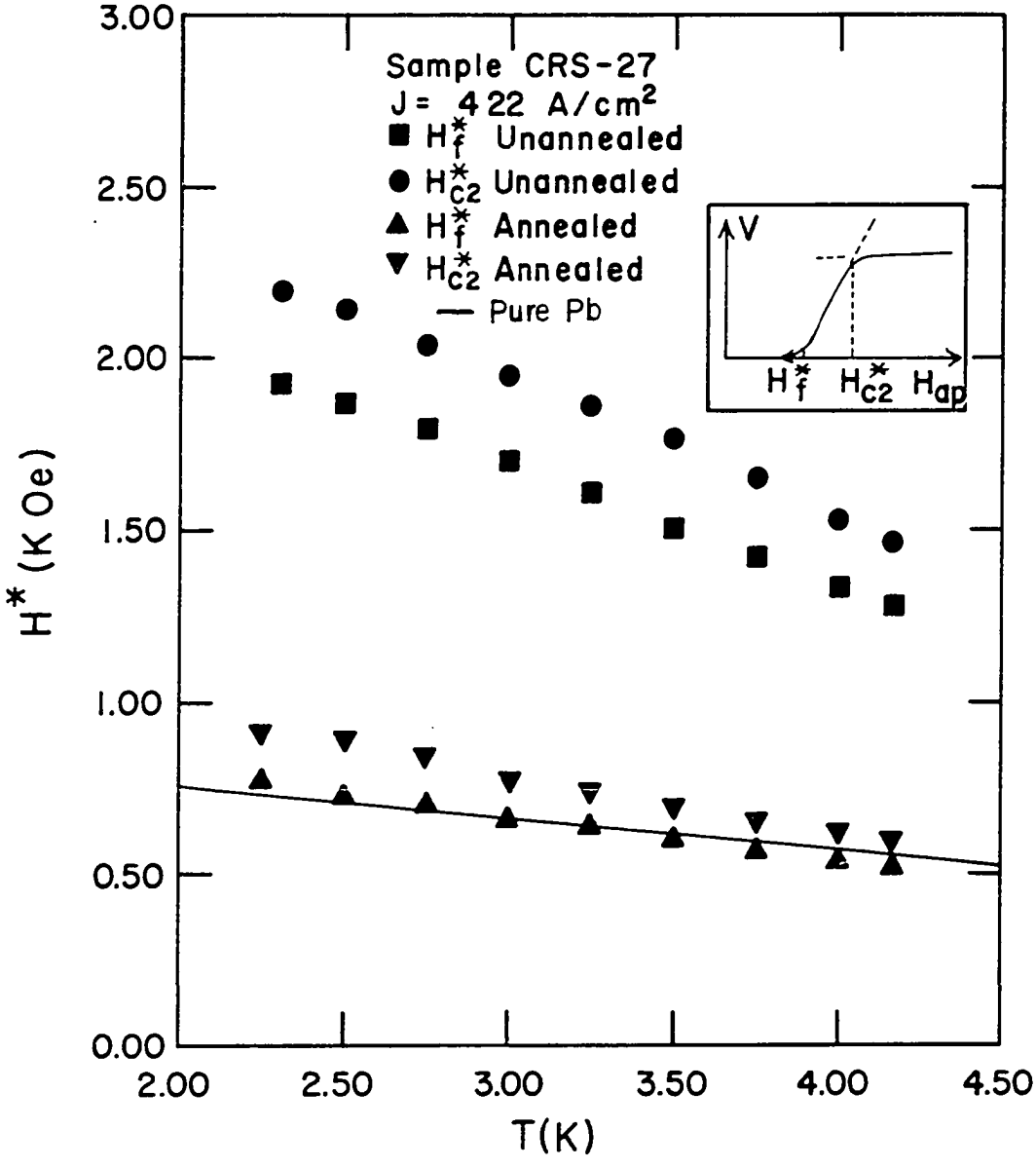
Sample CRS-27
J = 422 A/cm²
H*f Unannealed
H*c2 Unannealed
H*f Annealed
H*c2 Annealed
Pure Pb
V
H*f
H*c2
Hap
H*(K Oe)
T(K)
3.00
2.50
2.00
1.50
1.00
0.50
0.00
2.00
2.50
3.00
3.50
4.00
4.50

Figure 35. Resistance versus temperature data taken with SQUID for several applied magnetic fields. Sample is in perpendicular current geometry. Dashed lines indicate expected behavior in the absence of the proximity effect in the Cd lamellae. Dotted line shows calculated resistance of Cd lamellae

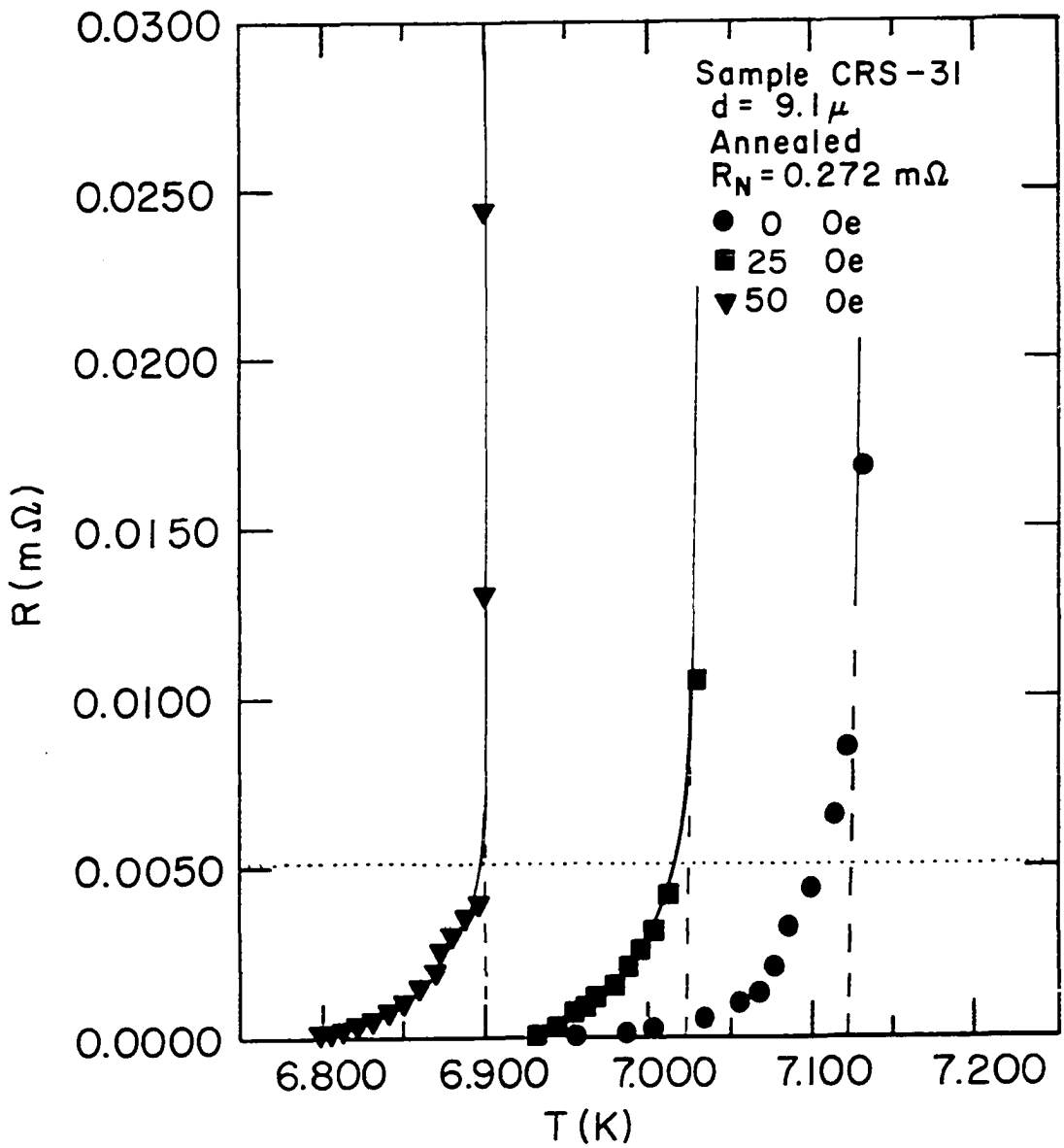
Sample CRS-31
d = 9.1 μ
Annealed
R_N = 0.272 mΩ
● 0 Oe
■ 25 Oe
▼ 50 Oe
0.0300
0.0250
0.0200
0.0150
0.0100
0.0050
0.0000
R (mΩ)
6.800
6.900
7.000
7.100
7.200
T (K)

Figure 36. Resistance versus applied magnetic field. SQUID data for sample in perpendicular current geometry for several temperatures. Dashed lines indicate expected behavior in the absence of the proximity effect in the Cd lamellae. Dotted line shows calculated resistance of Cd lamellae

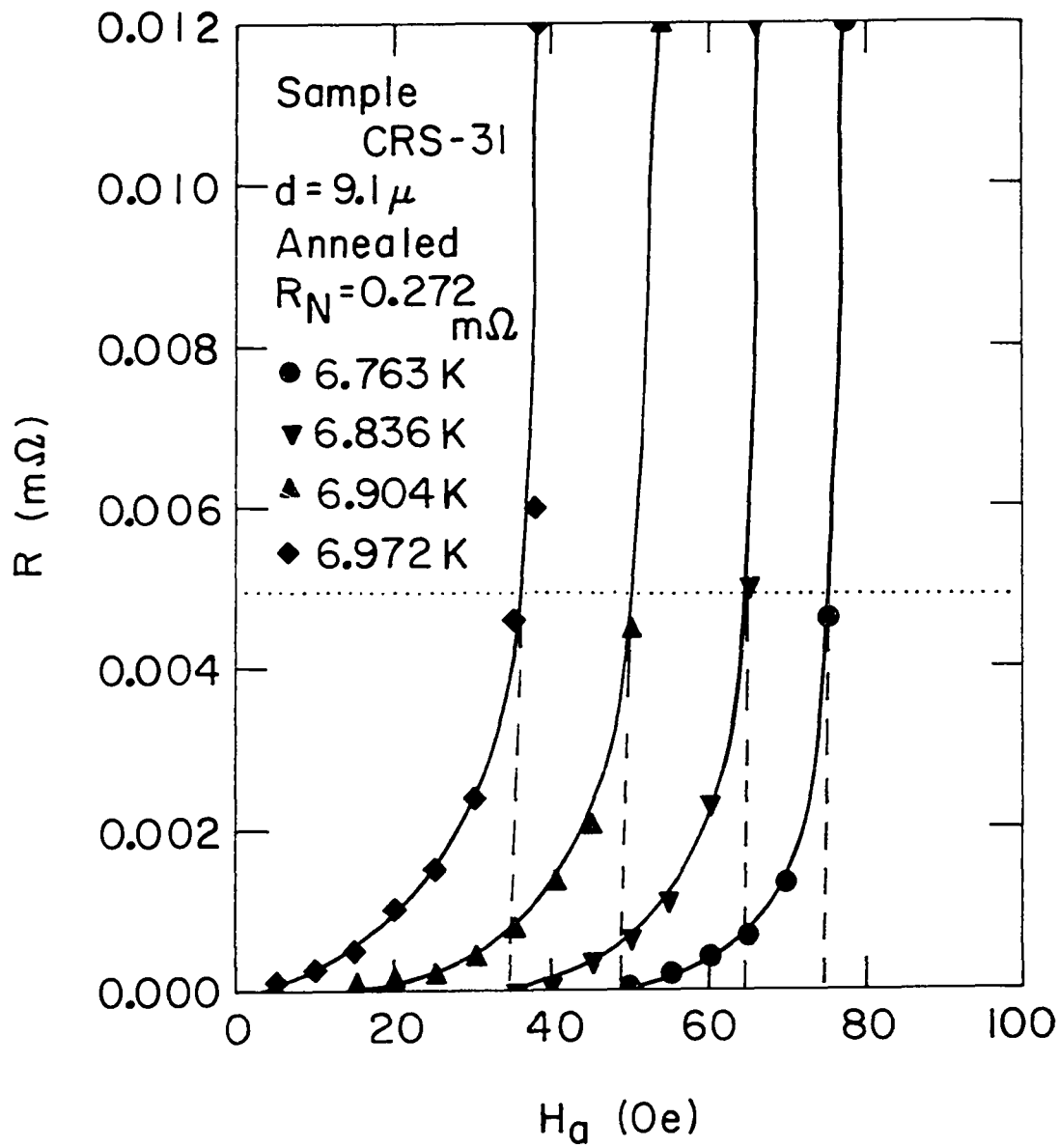
Sample
CRS-31
d = 9.1 μ
Annealed
R_N = 0.272 mΩ
● 6.763 K
▼ 6.836 K
▲ 6.904 K
◆ 6.972 K
R (mΩ)
0.012
0.010
0.008
0.006
0.004
0.002
0.000
0
20
40
60
80
100
H_a (Oe)

Figure 37. Predicted spatial dependence of the penetration depth in Cd lamellae for several temperatures. Curves shown are for a sample with a Pb transition temperature of 7.165K and Cd lamellae of 20,000 angstrom thickness

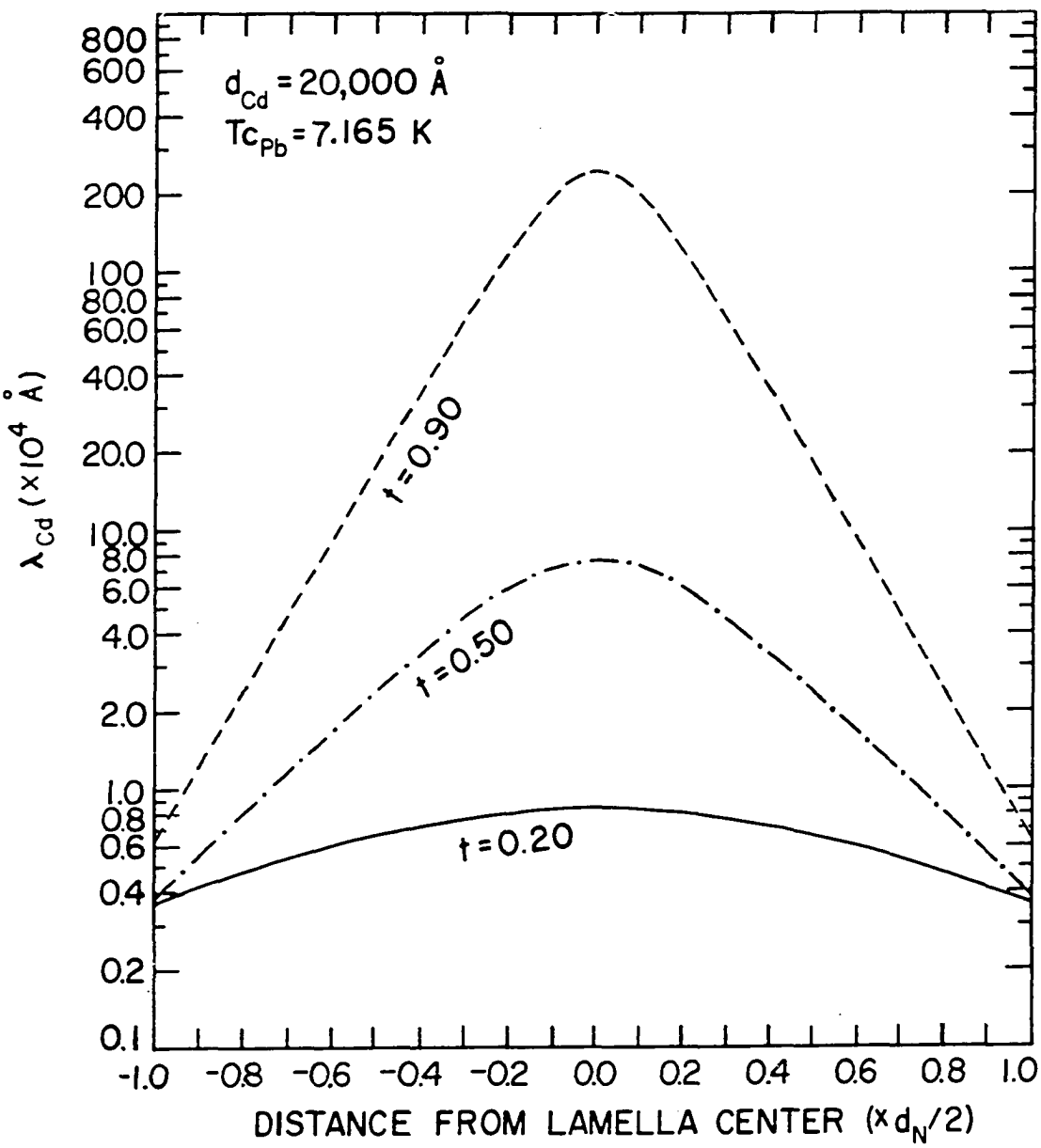
d_{Cd} = 20,000 Å
Tc_{Pb} = 7.165 K
t = 0.90
t = 0.50
t = 0.20
λ_{Cd} (x 10^4 Å)
800
600
400
200
100
80.0
60.0
40.0
20.0
10.0
8.0
6.0
4.0
2.0
1.0
0.8
0.6
0.4
0.2
0.1
-1.0 -0.8 -0.6 -0.4 -0.2 0.0 0.2 0.4 0.6 0.8 1.0
DISTANCE FROM LAMELLA CENTER (x d_N/2)

Figure 38. Typical I-V characteristics for sample in perpendicular current geometry for various temperatures. Data taken with L-N K-5 potentiometer

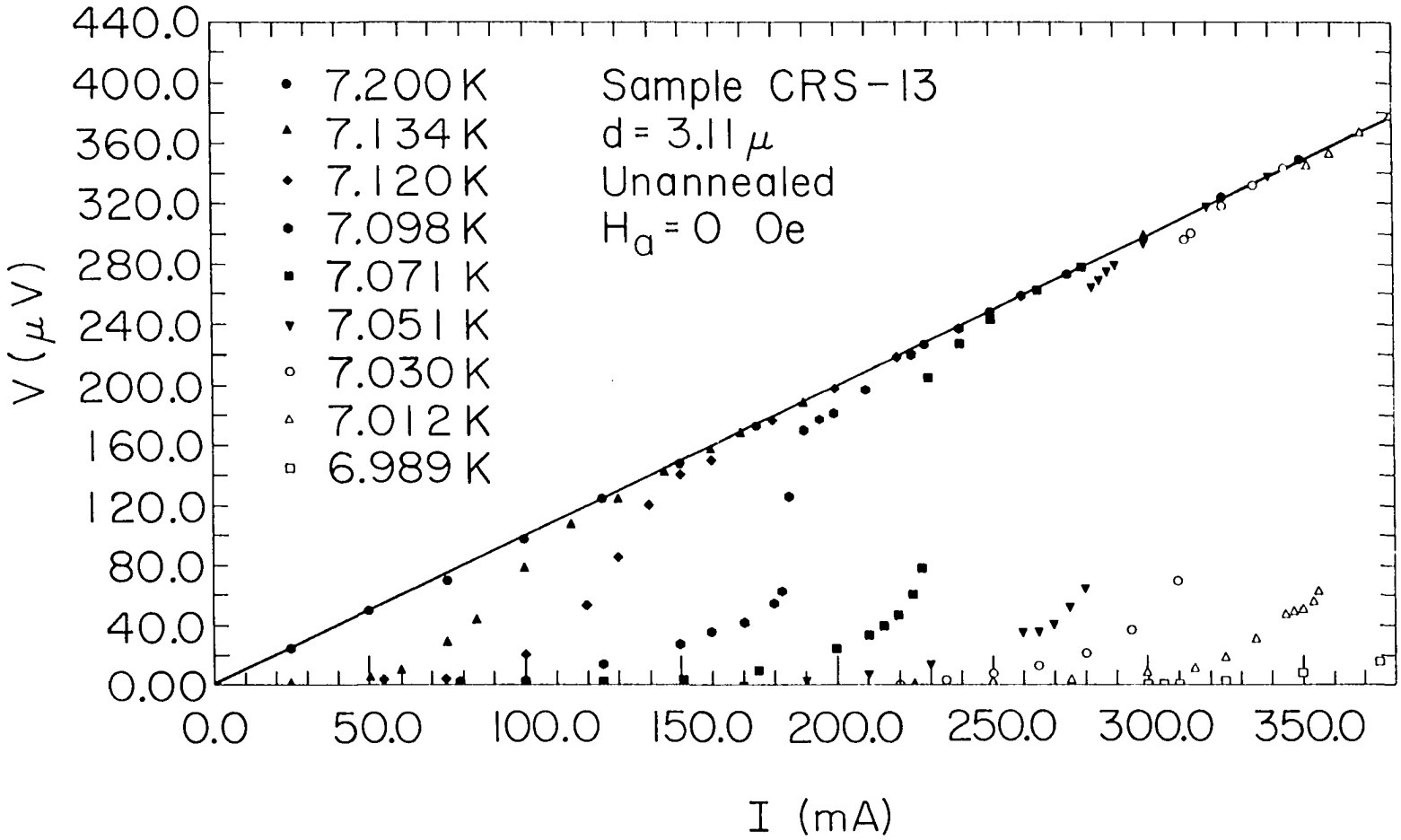
440.0
400.0
360.0
320.0
280.0
240.0
200.0
160.0
120.0
80.0
40.0
0.00
V (μV)
0.0
50.0
100.0
150.0
200.0
250.0
300.0
350.0
I (mA)
• 7.200 K
▲ 7.134 K
◆ 7.120 K
• 7.098 K
■ 7.071 K
▼ 7.051 K
○ 7.030 K
△ 7.012 K
□ 6.989 K
Sample CRS-13
d = 3.11 μ
Unannealed
H_a = 0 Oe

Figure 39. SQUID measurements of I-V characteristics for sample in perpendicular current geometry. Slashed line shows predicted Cd normal state resistance

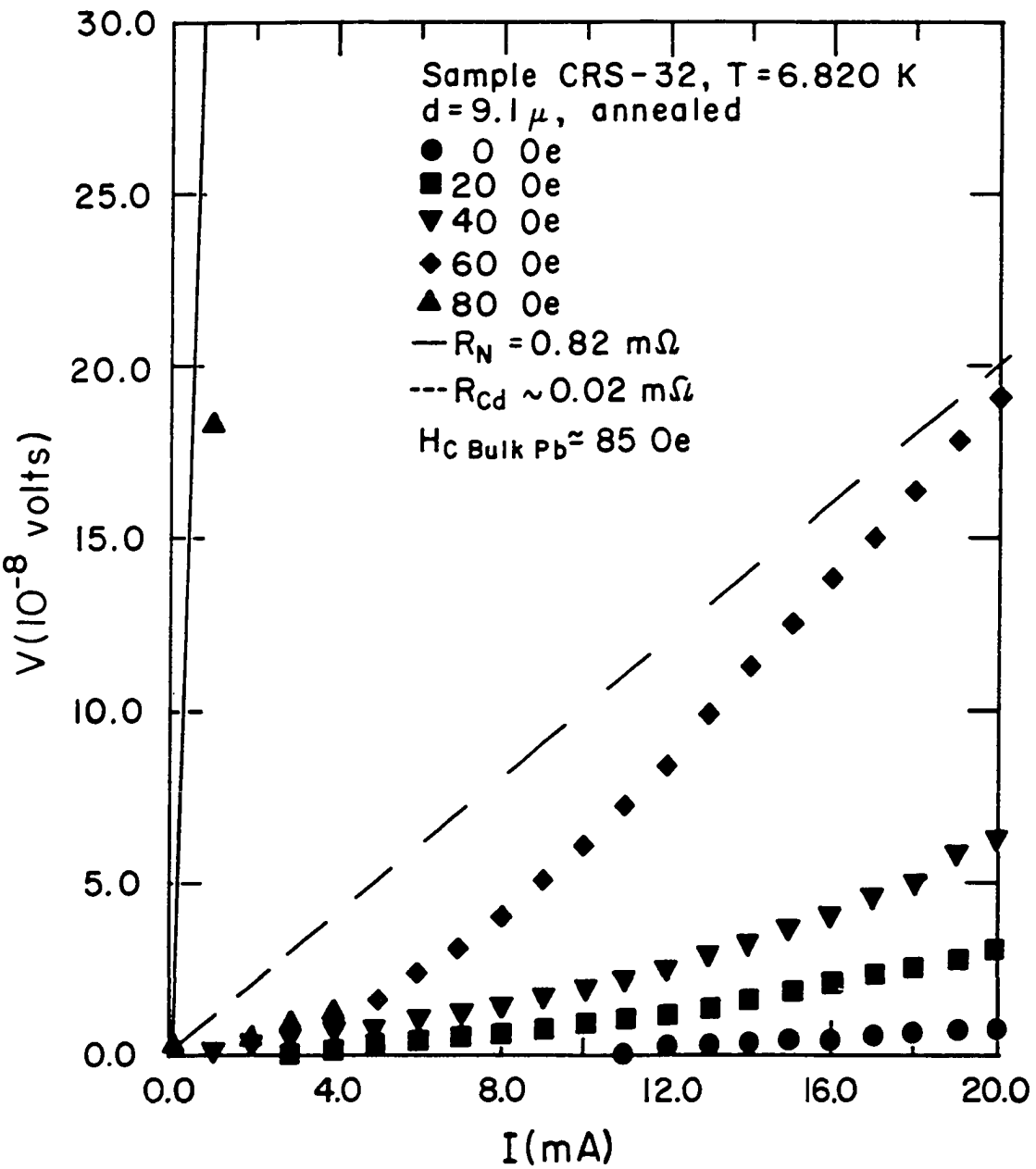
Sample CRS-32, T=6.820 K
d=9.1 μ, annealed
● 0 Oe
■ 20 Oe
▼ 40 Oe
◆ 60 Oe
▲ 80 Oe
— R_N = 0.82 mΩ
--- R_{Cd} ~ 0.02 mΩ
$H_{C\ Bulk\ Pb}$ ≃ 85 Oe
V(10^{-8} volts)
I(mA)
30.0
25.0
20.0
15.0
10.0
5.0
0.0
0.0
4.0
8.0
12.0
16.0
20.0

Figure 40. SQUID measurements of critical current as a function of applied magnetic field for several temperatures with sample in perpendicular current geometry

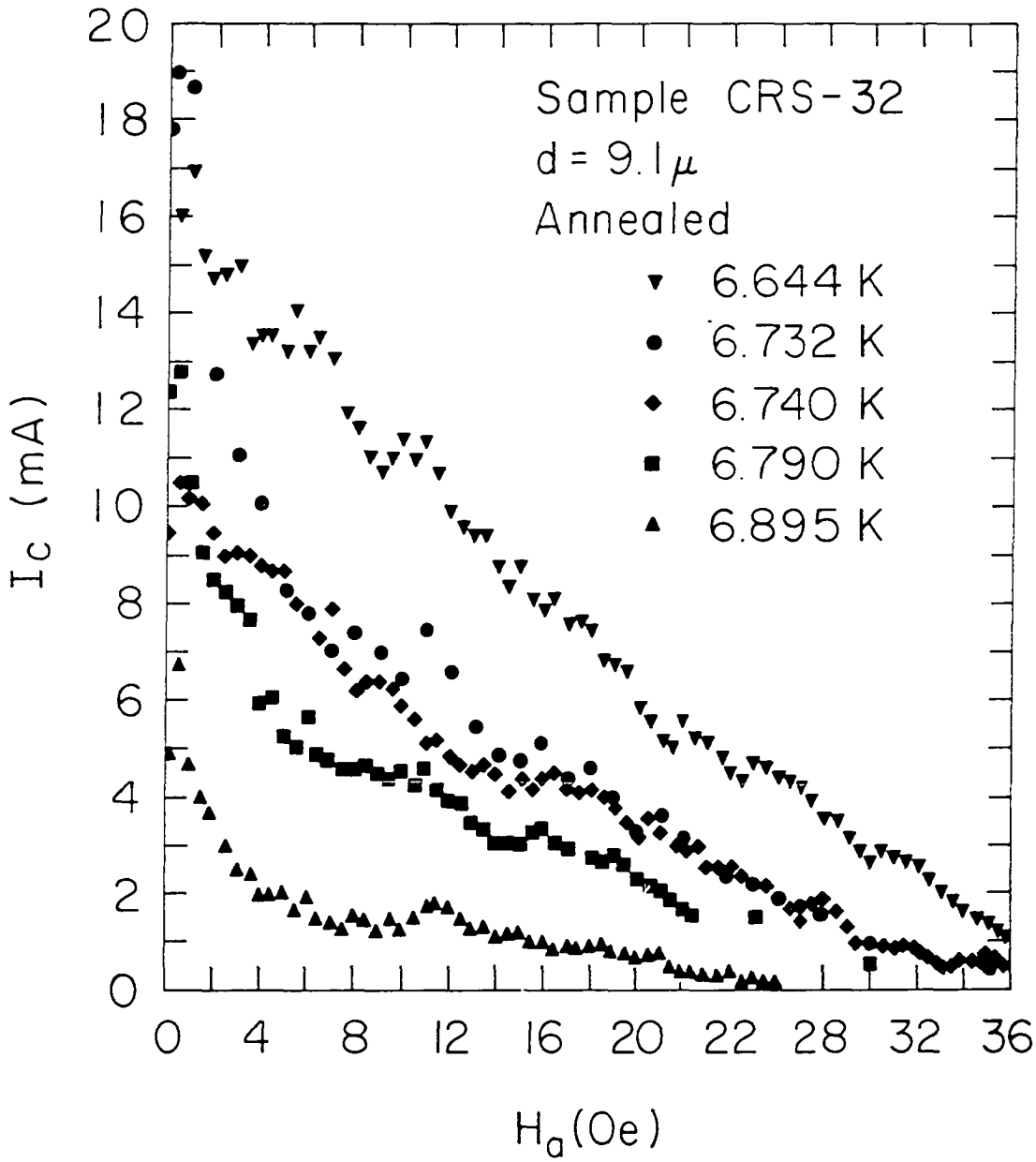
Sample CRS-32
d = 9.1 μ
Annealed
6.644 K
6.732 K
6.740 K
6.790 K
6.895 K
Ic (mA)
Ha(Oe)
0
2
4
6
8
10
12
14
16
18
20
0
4
8
12
16
20
22
28
32
36

Figure 41. The maximum current through a junction of dimension $Z = 10 \lambda_J$ as a function of applied magnetic field (98). The experimentally measured maximum current through the junction is represented by the envelope of these solutions

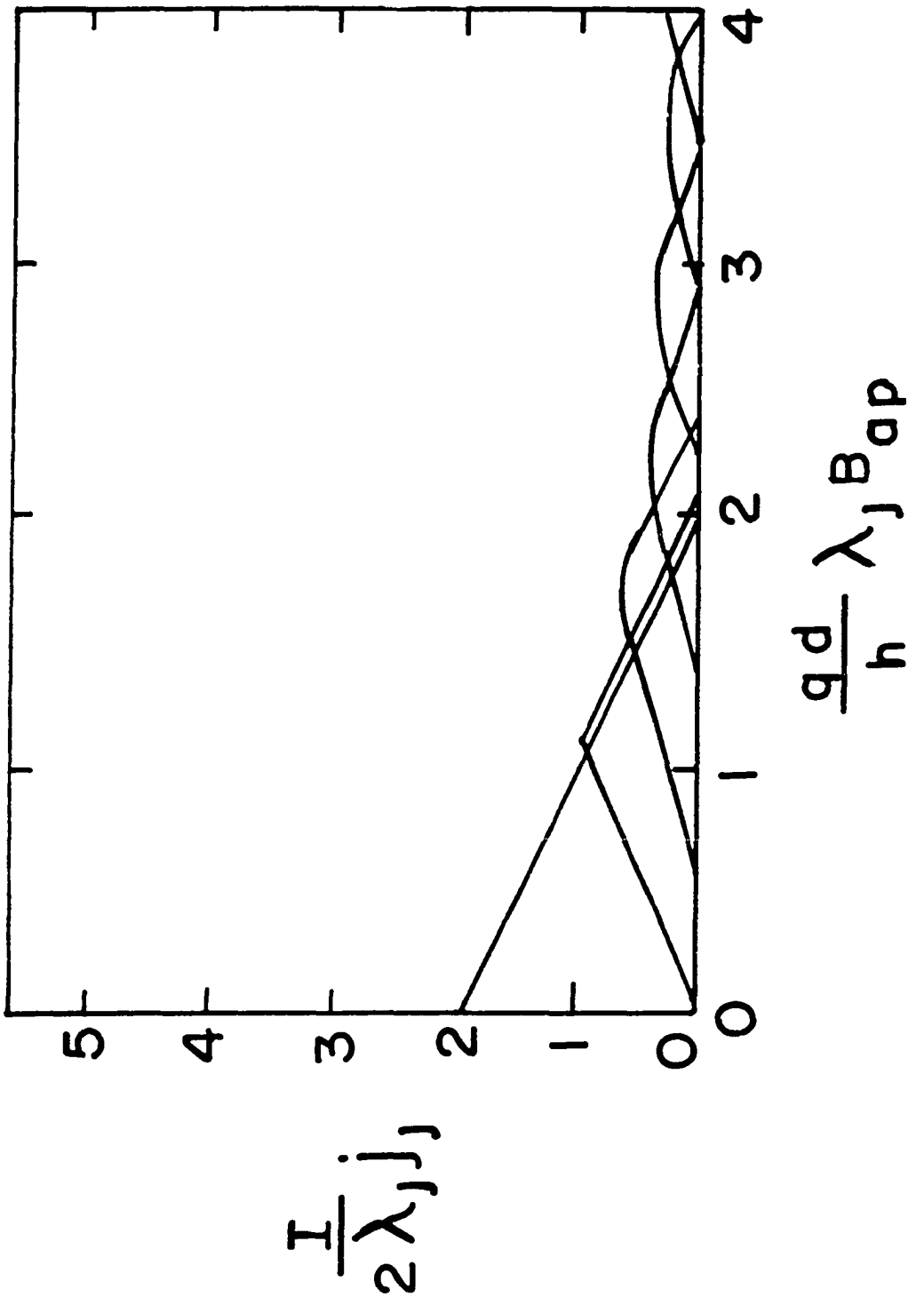
0
1
2
3
4
$\frac{qd}{h}\lambda_J B_{ap}$
0
1
2
3
4
5
$\frac{I}{2\lambda_J j_J}$

Figure 42. SQUID measurements of critical current as a function of applied magnetic field with sample in perpendicular current geometry

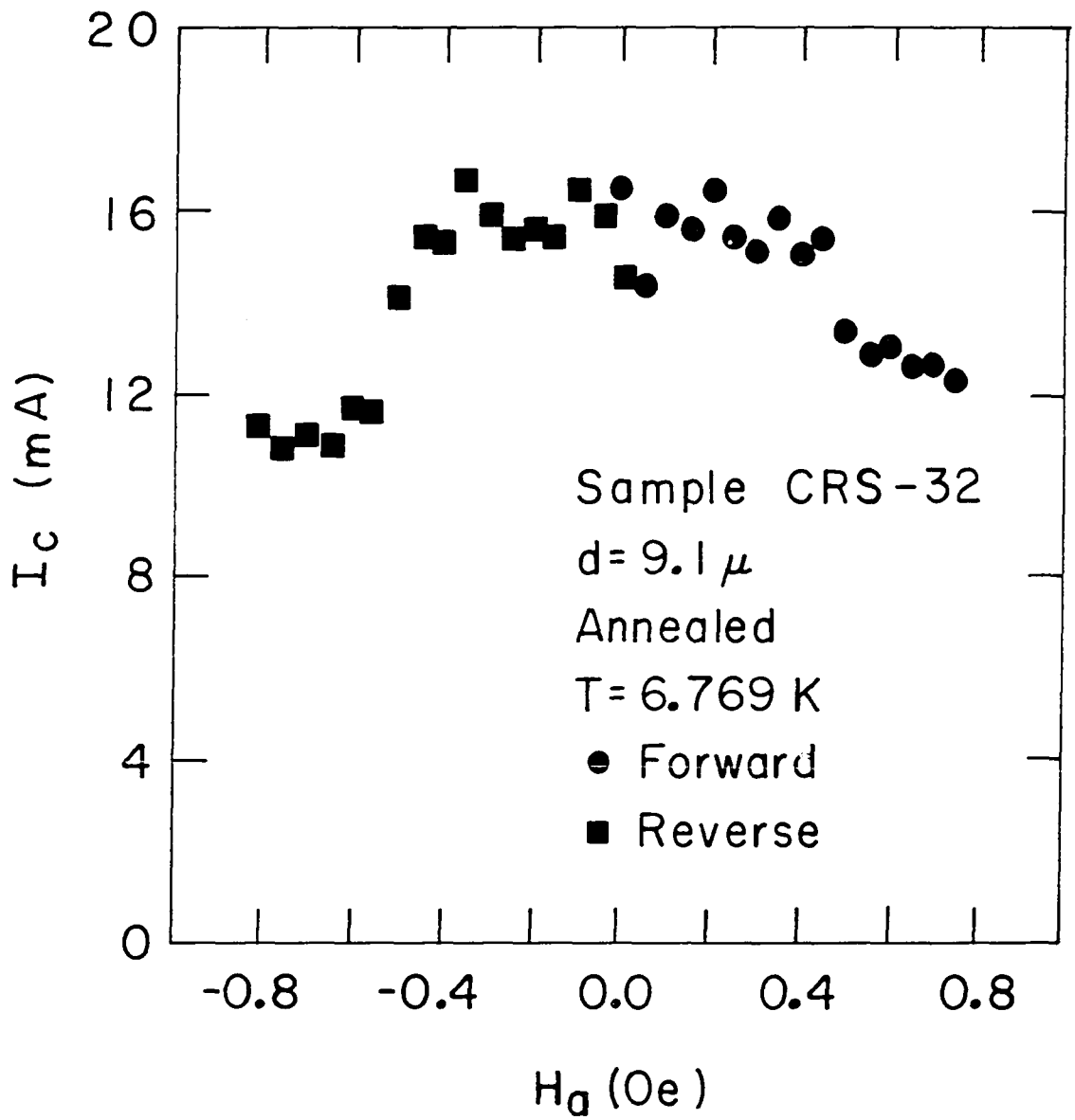
20
16
12
8
4
0
I_c (mA)
-0.8
-0.4
0.0
0.4
0.8
H_a (Oe)
Sample CRS-32
d= 9.1 μ
Annealed
T= 6.769 K
Forward
Reverse

BIBLIOGRAPHY

1. H. Kamerlingh Onnes, Akad. van Wetenschappen (Amsterdam) 14, 113, 818 (1911).

2. I. Giaever, Phys. Rev. Letters 5, 147, 464 (1960).

3. J. R. Toplicar, Ph.D. thesis, Iowa State University, 1976 (unpublished).

4. M. P. Zaitlin, private communication.

5. B. D. Josephson, Phys. Letters 1, 251 (1962).

6. J. File and R. G. Mills, Phys. Rev. Letters 10, 93 (1963).

7. W. Meissner and R. Ochsenfeld, Naturwiss. 21, 787 (1933).

8. J. L. Olsen and H. Rohrer, Helv. Phys. Acta 30, 49 (1957).

9. J. Bardeen, L. N. Cooper, and J. R. Schrieffer, Phys. Rev. 108, 1175 (1957).

10. B. S. Chandrasekhar, in Superconductivity, edited by R. D. Parks, (Marcel Dekker, New York, 1969) Vol. 1, p. 1.

11. A. C. Rose-Innes and E. H. Rhoderick, Introduction to Superconductivity, (Pergamon Press, Oxford, 1976).

12. N. R. Werthamer, Phys. Rev. 132, 2440 (1963).

13. P. G. de Gennes and E. Guyon, Phys. Lett. 3, 168 (1963).

14. P. Fulde and K. Maki, Phys. Rev. Lett. 18, 675 (1965).

15. W. L. McMillan, Phys. Rev. 175, 537 (1968).

16. W. J. Haas and J. Voogd, Leiden Commun. 208b, (1930).

17. W. H. Keesom, Physica 2, 35 (1935).

18. T. G. Berlincourt and R. R. Hake, Phys. Rev. Letters 9, 293 (1962).

19. T. G. Berlincourt and R. R. Hake, Phys. Rev. 131, 140 (1963).

20. Y. B. Kim, C. F. Hempstead, and A. R. Strnad, Phys. Rev. Letters 9, 306 (1962).

21. Y. B. Kim, C. F. Hempstead, and A. R. Strnad, Phys. Rev. 129, 528 (1963).

22. P. W. Anderson, Phys. Rev. Letters 9, 309 (1962).

23. A. M. Campbell and J. E. Evetts, Adv. Phys. 21, 199 (1972).

24. Y. B. Kim, C. F. Hempstead, and A. R. Strnad, Rev. Mod. Phys. 36, 43 (1964).

25. Y. B. Kim, C. F. Hempstead, A. R. Strnad, Phys. Rev. Letters 12, 145 (1964).

26. Y. B. Kim, C. F. Hempstead, and A. R. Strnad, Phys. Rev. 139, A1163 (1965).

27. B. D. Josephson, Phys. Rev. 152, 211 (1966).

28. S. M. Khanna, John R. Clem, and M. A. R. Le Blanc, Phys. Rev. B 14, 3898 (1976).

29. J. Bardeen and M. J. Stephen, Phys. Rev. 140, A1197 (1965).

30. H. Raffy, J. C. Renard, and E. Guyon, Solid State Commun. 11, 1679 (1972).

31. H. Raffy, E. Guyon, and J. C. Renard, Solid State Commun. 14, 427 (1974).

32. H. Raffy, E. Guyon, and J. C. Renard, Solid State Commun. 14, 431 (1974).

33. P. Martinoli, O. Daldini, C. Leemann, and E. Stocker, Solid State Commun. 17, 205 (1975).

34. P. Martinoli, O. Daldini, C. Leemann, and B. Van den Brandt, Phys. Rev. Lett. 36, 382 (1976).

35. P. G. de Gennes, Rev. Mod. Phys. 36, 225 (1964).

36. V. L. Ginzburg and L. D. Landau, Zh. Eksperim. i Teor. Fiz. 20, 1064 (1950).

37. P. G. de Gennes, in Quantum Fluids, edited by D. F. Brewer (North-Holland Publishing Co., Amsterdam, 1966) p. 26.

38. P. Martinoli, private communication.

39. P. G. de Gennes, Superconductivity of Metals and Alloys, (W. A. Benjamin, Inc., New York, 1966).

40. R. O. Zaitsev, Soviet Phys.--JETP 23, 702 (1966).

41. A. L. Fetter and P. C. Hohenberg, in Superconductivity, edited by R. D. Parks (Marcel Dekker, New York, 1969) Vol. 2, p. 817.

42. H. T. Davis, in Handbook of Mathematical Functions, edited by M. Abramowitz and I. A. Stegun (Dover Publications, Inc., New York, 1972), p. 811.

43. N. R. Werthamer, in Superconductivity, edited by R. D. Parks (Marcel Dekker, New York, 1969) Vol. 1, p. 321.

44. L. Dobrosavljevic and P. G. de Gennes, Solid State Comm. 5, 177 (1967).

45. G. Deutscher and P. G. de Gennes, in Superconductivity, edited by R. D. Parks (Marcel Dekker, New York, 1969) Vol. 2, p. 1005.

46. P. W. Anderson and J. M. Rowell, Phys. Rev. Letters 10, 230 (1963).

47. J. Clarke, Proc. Roy. Soc. Lond. A308, 447 (1969).

48. J. R. Waldram, A. B. Pippard, and J. Clarke, Phil. Trans. Roy. Soc. Lond. A268, 265 (1970).

49. F. E. E. Lamplough and J. T. Scott, Proc. Roy. Soc. A90, 600 (1914).

50. F. L. Brady, J. Inst. of Met. 28, 369 (1922).

51. A. M. Portevin, J. Inst. Met. 29, 239 (1923).

52. C. H. Green, Trans. Am. Inst. Min. and Met. Eng. 71, 651 (1925).

53. W. A. Tiller, in Liquid Metals and Solidification, (American Society for Metals, Cleveland, 1958) p. 276.

54. J. D. Verhoeven, Fundamentals of Physical Metallurgy (John Wiley & Sons, Inc., New York, 1975).

55. K. A. Jackson and J. D. Hunt, Trans. Met. Soc. AIME 236, 1129 (1966).

56. C. Zener, Trans. Met. Soc. AIME 167, 405 (1946).

57. A. J. Bevolo, E. D. Gibson, J. D. Verhoeven, and D. K. Finnemore, Phys. Rev. B 14, 114 (1976).

58. Max Hansen, Constitution of Binary Alloys (McGraw-Hill, New York, 1958).

59. G. K. White, Experimental Techniques in Low Temperature Physics, (Oxford University Press, London, 1968).

60. A. C. Rose-Innes, Low Temperature Laboratory Techniques, (English Universities Press Ltd., London, 1973).

61. R. J. Delfs, Ph.D. thesis, Iowa State University, 1975 (unpublished).

62. T. C. Cetas and C. A. Swenson, "Magnetic Temperature Scale from 0.9 to 18K," Temperature, (Instrument Society of America, Pittsburgh, 1972), Vol. 4, p. 57.

63. K. R. Efferson, Rev. Sci. Instrum., 38, 1776 (1967).

64. Y. B. Kim and M. J. Stephen, in Superconductivity, edited by R. D. Parks (Marcel Dekker, New York, 1969) Vol. 2, p. 1107.

65. Y. B. Kim, C. F. Hempstead, and A. R. Strnad, Phys. Rev. 131, 2486 (1963).

66. A. R. Strnad, C. F. Hempstead, and Y. B. Kim, Phys. Rev. Letters 13, 794 (1964).

67. D. A. Lilly and A. N. Gerritsen, Physica 69, 286 (1973).

68. O. P. Katyal and A. N. Gerritsen, Phys. Rev. 185, 1017 (1969).

69. R. A. Young, Phys. Rev. 183, 611 (1969).

70. R. C. Callarotti and P. Schmidt, in International Conference on Low Temperature Physics--LT 13, edited by K. D. Timmerhaus, W. J. O'Sullivan, and E. F. Hammel (Plenum Press, New York, 1974) Vol. 4, p. 353.

71. W. R. Decker, Ph.D. thesis, Iowa State University, 1971 (unpublished).

72. K. W. Taconis, in Progress in Low Temperature Physics, edited by C. J. Gorter (North-Holland Publishing Co., Amsterdam, 1961), Vol. III.

73. B. A. Haskell, Ph.D. thesis, Iowa State University, 1971 (unpublished).

74. D. K. Finnemore, Ames Laboratory of the United States Atomic Energy Commission Data Book DFK-9, 1968 (unpublished).

75. J. Clarke, S. M. Freake, M. L. Rappaport, and T. L. Thorp, Solid State Comm. 11, 689 (1972).

76. J. M. Dupart and J. Baixeras, Appl. Phys. Letters 30, 123 (1977).

77. R. P. Giffard, R. A. Webb, and J. C. Wheatley, J. Low Temp. Phys. 6, 533 (1972).

78. G. T. Meaden, Electrical Resistance of Metals, (Plenum Press, New York, 1965).

79. D. Mourer, M.S. thesis, Iowa State University, 1976 (unpublished).

80. J. D. Livingston, J. Appl. Phys. 34, 3028 (1963).

81. J. D. Livingston, private communication.

82. H. Meissner, Phys. Rev. 117, 672 (1960).

83. A. C. Rose-Innes and B. Serin, Phys. Rev. Letters 7, 228 (1961).

84. P. Hilsch, Z. Physik 167, 511 (1962).

85. J. Clarke, Phys. Rev. B 4, 2963 (1971).

86. L. P. Gor'kov, Soviet Phys.--JETP 7, 505 (1958).

87. F. B. Silsbee, J. Wash. Acad. Sci. 6, 597 (1916).

88. R. P. Huebener, R. T. Kampwirth, and J. R. Clem, J. Low Temp. Phys. 6, 275 (1972).

89. J. R. Clem, J. Low Temp. Phys. 18, 427 (1975).

90. M. G. Blanchin, A. Guinier, C. Petipas, and G. Sauvage, Acta Met. 20, 1251 (1972).

91. C. P. Bean, Rev. Mod. Phys. 36, 31 (1964).

92. O. Daldini, P. Martinoli, J. L. Olsen, and G. Berner, Phys. Rev. Letters 32, 218 (1974).

93. R. G. Chambers, Proc. Roy. Soc. 215, 481 (1952).

94. M. S. Khaikin, Soviet Phys.--JETP 7, 961 (1958).

95. C. Kittel, Introduction to Solid State Physics, Fourth Edition (John Wiley & Sons, Inc., New York, 1971).

96. L. G. Aslamazov and A. I. Larkin, Soviet Phys.--JETP 41, 381 (1975).

97. C. S. Owen and D. J. Scalapino, Phys. Rev. 164, 538 (1967).

98. L. Solymar, Superconductive Tunneling and Applications (Chapman and Hall, Ltd., London, 1972).

99. H. A. Notarys and J. E. Mercereau, in Superconductivity, edited by Frank Chilton (North-Holland Publishing Co., Amsterdam, 1971), p. 424.

100. Jon Lechevet, J. E. Neighbor, and C. A. Shiffman, J. Low Temp. Phys. 27, 407 (1977).

101. Jon Lechevet, J. E. Neighbor, and C. A. Shiffman, Phys. Rev. B 5, 861 (1972).

ACKNOWLEDGMENTS

The road to a graduate degree is often a rough, rocky, and occasionally unmarked path along which to journey. The author wishes to thank those who helped to guide the way and to smooth out the many obstacles encountered along the course of his graduate study. Special thanks and gratitude are extended to Dr. D. K. Finnemore for his advice and guidance throughout the course of this work. The author is especially grateful to Dr. Piero Martinoli for his suggestions during the preparation of this manuscript. Special thanks also must be offered to Dr. J. D. Verhoeven and to Mr. E. D. Gibson for their invaluable aid and suggestions involving the sample preparation and for their SEM microscopy work on the Pb-Cd samples.

Because the journey toward a graduate degree is a long and occasionally lonely endeavor, the author is eternally grateful to the members of Dr. D. K. Finnemore's low temperature group for their many helpful suggestions. Special thanks are in order for Mr. J. E. Ostenson for his reliable and continually available advice.

Last, but certainly not least, the author wishes to thank his wife, Lynn, for her continual moral support, encouragement, and understanding throughout the many trials and tribulations endured during the author's graduate career.